

HARVARD UNIVERSITY
Graduate School of Arts and Sciences




DISSERTATION ACCEPTANCE CERTIFICATE

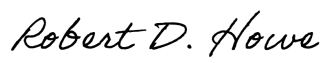
The undersigned, appointed by the

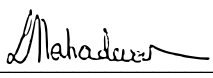
Harvard John A. Paulson School of Engineering and Applied Sciences
have examined a dissertation entitled:

“Soft Contact: Design and Fabrication for Gentle Grasping and Manipulation”

presented by: Kaitlyn Patricia Becker

Signature 
Typed name: Professor R. Wood

Signature 
Typed name: Professor R. Howe

Signature 
Typed name: Professor L. Mahadevan

April 29, 2021

Soft Contact: Design and Fabrication for Gentle Grasping and Manipulation

A dissertation presented

by

Kaitlyn Patricia Becker

to

The John A. Paulson School of Engineering and Applied Sciences

in partial fulfillment of the requirements

for the degree of

Doctor of Philosophy

in the subject of

Engineering Sciences

Harvard University

Cambridge, Massachusetts

April 2021

©2021 Kaitlyn Patricia Becker

All rights reserved.

Dissertation Advisor:
Professor Robert J. Wood

Author:
Kaitlyn Patricia Becker

Soft Contact: Design and Fabrication for Gentle Grasping and Manipulation

Abstract

The compliance of soft robots makes them particularly well suited for grasping applications where target objects are fragile, compliant, or topologically complex, as well as scenarios where target objects have an uncertain size or location. This thesis is an exploration of soft robotic design and fabrication that enables three modes in which characteristics of the contact interface between soft grippers and their target objects can be strategically tuned. First, passive digit structures and materials can be used to reduce contact stress concentrations and adapt to varying object sizes. Second, active surface structures can be used to increase dexterity of soft grippers by modulating contact friction. Third, a new grasping strategy of randomly distributed contacts can be used to achieve grasps that are individually gentle and collectively strong. We call this strategy entanglement grasping and present novel manufacturing methods to create the high aspect ratio soft actuators and large arrays that are the basis for this technique. The structural compliance of high aspect ratio large collectives enable passive, stochastic adaptation to compliant target structures and complex topologies. For each modality of contact tuning, passive, active, and distributed, I present novel mechanisms, fabrication methods, and design tools to create soft grippers for gentle grasping and manipulation.

Contents

Title Page	i
Abstract	iii
Table of Contents	iv
Acknowledgments	vii
Dedication	ix
1 Introduction	1
1.1 Motivation: challenging target grasps	1
1.2 How soft contact can adapt for challenging grasps	2
1.3 Challenges and opportunities designing for soft systems	3
1.4 Contributions and chapter organization	4
1.5 Previously published manuscripts	6
2 Passive Contact Tuning	8
2.1 Introduction	8
2.2 Motivation: deep-sea biological sampling	10
2.3 Background and prior art for compliant grippers	12
2.4 Two hydraulic soft actuator architectures	15
2.4.1 Boa-type actuator	16
2.4.2 Boa-type actuator fabrication	17
2.4.3 Bellow-type actuator	20
2.4.4 Bellows-type actuator fabrication	20
2.5 Creating gentle, conformal, and robust grasps	24
2.5.1 Rapid digital prototyping of geometric designs for large deformations	24
2.5.2 Modular strain-limiting elements	28
2.5.3 Mechanically programmed contact stress limits	30
2.5.4 Fabrication details to enhance cycle-life and burst pressure	31
2.5.4.1 Soft cores	32
2.5.4.2 Material compatibility and mold design	33
2.6 Characterization of gentle, conformal, and robust grasps	34
2.6.1 Grasp contact pressure	34
2.6.2 Grasp strength	35
2.7 Field-testing	38

3	Active Modulation of Surface Contact	40
3.1	Introduction	40
3.2	Background and prior art	41
3.3	Soft mechanism for active friction modulation	42
3.3.1	Principle of operation	42
3.3.2	Model	42
3.3.3	Geometry and materials	44
3.4	Characterization of friction modulation mechanism	45
3.4.1	Module for isolated mechanism testing	45
3.4.2	Testing setup	45
3.4.3	Effect of preload force	47
3.4.4	Effect of substrate material	47
3.4.5	Effect of inflation pressure	48
3.5	Soft robot integration	50
3.5.1	Integration with a soft gripper	50
3.5.2	Integration with a crawling robot	53
3.6	Conclusions and future work	58
4	Distributed contact via soft arrays	59
4.1	Introduction	59
4.2	Background and prior art	62
4.3	Open face molds and dip molding	64
4.4	Four methods of mechanical programming	66
4.4.1	Actuation direction programmed via strain-limiting fibers	68
4.4.2	Unidirectional actuation established via gravity	68
4.4.3	Actuation direction established via surface tension	70
4.4.4	Actuation direction established via electric fields	70
4.4.5	Comparison of mechanical programming strategies	71
4.4.6	Scale and aspect ratio limitations	73
4.5	Fabrication details for motion programming methods	74
4.5.1	Actuator plumbing	75
4.5.2	Fiber inclusion pin preparation	75
4.5.3	Fixtures for gravity programmed actuators	76
4.5.4	Fabrication of surface tension programmed actuators	77
4.5.4.1	Surface-tension pins	77
4.5.4.2	Surface-tension actuator plumbing	78
4.5.5	Fabrication for electric-field programming	79
4.5.5.1	Fabrication setup	79
4.5.5.2	Electric-field modeling	81
4.6	Characterization of individual actuator performance	86
4.6.1	Operational pressure and curvature characterization	87
4.6.1.1	Automated measurement of curvature and operating pressure	87
4.6.1.2	Resulting curvature and operating pressure relationship . .	88
4.6.2	Holding force characterization	90
4.6.3	Burst pressure	97

4.7	Fabrication modifications for large arrays, long actuators, and control integration	98
4.7.1	Large arrays	98
4.7.1.1	Rubber pouring and cycling for large arrays	98
4.7.1.2	Strain limiting in the base of arrays	98
4.7.1.3	Fabrication steps for Large Arrays	99
4.7.2	Fixture and pouring modifications for long actuators	105
4.7.3	Two degree of freedom actuators	106
4.7.4	Integration with microfluidic control	108
4.8	Conclusion	110
5	Entanglement Grasping	112
5.1	Introduction	112
5.2	Background and prior art	115
5.3	Evaluation of entanglement strategy: physical testing	117
5.3.1	Object set for grasp testing	118
5.3.2	Evaluation of approach strategies	119
5.3.3	Work space and sensitivity to position error	123
5.3.4	Grip strength	123
5.3.5	Grasp toughness metric	125
5.3.6	Contact distribution	127
5.4	Exploration of entanglement gripper design space via numerical simulation	128
5.4.1	Entanglement grasp success phase space	131
5.4.2	Preliminary contact study	133
5.5	Prototype entanglement gripper	134
5.5.1	Hardware	134
5.5.2	Filament actuator fabrication	134
5.5.3	Pneumatic actuation and control	135
5.5.4	Field tests and challenging objects	136
5.6	Conclusion	137
6	Conclusions and Future Work	139
6.1	Integration	140
6.2	Passive tuning: surface and structure	140
6.3	Application of friction tuning: dexterous manipulation	141
6.4	Application of arrays: study of biological systems	142
6.5	Further exploration and application of entanglement	143
6.6	Hybrid control with embodied intelligence	144
6.7	Tools for soft system design and innovation	144
6.8	Conclusion	145
	Bibliography	146

Acknowledgments

Thank you to my advisor, Professor Rob Wood, for fostering a research community that is collaborative, multidisciplinary, supportive, and creative. You and the lab that you have created are the reason that I came to Harvard. Thank you for the years of support, for the challenge to bring new ideas to the table, and for the freedom to find myself as a researcher. I'm so grateful for the opportunity to work in such a welcoming and stimulating environment, as well as for the numerous opportunities you've made possible to take my work outside of the lab.

Through thoughtful discussions and the greater community that they have fostered, Professor L. Mahadevan, Professor Rob Howe, and Professor Andy Biewener have also had an enormously positive influence on my career.

Thanks to Brennan Phillips and David Gruber for making the opportunities for field testing possible and your confidence in my ability to tackle the challenges that come with taking research out of a lab. You will always be my role models in the level of energy and enthusiasm that you bring to your work.

Kevin Galloway and Sam Felton, thank you for the early and generous mentorship in my graduate school experience. Thank you for the guidance in joining the Microrobotics lab, helping me find my footing in graduate research, and making space for me on projects that have had a lasting influence on my work.

I'm thankful for the daily conversations, inspiring presence, and helpful efforts of my colleagues in the Microrobotics lab, as well the lab communities of Rob Howe and Conor Walsh, with whom I've been fortunate to share space.

Farrell Helbling, I cannot express enough gratitude for your friendship, support, and humor throughout this adventure. I am in awe of your wit, grit, and generosity. The toughest moments were always easier to bear with some of your honest advice, pragmatically acknowledging unpleasant moments and laughing (or ranting) about them.

Kate Pukinskis and Seun Araromi, you've often understood me before I figured out what was in my own head. I so appreciate our friendship and conversations. Both of you have been role models in the thoughtfulness with which you approach work and life, as well as the generosity that you exhibit in mentorship and random acts of kindness. I also very much appreciate your appreciation of silly moments.

Anthony Camilleri, Brooks Willis, Diana Wagner, Michael Bell, Qian Wan, Rut Peña, and Zeynep Temel, thank you so much for the rants, the sounding board discussions, the fabrication geekery, the adventures, and the general sanity support. I cannot overstate

Acknowledgments

how much I appreciate your companionship in this journey and sharing in your enthusiasm for projects, big or small, serious or silly.

The MIT glass lab community has been like a family and a place where I always feel like I belong. I cannot think of a single community or experience that has had more influence on who I am as a fabricator and an engineer. Similarly, I cannot think of a place or group of people that more effectively combines mind and hand in a sandbox to be able to play with engineering principles. Michael Stern, Olivia Cheo, Peter Houk, and Whit Cornforth, working with you and your friendship has been a decade and a half of (occasionally challenging) joy.

Another family that I found recently is Mather house. It's been a privilege to work with such a stellar house team and students. I'm always in awe of the diversity of talents, intellectual curiosity, and community spirit coming from this house. My favorite memories will be dining hall discussions that naturally flip between technical, philosophical, and utterly ridiculous. Mather is a good house and I feel so fortunate to have lived there for the last four years.

Lastly, it has meant the world to come from such a large and loving family, particularly one that puts a high value on education, hard work, laughter, and kindness. My older brothers, Eric Becker and Kevin Becker, in particular, always challenged me to keep up, supported me when I stumbled, and trained me in the most valuable skill of laughing at myself. And, more than anyone else, I want to thank my mother, Dr. Patricia Hentz, who is responsible for so much of who I am now and who I aspire to be as a person, a student, and an educator.

For my mother,

who fostered my love of learning,
taught me to think critically,
and encouraged me to think differently.

Chapter 1

Introduction

The structural and material compliance of soft robots makes them particularly well suited for grasping applications where gentleness is a necessity. Gentleness, by itself, however, is not sufficient for successful and robust grasping. This thesis explores how the design and fabrication of soft robotic grippers can create grasps that are gentle, conformal, secure, and adaptive. To achieve these grasp characteristics, specifically, I investigate three modalities of tuning the contact interface between soft grippers and their target object; I introduce passive contact adaptations via underlying chosen materials and geometric design, active contact modulations via controllable surface structures, and distributed contacts via large arrays of highly compliant actuators. Each modality is approached from a combined perspective of design and fabrication to present solutions that are inspired by the opportunities and challenges that stem from the compliance of soft robots.

1.1 Motivation: challenging target grasps

Compliance makes soft robotic grippers an attractive alternative to rigid grippers and is also the root of the advantages and disadvantages of soft robots. The compliant materials that compose soft grippers are an opportunity for embodied intelligence that allows them to conform to target objects in a form of mechanical impedance matching [1]. The same quality, compliance, makes soft robots difficult to control and limits their inherent strength [2, 3]. Acknowledging these as strengths and opportunities (challenges), it is clear that soft robotic grippers have the potential to excel at tasks that are challenging for rigid robotic grippers. Similarly, they will not replace rigid grippers in tasks that

demand a combination of strength and precision at high speeds, for which rigid grippers are particularly well suited. Therefore, to explore where soft grippers might have the greatest impact, my work specifically targets grasping objects that have proven challenging for rigid grippers, including target objects that may be compliant, fragile, or topologically complex [4].

Deep-sea biological sampling is a task that is replete with compliant, fragile, and topologically complex specimens and further exacerbates the difficulty of grasping with thousands of pounds of hydrostatic pressure, corrosive salinity, and restricted access and feedback. The delicate manipulation of fragile species on deep-sea reefs is the initial motivation that inspired my work on soft contact, as a task that would leverage the advantages of soft grippers and highlight opportunities for development by nature of the task difficulty. Further background information is provided to motivate application to deep-sea biological sampling in Chapter 1, which lead to our demonstration of the first use of soft robotics in the deep sea for the gentle sampling of benthic fauna. Developing gripping solutions for an extreme operating scenario, such as the deep sea, drives the creation of a robust tool that can also be translated to less challenging environments. Thus the contributions introduced in the following chapters are not limited to deep-sea or hydraulic actuation. While the deep-sea has a wealth of compliant, fragile, and complex specimens, these traits can also be found in target objects on land and tested in a laboratory setting, as previewed in Figure 1.1.

1.2 How soft contact can adapt for challenging grasps

Three grasps illustrating some of the attributes that make for challenging target objects, as well as the three modalities of contact tuning that I explore in this thesis, are shown in Figure 1.1. The first, a holothurian (sea cucumber) grasped at a depth of approximately 1800 m under water is a highly compliant (and arguably fragile) animal that would normally not survive retrieval with the rigid manipulators traditionally used for deep-sea exploration. In this instance, the animal was safely picked up (gently hugged) and then replaced on the sea floor. The creature showed no signs of distress and did not engage in its known defense mechanisms. The gripper uses embodied intelligence built into the underlying structure and materials to passively create a gentle grasp ($< 2kPa$ contact pressure), that is also conformal and strong. The central photo of Figure 1.1 shows a

gripper installing a fragile light bulb with the assistance of tunable fingertip friction pads. This allows the grip to maintain a minimal normal force while it carries the bulb to the light socket and screws it into place. By activating or inactivating the friction pads, the gripper can modulate the contact friction of the grasp on and off, (on) enabling it to apply traction and turn the bulb, or (off) allowing the finger tips to slip over the surface to adjust the pose of the gripper on the bulb while still applying supportive contacts. In the third photo of Figure 1.1, a compliant, fragile, and topologically complex ivy plant is held by a novel gripper that is able to stochastically apply soft, distributed contacts. We call this novel device an entanglement gripper. By applying an array of highly compliant, soft, filament-like actuators, this entanglement gripper creates a grasp of many distributed and low-force contacts that sum to a collectively robust grasp. The gripper is thus gentle but also capable of supporting the weight of the plant and soil, and capable of adapting to the complex topology without perception or feedback.



Figure 1.1: Three demonstrations in which the design and fabrication of a soft gripper was used to specifically tune the contact interface to adapt to a target object. (Left) A hydraulically actuated gripper applies a gentle, conformal, and secure grasp to a holothurian, 1800 m under water. (Center) A pneumatically actuated gripper installs a light bulb with the help of controllable friction pads on its finger tips. (Right) An entanglement gripper applies distributed contacts to adapt to and gently lift an ivy plant.

1.3 Challenges and opportunities designing for soft systems

The relative nascency of soft robotics holds a lot of opportunity to expand and improve upon the tools and methods that we use to create soft structures designed for large

deformations. The development of the grippers shown in Figure 1.1 and discussed throughout this thesis relies on simultaneous consideration of both the design and fabrication of soft mechanisms. For mechanism design (in mechanical engineering), most of the tools and foundational training for characterization, design, and fabrication were developed for rigid systems. Built into that framework is a frequent simplifying assumption of rigid materials that will undergo small deformation, whereas soft mechanisms cannot be assumed to be rigid and the most successful mechanism designs are ones that leverage large deformations for functionality. Even if a mechanism designer is able to shift to a soft framework of large deformations, the tools that we use to both design and fabricate soft systems are still predominantly informed by rigid systems, which then has ramifications on the resulting designs [2, 5]. Designing soft systems to be fabricated with tools developed for rigid devices and, conversely, fabricating soft structures developed with design tools of rigid origins has produced a wealth of work in the field of soft robotics already. But there is arguably great potential for future disruptive impact in the simultaneous evolution of design and manufacturing of soft robots. Furthermore, the reliability and robustness of soft actuators resulting from their combined design and fabrication will be a limiting hurdle in expanding their utility, applications, and commercialization. Therefore, the design and fabrication with which we create soft robots, especially in concert, is an interesting area of research. While the design and fabrication tools and methods developed in this work focused on the application of soft grippers, many of the lessons learned can also be extended to applications in physical therapy and assistive devices, functional robotic apparel, lightweight temporary shelters, robot locomotion, and the study of biological systems.

1.4 Contributions and chapter organization

The work described in this thesis is divided generally by the modalities of contact tuning described above: passive contact tuning via materials and structure, active contact tuning via control over surface structure, and distributed contact via large arrays of highly compliant actuators. As described below, distributed contact is divided into two chapters, while the other two are covered in one chapter. Pictures of some of the relevant platforms that will be discussed in each chapter are shown in Figure 4.2.

Chapter 2 focuses on passive contact tuning: Gentle, conformal, and robust grasps can be achieved by tuning the passive mechanics of soft digits. I have demonstrated a use

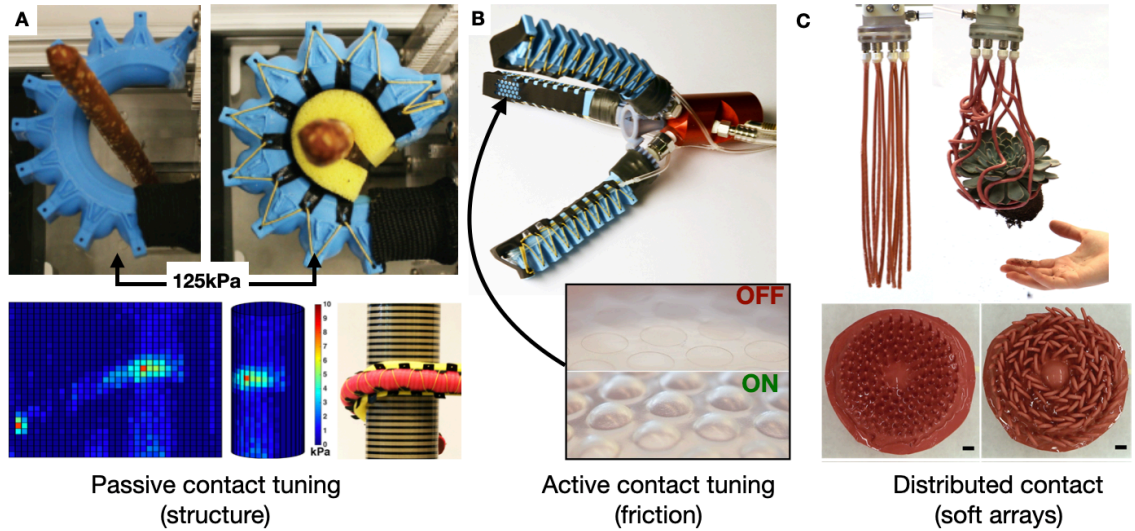


Figure 1.2: (A) The structure and materials of a soft gripper can be used to passively tune contact for a conformal, gentle, and robust grasp. (B) Active structures can be added to the surface of a gripper to modulate contact friction and introduce dexterity. (C) Large arrays of soft actuators allow for distributed contact points that are individually gentle and collectively strong.

of geometric design, incorporation of strain-limited fibers, and coupling of non-linearly elastic materials to tune the closure and contact stress of grippers for biological sampling in the deep-sea (Fig. 4.2A). These grippers have been successfully demonstrated at depths exceeding 3.5km. They achieve a gentle grasp (approximately 2 kPa of contact pressure) while operating under thousands of pounds of hydrostatic pressure, in temperatures around 3°C, and in corrosive saline environments.

Chapter 3 focuses on active contact tuning: An element of dexterity can be introduced to soft grippers via modulations in contact friction. I present friction tuning structures made of selectively constrained elastomeric membranes that can be actively or passively applied to robotic grippers and crawlers. My mechanism utilizes fluidic power input that could be part of an existing drive (passive) or controlled by an additional input (active) (Fig. 4.2B).

Chapter 4 introduces the first part of distributed contact: Distributed contact in grasping relies on the use of large arrays of high aspect ratio actuators. (This is developed into the concept of collective entanglement in the next chapter.) Large arrays and high aspect ratio actuators are both challenging to achieve in soft robotic fabrication. I provided

a solution with a new fabrication technique combining dip coating with mechanical motion programming via gravity, fiber inclusions, surface tension, and electric fields. I demonstrate the fabrication of high aspect ratio actuators ($>200:1$) and my actuator arrays are among the largest ($n=256$) of directly-driven soft actuators that can also be arbitrarily segmented in zones of actuation. An example array with a mechanically programmed vector field of actuation is shown in the bottom of Figure 4.2C. The mold forms that I developed to create both arrays and individual actuators are inexpensive, modular, rapidly fabricated, low precision, and scalable.

Chapter 5 concludes the second part of distributed contact: Arrays of the high aspect ratio actuators developed in the previous chapter are applied to create distributed contact points for the purpose of grasping. I describe a new strategy for robotic grasping via entanglement with soft, pneumatic, filament-like actuators. Large arrays of highly compliant filament actuators enable stochastic engagement with a target object. Random interactions rely on structural and material compliance to adapt to complex and compliant topologies while reducing the reliance on complicated vision, path planning, and controls (Fig. 4.2). This breaks from traditional strategies for robotic grasping, which use deterministic methods to achieve rapid, precise, and dynamic tasks by developing accurate models and using machine learning studies to optimize trajectories.

Chapter 6 is a conclusion on this work on soft contact and a proposal of future work and applications for the methods, mechanisms, and concepts presented in this thesis.

1.5 Previously published manuscripts

Much of the content of this thesis has been published in the following manuscripts:

- Galloway KC, **Becker KP**, Phillips BT, Tchernov D, Wood RJ, Gruber DF, “Soft robotic grippers for biological sampling on deep reefs,” *Soft Robotics*, vol. 3, no. 1, pp. 23–33, 2016. (Cover Article)
- **Becker KP**, Bartlett NW, Malley MJD, Kjeer PM, Wood RJ, “Tunable friction through constrained inflation of an elastomeric membrane,” *IEEE International Conference on Robotics and Automation*, Singapore, May, 2017.
- **Becker KP**, Chen Y, Wood, RJ, “Soft actuator arrays: mechanically programmable

dip molding of high aspect ratio soft actuator arrays,” *Advanced Functional Materials*, 2020, Wiley Online Library. (Cover Article)

- Bartlett NW, **Becker KP**, Wood, RJ, “A fluidic demultiplexer for controlling large arrays of soft actuators,” *Soft Matter*, vol. 16, no. 25, pp. 5871–5877, 2020, Royal Society of Chemistry.
- **Becker KP**, Teeple CB, Charles N, Mahadevan L*, Wood RJ* “Grasping via entanglement,” 2021. Under review. (*co-advised)
- Bell MA, **Becker KP**, Weaver J, Wood RJ, “Injection molding for soft robots,” 2021. In preparation.

Chapter 2

Passive Contact Tuning

2.1 Introduction

In this chapter, I explore how the design, materials, and fabrication of digits for soft robotic grippers can be leveraged to achieve a grasp that is conformable to a large range of object sizes, a grasp that limits contact stresses, and a grasp that is robust (or secure). While these are useful traits in most robotic grippers, these qualities were particularly motivated by the application to deep-sea biological sampling. Consulting with marine biologists, we established desirable performance criteria for a soft robotic gripper including the ability to distribute contact and limit peak contact pressures, the ability to conform to the often irregular specimen shapes, the ability to alter the surface texture of the actuator, and the ability provide a sufficiently robust grip so as not to drop precious specimens in the collection process. The criteria were successfully achieved through the passive mechanics of the various materials and their arrangement, as well as the overall geometric structure of the grippers.

In deep-sea biological sampling, an ever present challenge is an abundance of uncertainty as to the specimen that will be encountered on a given excursion. The pilots of unmanned submersible vehicles or ROVs (Remotely Operated Vehicles) must be prepared to pick up a variety of specimen, some of which they may have never seen before, using teleoperated robotic arms and manipulators. The lack of predictability is especially present for missions in previously unexplored territories and it is estimated that less than 0.0001% of the benthic regions in the world beyond 200m of depth have been explored [6]. Space and payload capacity for available tooling is limited on an ROV, so dive missions are often

constrained to a limited variety of tools loaded on the vehicle to accommodate the different specimens encountered. Also, with time required to travel to sampling depth is on the order of hours, vehicles usually remain at depth for long missions of several hours up to full days without the vehicle returning for repairs and tool changes. To accommodate the uncertainty of the dive conditions and target specimen, we set out to design a gripper that could accommodate a large variety of specimen sizes and shapes while providing a gentle and secure grasp.

In addition to the uncertainty going into a dive mission, deep-sea biological sampling is a particularly challenge grasping task that highlights the potential advantages of soft robotic grippers, as well as opportunities to advance the state of the art. An example specimen and grasp that embodies several challenging traits is shown in Figure 2.1. The crab in these pictures has an irregular shape that complicates grasp planning, it requires gentle contact to prevent damage, it was visibly obscured by marine snow, it was highly mobile, and it retreated under an obscuring outcropping of rock. ROV pilots responsible for operating the rigid manipulators that would typically be used for this task have developed an enormous amount of skill in compensating for these challenges. However, soft robotic grippers can accommodate much of the uncertainty related to the specimen and limited vision. Soft robotic grippers can also passively limit applied forces and adapt to irregular object shapes, thereby simplifying grasp control. Furthermore, soft grippers can allow the pilots to spend less time (and stress) on particularly challenging specimens and cover more area of exploration during precious dive time. The challenges above are exacerbated by deep-sea conditions but are valid challenges in all grasping tasks, aquatic and terrestrial. By addressing them in this challenging environment of limited access, limited visibility and feedback, thousands of pounds of hydrostatic pressure, low temperatures, and corrosive salinity, we believe the same principles can be applied to less adversarial environments.

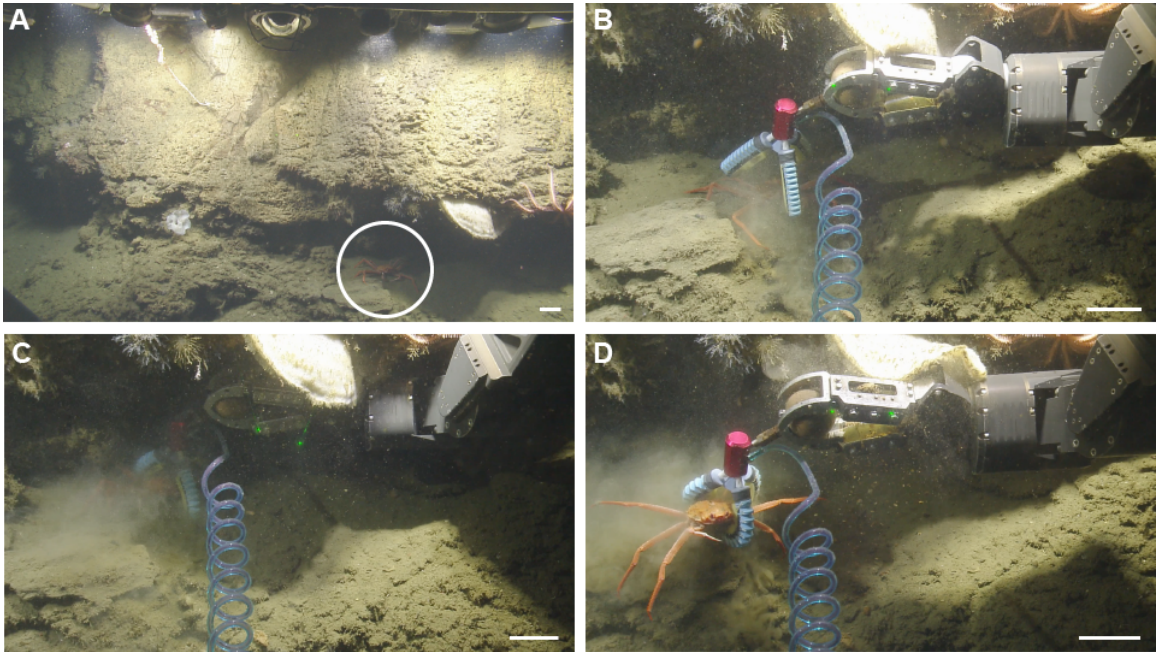


Figure 2.1: Field testing of an early generation of our deep-sea soft robotic gripper picking up a crab. The crab grab required a gentle touch while accommodating an irregular shape, avoiding the obstructing boulder, following a moving target, and working with little to no visibility. The scale bar in each panel represents approximately 10cm in the incident plane of the green lasers used for a visual size reference. After picking the crab up, it was safely returned to the sea floor from which it came.

2.2 Motivation: deep-sea biological sampling

Representing 95% of the world's ocean by volume, the least explored biome on Earth is the deep sea [6]. Various hot spots for unique biological diversity and genetic adaptations have only recently become accessible to scientists due to advances in ROV and submersible vehicle technology [7]. While Darwin described corals from depths reaching 128 m in 1889 [8], and the expeditions of the Challenger in the 1870's provided the discovery of thousands of species, the majority of benthic deep ocean area has yet to be explored [7]. Exploration and understanding of these areas is increasingly important as an estimated 19% of the world's shallow coral reefs have recently been lost, with a further 35% expected to disappear in the next 40 years [9]. Reefs occurring at depths greater than 30 m are somewhat buffered from human and natural disturbances and represent a potential refuge [10, 11]. But deep reefs remain dramatically understudied compared to other highly diverse habitats [12, 13]. Only with the relatively recent development of technical diving, ROVs,

and submersibles has it also become possible to make in situ observations of deep-sea fauna. In the last few decades, this increase in access has greatly expanded mesophotic reef biology [14, 15, 16, 17], and increased our awareness of the diversity of species, (a majority of which are believed to be not yet identified) that are also likely unique to a various deep-sea habitats such as vents, seamount coral gardens, whale-falls, and trenches [18].

Development of deep-sea ROVs has made this under-explored biome more accessible, but biological collection and study remains a challenging task. Robotic manipulators are required to collect and handle animals below depths accessible to technical divers. Commercially available manipulators that are designed to withstand and operate in deep-sea conditions have historically been developed for the oil industry. This translates to rigid grippers that are designed to apply gripping and lifting forces up to 2.2 kN (500*lbf*), and this is not ideal for picking up delicate specimens [19]. Some advanced systems incorporate feedback, but the force threshold to trigger feedback to an operator is sufficient to destroy a biological sample. From speaking with ROV pilots, we have come to understand that they often turn off the haptic feedback of the manipulators during their most delicate and sensitive tasks. They explained that it is more likely to disrupt concentration than provide meaningful feedback in the moment. Less expensive grippers tend to lack feedback or the feedback is not intuitive and thus not useful.

The industrial nature of available rigid deep-sea gripper options causes a major challenge for researchers valuing delicate specimens. Deep reefs are known to have slow growth rates and their populations are suffering from seasonal bleaching events [20] so it is of the utmost importance to take steps to study these ecosystems for the purpose of their preservation but to also minimize any potential damage while doing so. Furthermore, molecular biology and biochemical analysis of these animals can be affected by induced stress responses so, in addition to minimizing damage to the ecosystem overall, care must be taken to minimize stress applied to the specimen before RNA stabilizers (such as RNAlater) can be used. These chemicals are applied to stabilize the sample for further transport and sequencing, thereby facilitating gene expression and transcriptomic analysis performed on these animals [21, 22]. The compliant materials of soft robots offers an option that provides an inherent advantage in conforming to natural materials and environments, distributing contact, and minimizing contact stress on soft or fragile organisms. A recent jellyfish study confirms that the stress response associated with the use of an ultra-gentle soft gripper is minimal [23].

2.3 Background and prior art for compliant grippers

Soft robotics is a growing alternative to rigid robotic systems, providing a safer alternative for robots to interact with and operate in close proximity with living organisms [24, 25, 26, 27, 28, 29, 30]. By using soft materials instead of more traditional metals and hard polymers, robotic components can closely mimic the properties of natural systems. Grippers made of materials with a stiffness on the same or similar orders of magnitude to their target object are more likely to conform to natural systems, thereby reducing forced deformation and damage to those systems.

Underactuated and compliant grippers have proven to be a robust option for manipulating a wide variety of object shapes and sizes in unstructured environments. Recent research from Stanford University explored the development of a compliant, underactuated gripper to augment human capabilities and reduce strain related injuries for professional divers working at depths up to 100 m. Their gripper mimics the grasps needed to manipulate welding equipment and power tools that would otherwise be used by human hands [31]. The design and actuation of the compliant underwater gripper demonstrated by Stanford is similar to the shape deposition manufactured hand developed at Harvard, using a single tendon to drive each finger and coupling the rigid polymer phalanges of each finger with elastomeric flexure joints [32].

Similar to underactuated, compliant hands, fully soft robotic grippers are adept at adapting to variations in object size and shape. Furthermore, soft robotic systems are ideally suited for gripping and manipulating delicate objects and complex shapes by conforming to the object's shape and distributing grasping forces. Soft systems also offer improved safety as these pneumatically and hydraulically actuated soft materials are inherently safe for interfacing with humans and animals due to their natural compliance and ability to be back-driven [26, 33]. Suzumori conducted some of the earliest work on soft robotic grippers where he created continuum-style soft actuators that consisted of three parallel, fiber-reinforced elastomeric chambers that were spaced evenly around a central axis. Coordinated fluid pressurization of the actuators' chambers can produce multi-degree of freedom bending, and can be used as fingers to create soft robotic grippers [34]. Lane et al. designed a soft robotic subsea hand with tri-chamber continuum actuator fingers similar to those demonstrated by Suzumori; however, we were unable to find any record evaluating the gripper on an ROV or in open water [35]. In addition to soft grippers, several soft robotic continuum arms have

also been developed for the purpose of grasping. Two such arms preceding this work, the OCTOPUS robot by Chianchetti et al. [28] and the OCTarm by Walker et al. [36], have demonstrated grasping in relatively shallow waters, but have not operated at significant depths. Since the first generation of our gripper, a number of shallow water soft grippers and crawlers have also been demonstrated, most for shallow water exploration [37, 38].

The distinction between a capacity for grasping and manipulation is important and the soft grippers presented in this chapter were developed with the primary goal of gentle grasping and are capable of power grasps but not precision grasps and no more manipulation than moving an object from one location to another. The following chapter, however, introduces a direct successor to the bellows-type gripper that incorporates active friction tuning to the gripper surface. This ability to actively modulate friction and surface traction adds a level of dexterity to the gripper and capacity for simple manipulation that starts to reassemble the capacity of some simplistic rigid manipulators [39]. Another two successors to the bellows-type gripper described below are grippers by Teeple et al. [40] and Abondance et al. [41], which add the ability to switch between a power grasp and precision grasp, and a capacity for in hand manipulation, respectively. There are also several examples of more complex, anthropomorphic soft grippers that use a similar construction to the boa-style actuators discussed in this chapter and the fiber-reinforced actuators on which the boa-type actuators are based [42, 43, 27]. Conversely there is also a wealth of grippers that break from digitated designs and prioritize conformability and gentle grasping over a potential for manipulation, employing strategies that include suction cups, jamming enclosures, and enveloping shrouds driven by positive or negative fluidic pressures [44, 45, 46, 47]. These gripper are all fluidically actuated but there are, of course, a wealth of soft grippers and manipulators that range from simplistic to complex and represent a variety of actuation modes [47].

The soft robotic actuators that create the ‘digits’ of our grippers are monolithic composite structures and are modularly coupled to a rigid palm. The simple construction, inexpensive materials, and modular design of our soft grippers allow one to quickly modify or repair a system in the field with minimal expense or mechanical expertise. The palms are connected to a wooden ball that a rigid manipulator like the Predator (Kraft Telerobotics) can retrieve from a tool holster on the ROV. A typical ROV, with a predator robot arm and rigid manipulator are shown in Figure 2.2A. The soft gripper holster is also visible on the ‘front porch’ of the ROV. Operation of the soft gripper at the end of the rigid manipulator,

can be seen in Figure 2.2B. A closer view of one of the grippers holding a holothurian (a sea cucumber) is also included in Figure 2.2C. The soft fingers are modularly attached to a palm, which is in turn connected to the wooden ball. The fingers, palm, ball, and hydraulic connections can all be individually replaced or repaired.

Two different forms of soft actuators (described further in Section 2.4) were used for the soft robotic deep-sea gripper and are interchangeable on the red palm that is visible in Figure 2.2C. The structure and operating principles of the actuators is based on the PnueNet, fast-PnueNet, and fiber-reinforced soft actuators developed at Harvard [26, 48, 27], with modifications to achieve increased stiffness in an actuated state, more conformal grip over a larger range of object sizes, higher burst pressure, and higher cycled pressure to failure. With these modifications, they have successfully been used for biological sampling tasks at depths greater than 3.5 kilometers underwater in field-testing. These modifications are described in section 2.5 of this chapter.

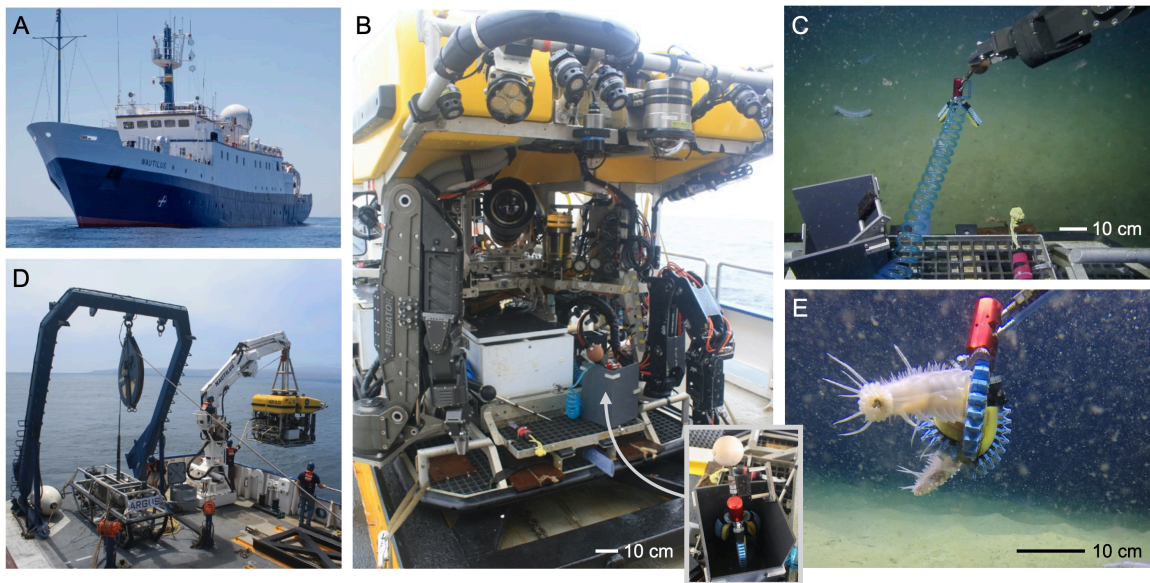


Figure 2.2: (A) The Nautilus, Ocean Exploration Trust’s research vessel on which most of the field testing was performed. (B) Front view of Hercules, the ROV that operates from the Nautilus. The rigid robot arms used for deep-sea biological and geological sampling are visible on the front corners of the ROV. Also visible is a soft gripper in a tool holster on the ‘front porch’ of the ROV that is accessible to the rigid manipulator. The inlay shows a view into the top of the holster. (C) During operations, the soft gripper is held in the rigid manipulator by a wooden ball. (D) A picture of the back deck of the Nautilus while the ROV (Hercules) was being launched for a field test. (E) A close-up image of the soft gripper holding a holothurian at a depth of 1800 m in Arguello Canyon, off the coast of California.

2.4 Two hydraulic soft actuator architectures

Two different soft actuator architectures used as the basis for our grippers are presented below – fiber-reinforced and bellows-type architectures. They have previously been introduced in the field of soft robotics and were chosen and modified for use in deep-sea biological sampling as described in Section 2.5. These fluidically-actuated architectures are a natural choice for incorporation into deep-sea ROV platforms because they can be hydraulically actuated using commercially available pumps that are rated for and used in deep-sea operations. With an incompressible working fluid, the actuators can operate on a differential pressure and are resilient to enormous hydrostatic pressure (in excess of 35MPa). Furthermore, the silicone rubbers and plastics that we use to create these actuators are inert to the corrosive saline environment, allowing us to pull in salt water from the surroundings to power the actuators. By avoiding the use of hydraulic fluids, a leaky actuator poses no risk of contamination.

Actuation of the fiber-reinforced architecture is dominated by a strategic arrangement of composite materials to allow tensile strain in some regions and impose directional restrictions in other regions. By contrast, the bellows architecture leverages more geometric reconfiguration and relatively low strain values to achieve actuation. (Although we will detail the incorporation of strain-limiting elements on the bellows-type architecture as well.) Some of the work detailed in this chapter applies to both architectures, but focus is more heavily applied to the bellows-type actuator because more of the novel contributions in this work were applied specifically to that architecture. The fiber-reinforced actuator can be built to operate at higher pressures than the bellows-style architecture and can be mechanically programmed to achieve complex motions that couple bending and twisting motions, which would be difficult to replicate in a bellows-style actuator. Preference toward the bellows-type gripper, however, was motivated by the fact that the fabrication process could be made simpler and faster than that of the fiber-reinforced grippers. The bellows architecture could also be successfully applied to more of the required biological sampling tasks than could the fiber-reinforced architecture in field testing. Both actuator types are described further below.

2.4.1 Boa-type actuator

The fiber reinforced actuator, referred to here as a boa-type actuator, was fabricated based on the method developed by Polygerinos et al. for molding elastomeric tubular bladders with embedded fiber-reinforcements to program the material’s strain response to a pressurized fluid input [27]. With this technique, the fiber reinforced actuators can be mechanically programmed to execute complex motions as determined by the arrangement of strain limiting elements or fibers. The ‘mechanical program’ that prescribes the complex motions can be changed between actuators but is fixed once the actuator is fully fabricated. A finished actuator will always repeat the same motion unless disrupted by external objects and forces. Inspired by the boa constrictor and tentacled cephalopods, we implemented an arrangement of uni-axial glass fibers and Kevlar thread to program the boa-type soft actuator to coil around target objects. The boa-type gripper can access tight spaces, and reversibly shape change from a cantilevered straight beam to a helical structure around a target object. This coiling behavior is demonstrated on a sea whip in the Red Sea in figure 2.3.

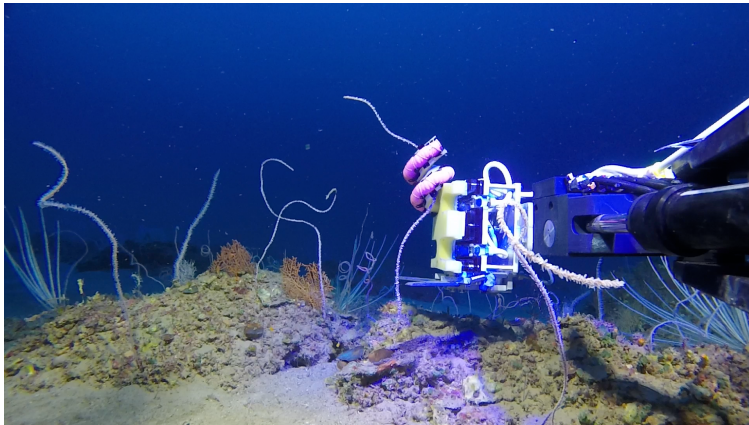


Figure 2.3: Picture of boa-type gripper coiling around a sea whip in the Red Sea at a depth of approximately 100 m.

As mentioned above, the path of motion is dependent on the actuator geometry, elastomeric material properties, and fiber-reinforcement placement. The unencumbered path, as shown below in Figure 2.4, is always repeated in the absence of external forces and obstacles. The compliance of the actuator gives it the ability to bend and comply to objects, thus tolerating greater uncertainty of sample size, location, shape, and stiffness. As interior

fluid pressure increases, the 300 mm long (and 15 mm wide) actuator wraps around an object to increase surface area contact and distribute forces. The boa-type actuator we developed for field-testing was designed to wrap around objects as small as 12 mm in diameter. The operating pressure used throughout the tests and images shown is approximately 310 kPa (45psi) unless noted otherwise, though the actuators can be easily programmed to operate at higher and lower pressures by adjusting the geometry, material stiffness, and spatial density of fiber-reinforcements.

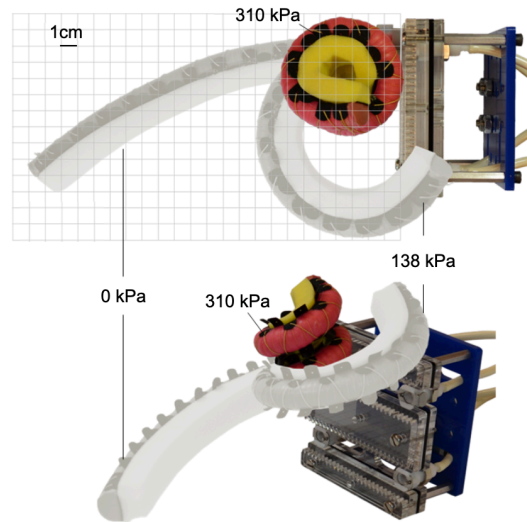


Figure 2.4: Pressurization path of motion of a boa-type gripper in the absence of external forces and obstacles.

2.4.2 Boa-type actuator fabrication

The boa-type actuator fabrication process, shown in Figure 2.5, begins with molding a bladder on a semi-circular stainless steel rod that is suspended inside of a 3D printed mold. A 2 mm gap between the rod and interior mold walls determines the bladder skin thickness. The interior walls of the mold also include grooves that will later guide the winding of the kevlar fibers that contribute to the bending motion of the finished actuator. The rod and mold are 300 mm in length. The mold parts were printed in Vero Clear and Tango Blue Stratasys resin on Objet Connex and Scholar printers. The rod is held in place by a top cap, which is the small part visible in figure 2.5A. On the other side of the molding assembly, a pin is press-fit into the end of the rod that aligns with a hole in the

printed mold. The mold is first sprayed with mold release and then clamped together in a vertical orientation without the rod or cap. The rod does not need to be coated with mold release and is not yet inserted into the molding assembly. We use a 30A shore hardness rubber, Elastosil M4601A/B (Wacker Chemie), for the internal bladder. The rubber is mixed with a thinky centrifugal mixer for a total of 120 s at 2000RPM and poured into the mold. The mold is degassed with care taken to avoid overflow as trapped bubbles expand. After degassing, the half-round rod is pushed into the mold until the pin is pressed into its alignment hole. The cap is placed over the top portion of the rod and mold, and the full assembly, as shown in Figure 2.5B, is left in a room temperature pressure chamber to cure overnight. (The reason for a room temperature cure is that the Vero Clear and Tango Blue resin will soften at elevated temperatures and deform under the pressure of clamps.) Once the rubber is fully cured, the rod is removed from the mold with the rubber in place, as shown in Figure 2.5C. The bladder remains on the rod for the next few steps and it is helpful to clamp the exposed end of the rod in a vice.

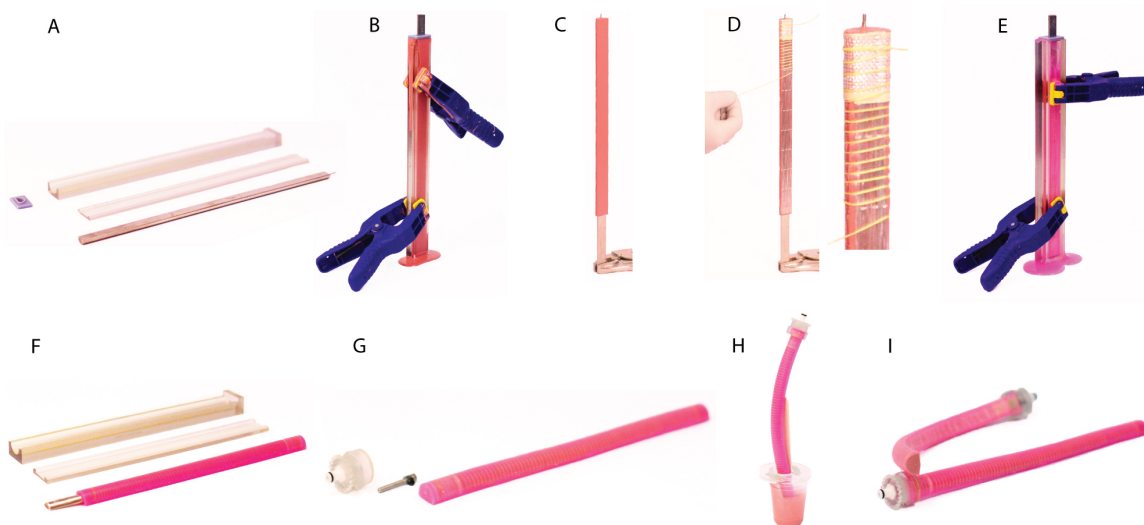


Figure 2.5: Pictures showing the fabrication process of boa-type grippers. (A) 3D-printed molds are used to cast the inner bladder of the actuator. (B) Casting of the inner bladder. (C) The Bladder is released from the mold and (D) covered with fiber reinforcements. (E) An outer layer is cast around the assembly to cover the fibers reinforcements. (F) The Actuator is removed from the second mold. (G) The half-round rod is removed and connective hardware is stalled through the open end of the actuator. (H) The open end of the actuator is sealed with rubber. (I) The final length of the actuator is 290 mm.

Nonwoven glass fibers are glued to the flat face of the bladder with a silicone glue such as Silpoxy (Smooth-On). This can be replaced with a fine metal mesh or fabric. The glass fibers were chosen because they had the lowest occurrence of delamination or tearing during cyclic testing. A strip of woven glass fibers is then glued around the pinned tip of the bladder and over the non-woven glass fibers as shown in Figure 2.5D. The edges of the woven strip should fully overlap on the flat face of the bladder. Kevlar thread is then wound around the bladder and fibers, following the guiding grooves mentioned above. The pitch of the winding can be modulated to change the bending motion of the resulting actuator [49], however we maintained an even pitch to achieve a constant curvature with the boa actuator. A second mold, similar to the first but larger in diameter, is used to then cast a skin around the wound bladder. The larger mold is sprayed with mold release, clamped, filled with mixed Dragonskin20 (Smooth-on), and degassed. (One might notice that the rubber in Figure 2.5E does not have the typical color of the elastomers listed. Pink fluorescent dye was added to increase visibility under black light. This was to help visualize the gripper while operating in low-light settings with a black light to investigate fluorescent animals.) Once again, the rod, now with windings, is pushed into the rubber until the pin fits into an alignment hole at the base of the mold and a cap is put in place to keep the rod centered within the mold. The assembly is then placed into a pressure chamber and left to cure at room temperature overnight. Isopropyl alcohol squirt inside the actuator can help to slip it off of the rod after curing.

Once de-molded, and the rod removed, the actuator is plumbed with hardware to attach to the modular deep-sea gripper palm and the open tip is sealed. The hardware before installation is shown in Figure 2.5G. A vented screw with a laser-cut acrylic half-round washer to match the interior cross-section of the actuator is pushed down into the tip of the actuator. The vented screw is pushed through the hole from the mold alignment pin and screwed into a quick-disconnect fitting (McMaster PN:5012K46) that is modified with internally tapped threads to match the vented screw. The quick-disconnect fitting is also installed into a 3D-printed cap. Before screwing the hardware together, the 3D-printed cap is lightly filled with sil-poxy to help ensure a seal. The tip of the actuator is then also back filled with rubber and left to cure to seal the open end.

2.4.3 Bellows-type actuator

Bellows-type soft actuators are a common architecture that creates asymmetric motion by unfolding the excess material in the bellows. Compared to fiber-reinforced actuators where the elastomer material must undergo significant strain to create motion, this unfolding approach places less strain on the material, which can increase the longevity of the actuator and lead to lower operating pressures. Bellows-type actuators also have the advantage that certain geometries can support bi-directional bending by alternating pressurized fluid and vacuum, as demonstrated in Figure 2.7. Furthermore, fiber-reinforcements can be incorporated into bellows-type actuators to increase the actuator’s operating pressure and output force, and reduce its radius of curvature when actuated.

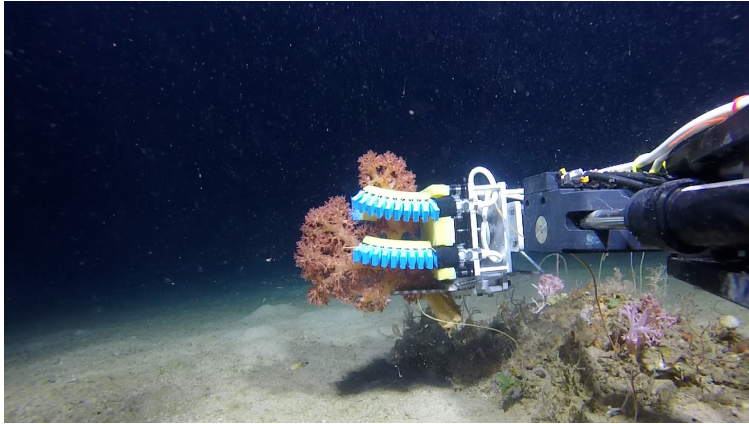


Figure 2.6: Picture of first generation bellows gripper picking up soft coral in the Red Sea at a depth of approximately 100 m.

2.4.4 Bellows-type actuator fabrication

The first step in fabricating a bellows-type soft actuator begins with molding the soft core, (first introduced by Galloway [19]), which will define the internal geometry of the final actuator. This was introduced with our first generation of the deep-sea soft robotic gripper. The soft core must be molded prior to starting the bellows-style finger. Similar to the fiber reinforced actuators, the molds are 3D printed in Tango Blue and Vero Clear resin from Stratasys. The soft core is molded in silicone (elastosil M4601 by Wacker Chemical) using a 3D printed two-part mold. Two stainless steel rods are co-molded with the core, as skewers that support and align the core in later molding steps. The core should then be

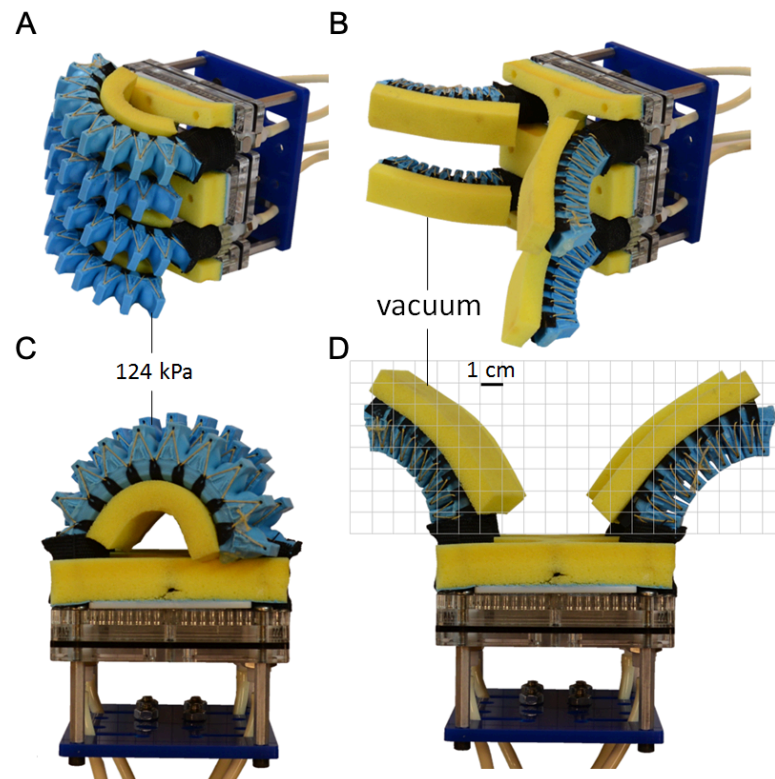


Figure 2.7: Range of motion of the bellows actuator under vacuum and 124kPa .

liberally coated with mold release and set aside to be incorporated in the molding of the actuator, as shown in Figure 2.8C.

A second 3D printed mold, shown in Figure 2.8A, defines the outer geometry of the soft actuator and is prepared by applying mold release to all interior surfaces. Pins (or side pulls) are also added along the bottom of the mold to create through-holes at the top of each bellow nod. These features serve as anchor points to add reinforcements, bridging materials, and other functions to the actuator discussed further in Section 2.5.2. The pins, visible in Figure 2.8B, are stainless steel and thus do not necessarily need mold release. The silicone (Smooth-Sil 950 by Smooth On) for the bellows-type actuator is poured into both halves of the mold. When casting these actuators, care should be taken to minimize air entrapment, particularly when pouring rubber into the bellow cavities and around the pins. To extract bubbles, the mold halves with freshly poured silicone, as shown in Figure 2.8B, are placed under vacuum for several minutes, along with any excess mixed rubber that may be used to top the mold off later in the process.

As shown in 2.8C, after the soft core is inserted into the mold, and soft core skewers are gently pushed into alignment slots built into the mold. The positioning of the core on its skewers is critical to the alignment of the cores inside of the mold. This is defined by the distance between the tip of the core and the tip of the skewers, which is set in the core molds. When reusing a previously used core, this distance should be checked by reinserting into a core mold. After the core is in place, the two halves of the mold are brought together and clamped (Figure 2.8D). This should be done quickly, but the mixed viscosity of Smoothsil 950 is high enough that rubber does not run quickly when the mold is tipped upward. The base of the mold halves should be aligned first and then hinged closed so that bubbles are pressed upward and exit through overflow ports at the top of the mold, along with excess rubber. The mold is then left to cure in a pressure chamber at room temperature overnight. This step compresses any bubbles that might lead to a pin hole in the walls of the actuator, which are only 2 mm thick, (2.7 mm in later versions).

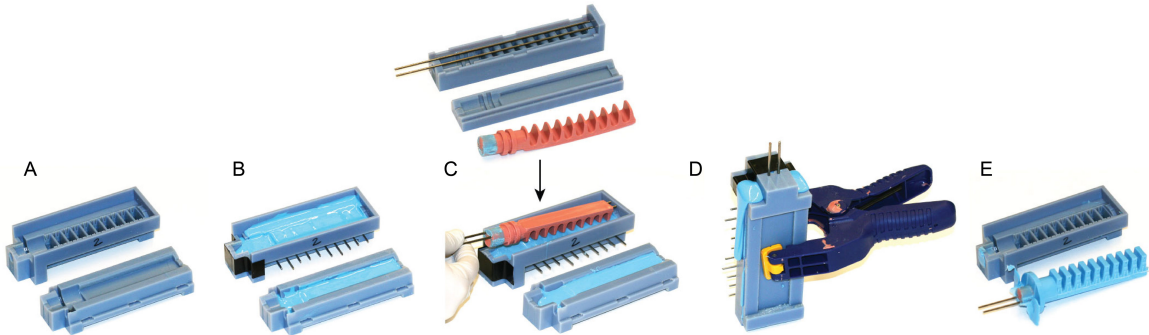


Figure 2.8: Pictures showing the molding process of bellows-type actuators, beginning with (A) a 3D-printed mold. (B) Pins are placed in the mold to define holes that will later be used for reinforcements and a two-part silicone is poured into either side of the mold. (C) A previously molded soft core is positioned into the freshly poured silicon and (D) the mold is clamped together. (E) After curing in a pressure chamber, the pins are removed and the actuator and soft core freed from the mold. This process is continue in Figure 2.9. The center to center spacing of the bellow nodes is 10 mm and the finished actuator in Figure 2.9 is 128 mm in length.

Once the silicone has cured, the side pulls can be removed and then the actuator and core liberated from the mold. The soft core skewers extend beyond the end of the actuator and are removed next, which leaves two small holes at the end of the actuator face that is pointed away in Figures 2.8 and 2.9. These can be plugged with a small amount of silicone glue (e.g., Sil-Poxy by Smooth On). The flange at the base of the actuator in

Figures 2.8E and 2.9F is included to help removed the soft core. In Galloway et al. [19], the flange is used to couple to vacuum pressure to help pull outward on the actuator walls while removing the soft core. In successive generations of the bellow actuators, I no longer use a vacuum for removal but included the flange as a sacrificial feature to provide a small reservoir of rubber at the top of the mold to account for rising bubbles, as well as provide a place to grip while removing cores. In the final preparation of an actuator, the flange is cut off (Fig. 2.9G), and a 3D printed hub installed with a quick-disconnect fitting is glued into the open end of the actuator (Fig. 2.9H). Internal grooves defined by the soft core are complemented by the geometry of the 3D printed hub to help reinforce the glued interface. Kevlar thread is tied around the exterior of the base for further reinforcement (Fig. 2.9I) and tacked with Sil-Poxy. Black heat-shrink tubing is applied to the exterior in part to protect the wrapping but mostly for aesthetic purposes (Fig 2.9J).



Figure 2.9: Pictures showing the hardware installation for bellows-type actuators. The hardware allows for modular attachment to a deep-sea gripper palms. (F) The soft core is removed from the actuator and (G) the flange is removed. (H) Connective hardware is glued into the base of the actuator, (I) reinforced with Kevlar thread, (J) and covered with heat-shrink tubing. The finished length of the actuator from connector to finger tip is 128 mm.

A particularly important element of this fabrication process is the incorporation of the soft core, which forms the complex internal geometry that must be achieved for the bellows-style actuators. These were first introduced by Galloway [19] and I have added design guidance in Section 2.5.4.1 for soft cores, as well as for the molds for soft cores and actuators to double the burst pressures and achieve approximately five times greater cycling longevity than the original generation of the soft-core-molded bellows-style actuators shown above, as well as more durability in the soft cores themselves.

2.5 Creating gentle, conformal, and robust grasps

2.5.1 Rapid digital prototyping of geometric designs for large deformations

The large deformations experienced by the materials in soft robots make it difficult to create simple models with which to explicitly prescribe their motion. With the increasing availability and ease of additive manufacturing, it can be more pragmatic to take an experimental approach to understanding and mapping the key design parameters [48]. FEA (Finite Element Analysis) is also a powerful modeling alternative that has successfully been leveraged to optimize the performance of soft actuators [49, 50]. Artificial intelligence and machine learning has also been explored in the conceptual design of soft locomoting robots [51] as well as path planning for grasping and manipulation [52].

Empirical testing and simulations are all valuable tools for the development of future soft robots. I believe there is also potential value in a lighter-weight simulation platform to speed up the ideation and development process for novel soft actuators. Most of the tools and methods that we use to create soft robots were developed around characterization, design, and fabrication methodologies for rigid systems. This is important to note when considering the methods of prototyping a system will influence its eventual manifestation as well as its development and user perception at each stage of the development process [5]. Most engineers involved in machine and mechanism design learn to start by simplifying systems. We assume bodies are rigid and all deformations are relatively small. These assumptions do not translate well to soft systems and we consequently have less experience designing for soft systems with large deformations. Given that experience is required to develop expertise, a rapid digital prototyping tool for soft robotic structures can be helpful for a designer to quickly build experience in design for large deformations. Additive manufacturing of molds for soft actuators, (or of soft actuators directly), or creating robust and accurate FEA models can take hours to days to troubleshoot and complete. I propose a tool that exchanges precision for the purpose of ideation, similar to the concept of rapid prototyping. This does not replace physical tests or modeling, but augments the toolkit available in the early development process. A prototype of such a design tool is shown in Figure 2.10.

To explore the use of a rapid digital prototyping tool for soft robots, I built a

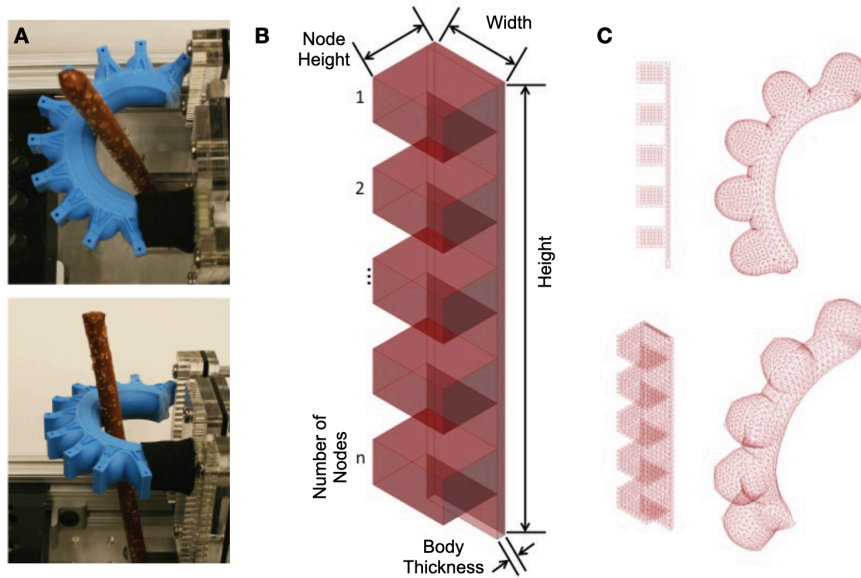


Figure 2.10: A simple model in which a (A) bellows actuator is approximated by a set of (B) parametrically driven faces (C) that are converted to a triangular mesh. The mesh acts as a network of springs that are pressurised by a normal vector at the centroid of each triangle. These models were built in Rhino and Grasshopper.

simplistic bellows actuator geometry to represent basic elements of the bellows-type actuator, similar to the one used for our soft deep-sea gripper. This actuator is shown in Figure 2.10A and its simplified form is represented in 2.10B as a parametric NURBS (Non-uniform rational basis spline) model. This was built in Grasshopper, which is a visual programming environment for Rhino, a commercial 3D computer graphics and computer-aided design (CAD) application software by Robert McNeel Associates. Within Grasshopper, the model is split into faces, converted to a triangular mesh, and stitched back together. An internal pressure is approximated as a normal force applied to the centroid of each triangle and the edges of the mesh are modeled as simple spring elements, the result of which is shown in 2.10C. The model can run in less than three minutes but does not take into account the thickness of the material and thus trades accuracy for low computational costs and quick iteration times. Similar to prototyping for the purpose of ideation, the quality of the simulation is intended for early exploration that can be validated and optimized with physical experiments or a rigorous FEA study.

The stiffness and pressurized deformation of the digital actuator was tuned to mimic the curvature of five nodes of the physical actuator in 2.10A. Those dimensions

were then used as a datum. The pressure and spring stiffness of the datum was then used to explore the effects of varying individual parameters of the geometry of a bellows-style actuator. Five characteristic parameters were chosen to describe the actuator geometry, as labeled in Figure 2.10B. Examples digital actuators with variances for each of the parameters are shown in Figure 2.11. For each example, only one parameter is modified and all other parameters are held constant to match those of the datum. Because the length of a node is coupled to the number of nodes and the height of the actuator, the node length was not independently varied. The model also does not incorporate interference from adjacent nodes, which is a point for further development. Issues arising from this interference can be seen in Figure 2.11, in the first variant that exhibits an increased number of nodes.

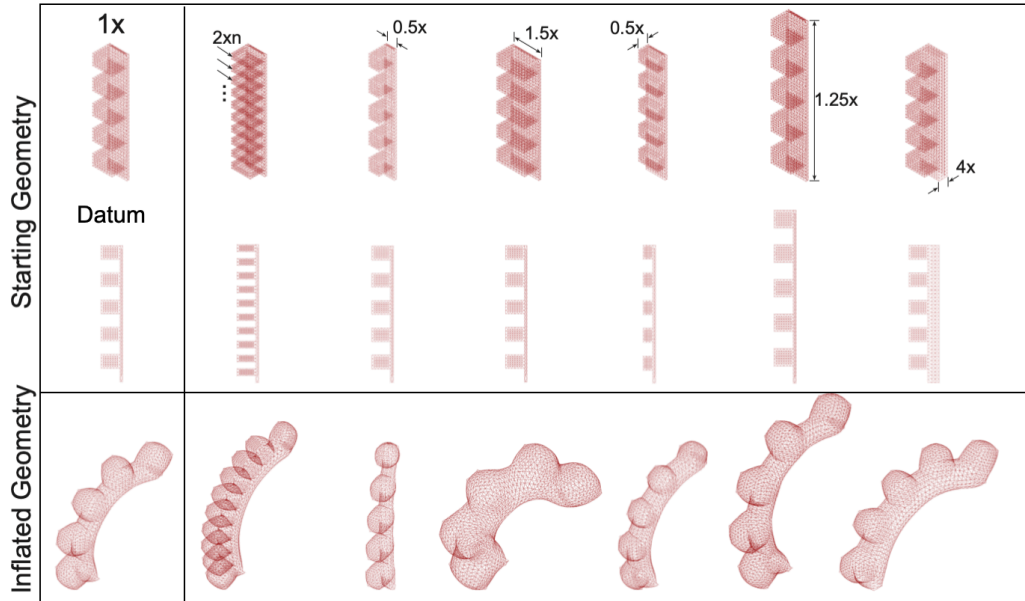


Figure 2.11: Table of rapid digital prototypes of a bellows-style actuator concept. The datum on the left serves as a reference case. Each of the variants on the right have one parameter modified from the datum actuators, as indicated by a dimension in the top row. Unless indicated otherwise, all other parameters match those of the datum actuator.

Exploring each parameter as an independent vector in a multi-dimensional design space does not capture the complex interactions between variables but can still help identify the salient impacts on performance. A number of performance metrics could be considered when building a cost function with which to compare the success of design variants. However, a simple starting metric is the deflection of an actuator given a fixed input pressure, as

shown in Figure 2.12A. The horizontal deflection of each digital actuator is normalized to the datum actuator and compared in the plots shown in Figure 2.12B. Each plot represents a different vector in the design space where, similar to the table in figure 2.11, only one parameter is varied and all others remain the same as the datum actuator. The deflection (normalized to the datum actuator) is plotted on the vertical axis and the varied parameters (also normalized to the datum actuator) are given on the horizontal axis of each plot. The dashed vertical line extending through each of the plots shows where the datum point intersects with each of the design vectors.

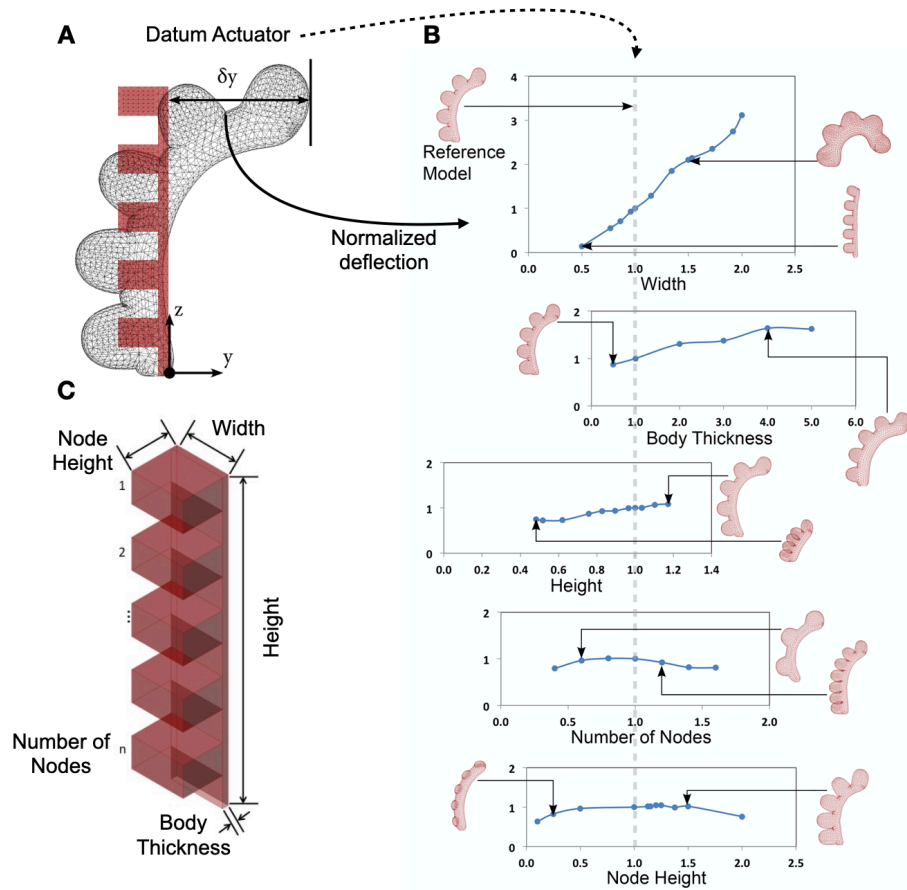


Figure 2.12: And rapid digital prototype exploration of the design space for a bellows-style actuator concept. (A) The horizontal deflection of the datum actuator is used to compare the performance of design variants. (B) Each parameter, normalized to the datum actuator, is individually varied while all other parameters are held constant for each plot. A dashed line indicates the intersection of the datum actuator with performance results each parameter exploration. (C) A reference schematic of the parameters being varied.

The plots in Figure 2.12B reveal the relative impact of varying different parameters in the geometric design of a bellows-style actuator. For example, changes in the width of the actuator creates the greatest slope while the height of the nodes has relatively little effect. As mentioned above, the exploration of varying the number of nodes is adversely affected by the model’s inability to resolve interference between the nodes and can be improved for future use. It is also worth noting that the model was constructed using a parametric description of orthogonal planar faces. Future iterations of this design tool should consider different approaches to building primitives that are less restrictive and more focused on leveraging large deformations for useful motion. As the field of soft robotics progresses, “light weight” rapid digital prototyping tools such as this could be a useful tool for early exploration performed before experiments and FEA. By reducing time and material cost, rapid digital prototyping can speed up the ideation process, increasing creativity while also building up experiential learning. While the model sacrifices accuracy, the low computing time also makes risky designs less costly and thus more accessible while also reducing the material waste associated with the prototyping process.

As applied to the design and fabrication of soft robotic deep-sea grippers, the rapid digital prototyping exercise revealed that, within reasonable manufacturing constraints, we would likely not achieve a conformal grasp with a single material bellow actuator. This lead to the addition of several materials to provide tighter grip closure, stronger grips, and lower contact pressure, as described in the following sections.

2.5.2 Modular strain-limiting elements

A simple lacing technique was introduced to reversibly modify the actuators, expanding the versatility of the soft grippers to be able to accomodate a larger range of object sizes. The lacing technique couples different textures to a bridging material, which is then laced to the actuator body. Ripstop nylon with a TPU backing was used as a bridging material because it is flexible, can be laser cut without unraveling or fraying), allows adhesive bonding to the nylon surface, and TPU films can be heat-welded to the TPU-coated surface. While this is a simple vehicle with which to attach various surfaces to both the boa and bellows-type actuators, it also adds fiber-reinforcements to the bellows-type actuator. For the bellows-type actuator, lacing has the added benefit of reinforcing the actuator and enabling it to operate at higher pressures (up to 170 kPa as opposed to 70 kPa without lace

reinforcements). Additionally, by restricting the radial deformation, the lacing redirects deformation of the actuator into the curling motion, thereby achieving tighter closure with the same operating pressure, as demonstrated in Figure 2.13.

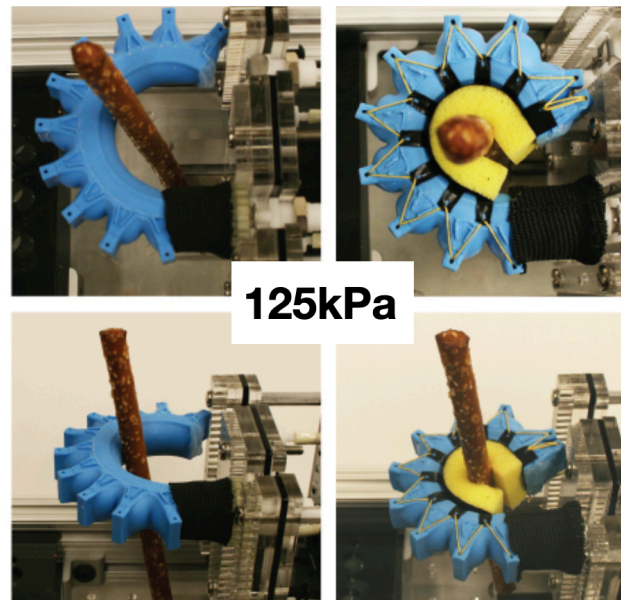


Figure 2.13: Pictures of a bellows-style actuator with and without lacing, bridging material, and foam. The actuation pressure is the same for both configurations, demonstrating that the lacing and bridging materials constrain radial deformation and thus tighten closure of the actuator. Foam attached to the bridging material creates a tighter internal radius, enabling the bellow to grip a pretzel stick (approximately 10 mm in diameter.)

Tighter closure of the gripper is achieved without increasing the inflation pressure, as shown in Figure 2.13 but the remaining gap to conform to smaller targets was achieved with an open cell polyurethane memory foam, further discussed in the next section. The lacing shown in in Figure 2.13 provides reinforcements and radial constraints to the bellow-style actuator, similar to the Kevlar windings cast into a fiber-reinforced actuator, but the bridging material also provides a platform with which to easily attach and replace materials and textures onto the gripping face of the actuators. The silicone materials use to create the actuators are ideal to withstand the harsh environments of field testing because they are tough and inert, but this also makes it difficult to bond to those surfaces with adhesives. The bridging material supports adhesives on the nylon side, and thermal bonded TPU on the TPU coated side. This allows for attachment of foam, connection interfaces for tools and instruments, or webbing between fingers of a gripper to help provide greater enclosure

of a grasped sample. Because the lacing is reversible, these coverings can also be replaced to minimize damage to the underlying actuator and refresh the surfaces of the actuator after extended use.

2.5.3 Mechanically programmed contact stress limits

The soft grippers in this work do not rely on sensors for force feedback, but are mechanically programmed to limit contact forces via the chosen materials and geometric design. This is important for biological material collection as well as underwater archaeology, where the pressure distribution around an object and the gripper's load carrying capacity are important to know before attempting a grasp. Some of the material selection is discussed below and I empirically examine the contact pressure and resistive forces of the boa- and bellows-type actuators in Section 2.6.1.

The materials, geometry, and internal pressure of an actuator are integral to the contact pressure that they apply. The bridging material from the lacing technique described above allows the additional incorporation of materials with a non-linear response to compressive strain on the contact interface of the grippers. This serves as a means to enhance the effect of mechanically programming stress contact limits integrated into the passive behavior of the gripper by using an open-cell low density memory foam. This is a lightweight and compliant material that provides a particularly non-linear compression response. In our observations, a 12.7 mm (0.5inches) layer of soft foam (Mcmaster-Carr, Inc., part: 86195K33) attached to the bridging material does not significantly impede an actuator's range of motion. As discussed above, the foam actually reduces the actuator's radius of curvature as it closes around an object, a useful feature for grabbing narrow specimens. Memory foam also has desirable non-linear stress-strain properties that help distribute forces and conform to irregular shapes. This non-linear behavior is demonstrated via a compression test, the results of which are shown in Figure 2.14. Several thicknesses and densities of open-cell memory foam were compressed in a materials characterization system (Instron 5544A). In all of the samples, the stress plateaus after approximately 10% compressive strain. The softer foams exhibit the longest plateau where stress is held around 2 kPa until nearly 50% compression, thus creating a contact pressure buffer.

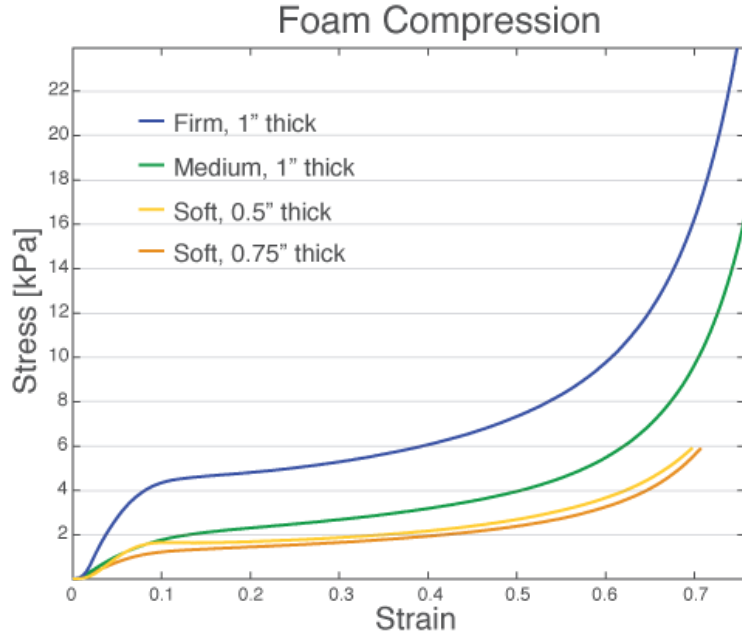


Figure 2.14: Plot of the stress-strain response when compressing the TPU foam attached to the interior of the gripper. The non-linear response is leveraged in designing for a stress-limited grasp.

2.5.4 Fabrication details to enhance cycle-life and burst pressure

While minor fabrication details are often relegated to an appendix, the relative nascency of soft robotics necessitates greater attention to the tools and methods that we use to create soft structures designed for large deformations. Just as we need to reconsider how to approach the design process, it is important to consider details of fabrication in the process of developing more robust and reliable soft actuators. I believe the reliability and robustness of soft actuators will be a limiting hurdle in expanding their utility, applications, and commercialization. The subsections below are included because they were important developments that I have not found in other literature, and have enabled substantially higher operating pressures and actuator life cycles with seemingly subtle or no changes in geometry, fabrication, and material considerations. The following fabrication adjustments have nearly doubled the burst pressure of the bellows-style actuators with and without strain limiting elements, respectively. More testing is required to assess statistical significance, but an initial cycling test suggests that the fabrication adjustments might at least quadruple

the number of cycles to failure of the bellows actuator.

2.5.4.1 Soft cores

The soft core molding method was a key improvement to the fabrication process for bellows-style soft actuators. The high aspect ratio features renders any rigid core mechanically constrained and can lead to damage to the core and the actuator body during demolding. Mosadegh et al. used a two-step molding technique where one-half of the bellow was molded and then bonded to the other half [48]. However, this introduces a materially weak seam along the actuator's entire perimeter and becomes the source of most actuator failures. The operating pressures in that work are also less than half of the operating pressures used for the deep-sea bellows grippers. Marchese et al. present a method where dissolvable cores are used to define the inner bellow geometry; however, this is a time consuming process requiring a new core for each new actuator and time spent dissolving the core [53]. Reusable soft cores introduced by Galloway help to overcome these challenges. This allows for the entirety of the soft digits to be molded in one step for a seamless soft body that can withstand higher operating pressures.

To maximize operating pressures, I found it is important to carefully trim the flashing or excess rubber from the parting lines. These should be trimmed to the surface of the core with a preference for cutting into a core over leaving excess flashing. Remnant flashing translates to a thin spot in the skin of the actuator after molding. This thin spot is structurally similar to a crack, due to the shape of flashing, and leads to stress concentration in the actuator wall and possible rupture. To facilitate trimming and mitigate deleterious effects of flashing, the parting line of a mold can also be moved to more accessible edges for trimming and place any defects in lower strain regions of the actuator. Injection molding in combination with higher clamping forces in mold assembly can also minimize flashing but care should be taken in this fabrication strategy because minimal flashing can be harder to trim and still detrimental to actuator robustness. Similarly, trimming flashing to the point where it is smaller but not eliminated makes successive trimming more difficult and still poses a risk to actuator robustness. A fresh razor blade or scalpel has been the most effective tool for trimming flashing while applying light tension to the flashing if there is enough to hold safely. Shorter or minimal flashing will tend to bend and slip beneath the blade and is challenging to trim effectively.

The silicon rubbers used for the soft cores were chosen for having a high elongation to failure to allow high deformation in the removal process and avoid plastic deformation so the cores can be reused. Elastosil was initially used for the soft cores and is still a preferable choice for its low cost and high elongation to failure (700%). However, True Skin 30 (Quantum Silicone) has a comparable price to the lines of Smooth-on products frequently used in soft robotics and touts a 1000% strain to failure. This is helpful for creating reusable cores for more complex internal geometries that require more deformation to successfully remove the core. It is also helpful in scenarios where there is a high ratio of surface area to core volume, which leads to higher forces applied to smaller cross-sectional areas. A shore hardness of 30A provides a balance of stiffness that can support its weight in the nodes of the bellows actuator (with the help of the stainless steel skewers mentioned above) but can also deform easily enough to facilitate removal. Elastosil and True Skin are able to endure higher strain and resist plastic deformation over similar 30A durometer two-part silicones used for casting.

2.5.4.2 Material compatibility and mold design

Similar to the stress concentrating effects of molding with soft cores with untrimmed flashing, artifacts from the 3D printing process can create thin spots and surface textures that are more prone to tearing. This was particularly true of vertical and overhung interior walls of molds that were made on the Polyjet printers (Object Scholar and Conex). Vertical and overhung walls require support material to hold tight tolerances on these features. Once the support material is removed, it reveals a roughness that is less than 1 mm in magnitude but, because the layer height at which the variation in wall thickness occurs is small, these can behave like minor cracks in the wall of the actuator and lower the burst pressure and cycle life of an actuator. To avoid this, all interior mold walls that define the inflatable portion of the actuator had at least a 1° draft angle. A draft angle is normally included in injection molded parts to facilitate removing rigid parts from a rigid mold. A draft angle is not strictly necessary for soft parts but was found beneficial for this purpose of creating a smoother molding surface and greater actuator longevity. Until making this change to the molds, every actuator failure point occurred within the regions that were defined by surfaces that once touched support material in the mold printing process. The problem of surface texture also arises with parts from FDM printed molds. This can be mitigated with

an acrylic spray coatings or partially dissolving the surface of the mold with Acetone vapor but these will also affect the mold fidelity. Another solution is to use alternative printing options such SLS (Selective Laser Sintering) of nylon or SLA (stereolithography) printed molds, though each comes with their own considerations and trade-offs.

The majority of molds used to make the deep-sea fingers were polyjet-printed in Vero Clear (Stratasys) because it was a readily available high resolution printer and the transparent mold walls facilitated the trouble shooting process. Another important caution is that a component in the poly jet resin also inhibits curing of most of the silicones used in this work. The issue of cure inhibition was also present with SLA parts made from the clear FormLabs resin. The issue becomes exacerbated as the ratio of the surface area to molding volume increases. To mitigate this, support material had to be thoroughly removed via a pressure washing station and molds were baked overnight in a 65°C oven. A sacrificial molding of rubber that would be thrown away (or several) was also a useful final cleaning step. A mold release can provide a minor barrier but will not resolve the problem of cure inhibition. If a part is cured enough to be removed from the mold but is still soft and tacky, removing it from the mold and continuing to bake it in an oven may partially resolve this issue. A more reliable solution, though, would be to treat this as a sacrificial casting, clean the mold of any residue, and start again. A sintered nylon part would not exhibit this cure inhibition problem but was not used primarily on the basis of cost and convenience.

2.6 Characterization of gentle, conformal, and robust grasps

2.6.1 Grasp contact pressure

Contact pressure tests of the forces between a gripper and target objects were intended to evaluate and demonstrate the inherent safety, form closure, and grasp strength of the chosen designs. A gripper's performance under these metrics can be adjusted easily through changes in geometry and materials. Several bench top experiments were performed to understand the magnitude of the force and pressure applied to static objects. A 63.5 mm diameter plastic tube was selected as the target object because both soft actuator types could cradle more than half the circumference of the tube and the radius of curvature was large enough to be wrapped with a Tekscan (model: 5051-20) pressure mapping sheet without damaging the sheet or inhibiting measurements. Several actuator configurations

were evaluated including the boa- and bellows-type actuators with and without memory foam. Figure 2.15, depicts the experimental setup and corresponding pressure map for the boa-type actuator. Pressurized to 310 kPa (45psi), the boa-type actuator without a foam texture had a narrow pressure distribution with most pressures ranging from 6 kPa-10 kPa, while the boa-type actuator with a foam inner surface had a wider pressure distribution with most recorded contact pressures below 5 kPa (0.72psi). The bellows-type actuators (pressurized to 69 kPa (10psi)) had a similar response where the maximum pressures detected were 2 kPa (0.29psi) and 7 kPa (1psi), with and without foam, respectively.

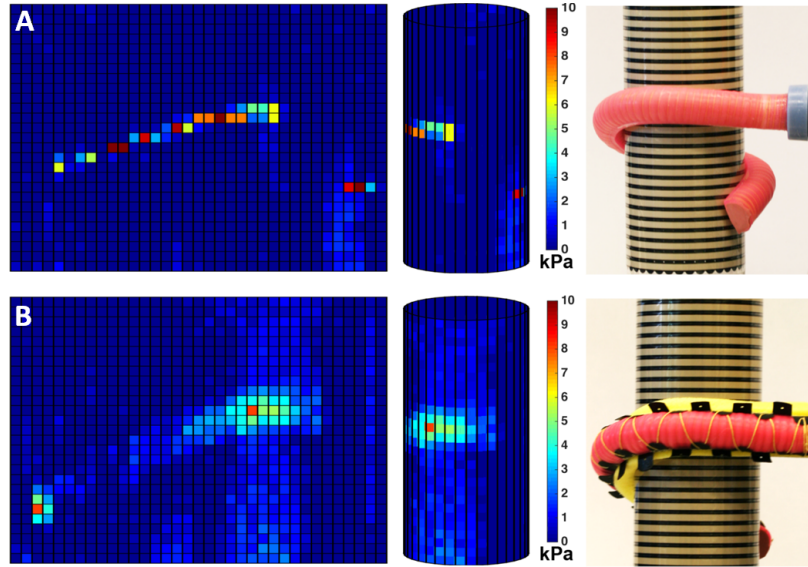


Figure 2.15: Map of the measured contact pressure of a boa wrapping around a 63.5 mm diameter cylinder (A) without and (B) with foam. The rectangular maps on the left show what the measurements would look like if unrolled to a flat sheet. The center map follows the orientation and experimental setup shown in the right-hand images.

2.6.2 Grasp strength

While the first design criterion of the soft deep-sea grippers is to provide a gentle grasp, it is also important for the gripper to have enough strength to securely pick up a sample and move it to a collection box on the ROV, withstanding gravity and inertial forces while moving through the water column. Given the added effect of buoyancy, drag forces while moving in the water is often the more substantial effect. Grasp strength was evaluated with a materials characterization system (Instron, model: 5544A single column)

that analyzed load-extension characteristics for several gripper scenarios including load direction and object size. In the experimental protocol, an acrylic tube ranging in diameter from 12.7, 25.4, and 50.8mm was positioned next to the palm of the gripper, and the actuators were inflated to their target pressures to enclose the cylinder. Figure 2.16 shows an example of a test with a bare boa wrapping around a 50.8 mm (2inch) diameter cylinder in a vertical orientation, as well as a foam-clad boa wrapping around a 12.7 mm (0.5inch) diameter cylinder in a horizontal orientation.

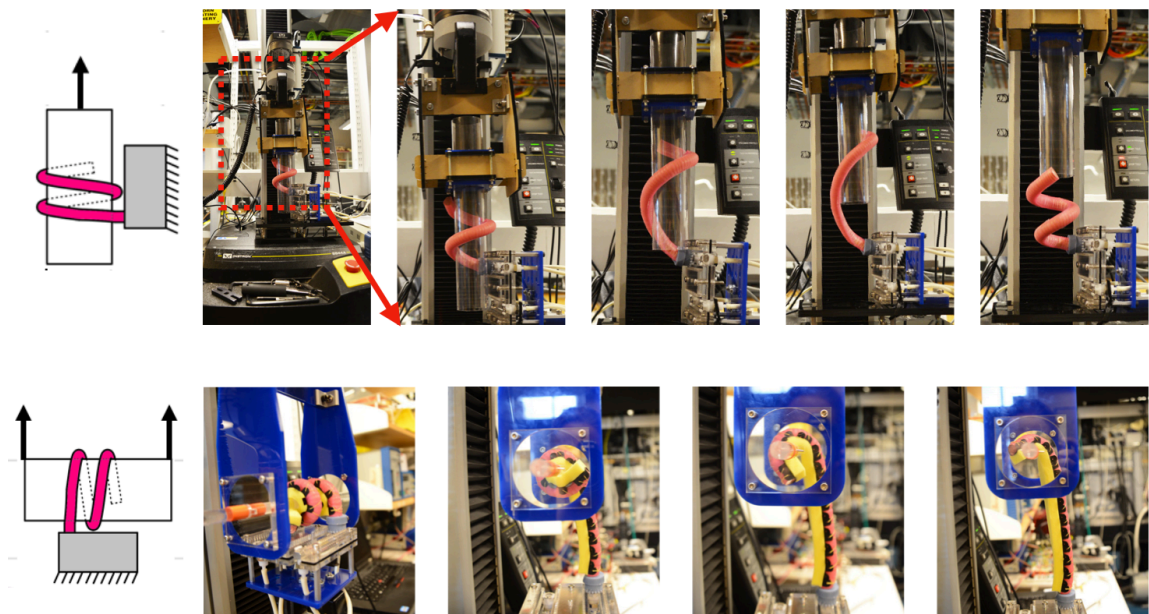


Figure 2.16: Experimental setup for grip force testing of a boa-style actuator without and with foam. Results of these experiments are shown in Figures 2.17 and ??

All bellows-type actuators were pressurized to 124kPa (18psi) and boa-type actuators were inflated to 310 kPa (45psi) with one exception where the boa-type actuator was pressurized to 345 kPa (50psi) to fully close around the 12.7 mm diameter tube. The grip strength of the bellows-type actuators were evaluated with two actuators, one opposing the other. The gripper was anchored to the table, and the Instron pulled on the tube at a fixed velocity (8mm/s) until the cylinder was pulled from the actuator’s grasp. Each test configuration was conducted five times and averaged. In the following plotted results, the solid black line is the average of the results while the shaded area represents one standard deviation. A comparison of the bellows-style gripper with foam and the boa-style grip-

per with and without foam closing around a 50.8 mm diameter in a vertical and horizontal orientation is shown in Figure 2.16.

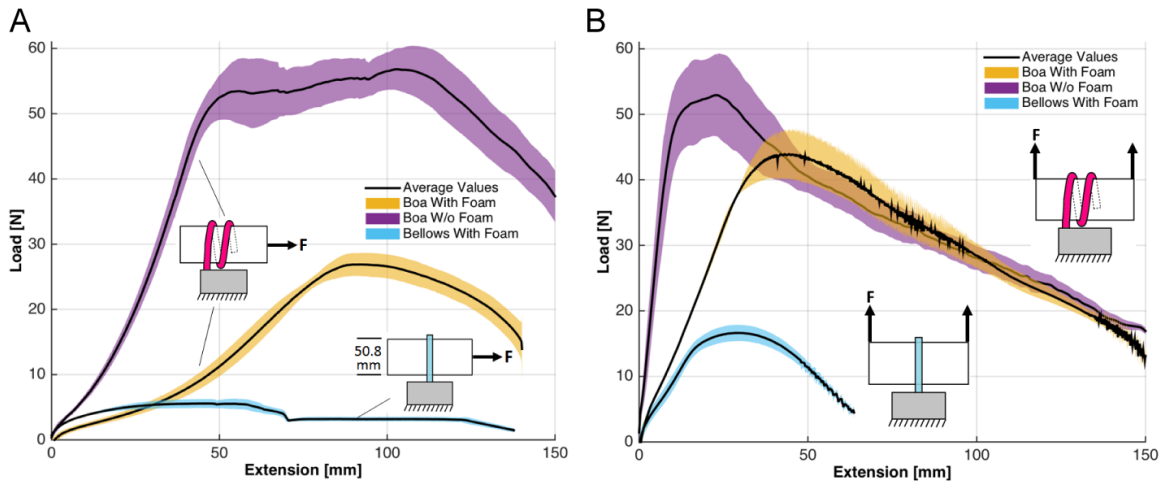


Figure 2.17: Grip force of a boa and bellows-style grippers as a 50.8 mm diameter tube is pulled (A) horizontally and (B) vertically from their grasp.

While gripping the 50.8 mm diameter tube, the bellows-type gripper had the greatest resistive force in the vertical direction (16.6 N) (Fig. 2.17B), and offered relatively little resistive force in the horizontal direction (5.6 N) (Fig. 2.17A). The boa-type gripper demonstrated significantly higher vertical and horizontal resistive forces across a range of tube diameters. In vertical pull tests with the 50.8 mm diameter tube, the boa-type gripper without foam had an average maximum holding force of 52.9 N, while peak average of the actuator with foam was 44 N (Fig. 2.17B). Furthermore, in experiments where the tube diameter was reduced to 25.4 mm and 12.7 mm, the hold force remained high compared to the bellows actuator (Fig. 2.18).

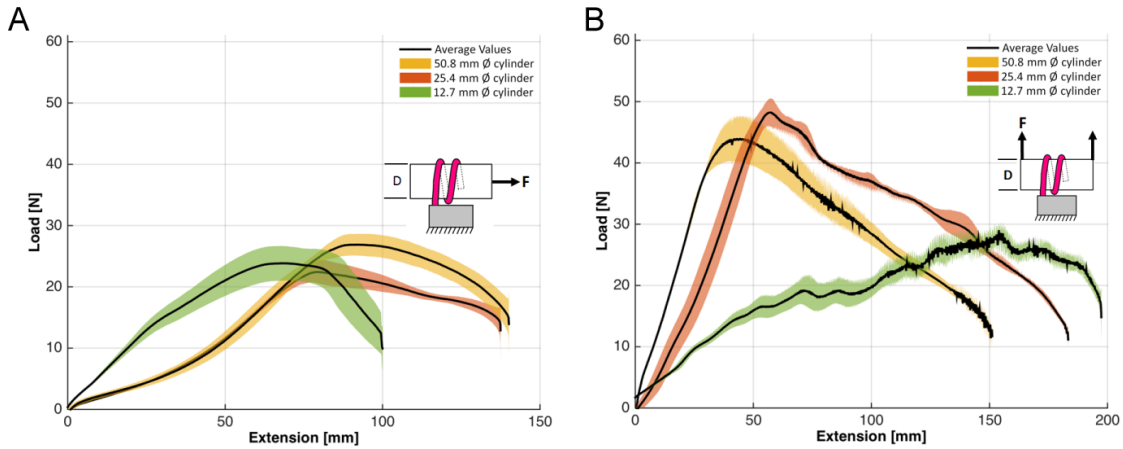


Figure 2.18: Grip force of a boa-style gripper with foam as a 12.7, 25.4, and 50.8mm diameter tube is pulled (A) horizontally and (B) vertically from its grasp.

2.7 Field-testing

The first field test of the bellows and boa-type actuators was a pilot study in the Gulf of Eilat, in the northern Red Sea, in 2015. To our knowledge, these field trials were the first time soft robotic grippers were employed for deep sea marine biology collection and manipulation. With the bellows-type gripper, we retrieved a red soft coral (*Dendronephthya* sp.) after landing the ROV on the sea floor. The four bellows-type actuators gently closed around the specimen without damaging any of the branches. The boa-type gripper proved very effective at wrapping around long and narrow (less than 12 mm diameter) coral whips that extended vertically from the sea floor. In the pilot study, the soft gripper was deployed in over a dozen dives at depths ranging from 100 m to 170 m and successive generations of the gripper have also been demonstrated at various locations in the Pacific and Atlantic Oceans at depths exceeding 3.5 km. Samples collected by the crew of the Nautilus and Ocean Exploration Trust using our soft grippers now reside in the collection of the Comparative Zoology Museum at Harvard University. The grippers have also contributed to the permitted biological sampling of deep-sea coral performed by the crew of the Nautilus. Fragments of the coral were distributed to various marine biology labs for genomics study in collaboration with the Ocean exploration trust. In accordance with permitting restrictions, all other animals the grippers have picked up are non-protected species. Furthermore, unless there was a need for a sample as decided by the research directive of marine biology

teams associated with these missions, gripper testing focused on the demonstration of gentle grasps and returning the specimen safely to the sea floor. Examples of these grasps are shown in Figure 2.19.

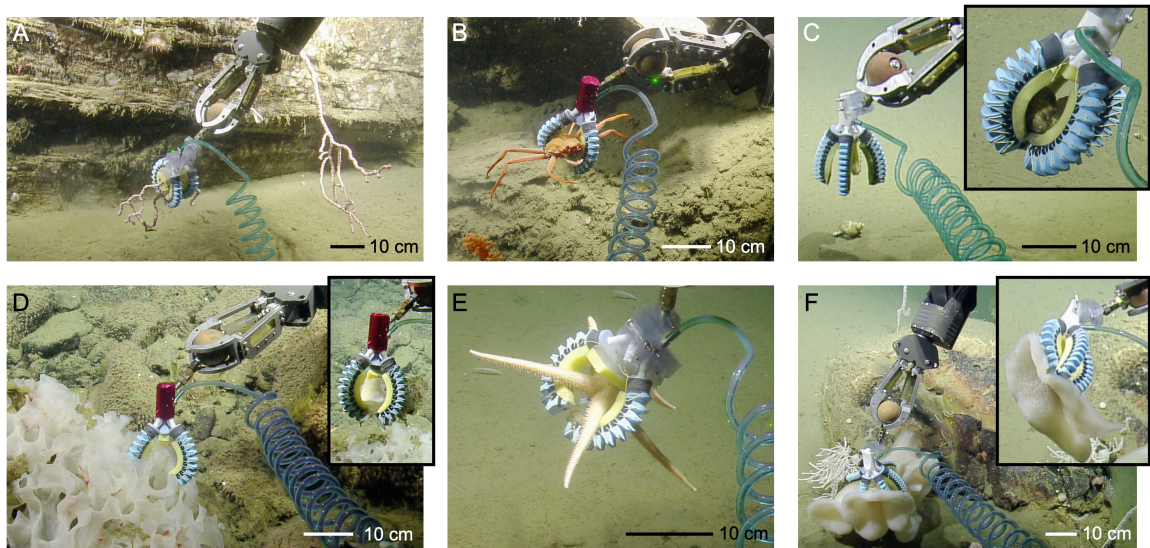


Figure 2.19: Photos of various specimens picked up in the Cordell Bank marine sanctuary. (A) A soft coral sample (*Paragorgia*) retrieved at 952 m with a three-finger cylindrical gripper, after being dropped during an attempted grasp with rigid manipulators. (B) A crab grasped and then released with a three-finger spherical gripper at a depth of 1205 m. (C) A snail grasped and released with a four-finger spherical gripper at a depth of 1287 m. (D) A sponge collected with a three-finger spherical gripper at a depth of 1700 m. (E) A sea star grasped and released with a three-finger cylindrical gripper at a depth of 1050 m. (F) A sponge collected with a five-finger spherical gripper at a depth of 2647 m.

In the effort of creating soft robotic grippers suitable for the task of deep-sea biological sampling, I have demonstrated soft robotic grippers that are capable of grasps that are gentle, conformal, and robust. Through the use of novel designs, design tools, and refinement of fabrication methods, I have developed a new generation of bellows actuator that can accommodate a larger range of bending curvatures, is stronger than its predecessors, and has a higher burst pressure and cycle life than its predecessors.

For more details on the locations of testing, pumps and engines used to provide hydraulic control, and the user interface, please refer to the publications included in the bibliography [19, 54, 55, 56, 57, 58].

Chapter 3

Active Modulation of Surface Contact

3.1 Introduction

Contact interfaces are an important consideration in how robots interact with the world. Enhanced adhesion or friction at a contact interface can contribute to a more secure grip on a given target, or to more traction for walking and climbing. The ability to actively adjust a contact interface, however, allows additional control over the ways in which robots interact with their environments. A gripper, for example, can use the modulation of contact friction as a way to enhance dexterous manipulation. For grasping, control over the friction of a gripper could enable using a low friction state to ease optimal positioning of the gripper on a target, as well as selectively increasing friction for grasping and manipulation tasks. It can be useful to decouple closure and normal contact forces of a soft gripper from the ability to apply traction. I demonstrate this by carrying and screwing in a light bulb with a soft gripper equipped with tunable friction at its finger tips. I also implement this in a simple, one degree-of-freedom crawler. In both of these cases, adding a tunable friction mechanism can reduce the complexity of the control or add additional control opportunities.

In this chapter, I describe a fully soft friction tuning mechanism made of selectively constrained elastomeric membranes that may be actively or passively applied to robotic grippers and crawlers. My mechanism utilizes fluidic power input that could be part of an existing drive (passive) or controlled by an additional input (active). The friction tuning

mechanism is evaluated independently as well as integrated in a gripper and crawler.

3.2 Background and prior art

Electro-adhesion, suction, folding mechanisms, and rigid toggles are some mechanisms used for actively tuning contact mechanics [47, 59, 60, 61]. Contact friction is a central consideration in almost any robotic system, especially those involved in locomotion or grasping. A number of studies have used artificial microstructures similar to those of gecko setae to enhance friction in applications ranging from endoscopy to climbing robots [62, 63, 64, 65]. Others have examined fabrication techniques to make devices that enable directional friction [66]. While these techniques have demonstrated increased friction (and, in some cases, adhesion), the resulting systems are inherently passive. The addition of active friction control has the potential to further enhance the performance of these systems.

Prior to the original publication of the soft mechanism described in this chapter, there have been relatively few studies regarding controllable friction in soft systems. Kim et al. have exploited shape memory polymers to achieve thermally controllable adhesion with actuation cycle times on the order of 100 seconds [67]. Lin et al. discuss a real-time mechanically tunable adhesive, though integration of this adhesive may be challenging in a fully soft system [68]. A self-assembling polymer network that creates a coating that modulates texture under UV light was described by Liu et al. [69]. Vikas et al., building on the work of Umedachi et al., have succeeded in creating soft crawling robots that leverage variable friction [70, 71]; their friction tuning mechanism is intimately coupled to the overall structure of the robot, enabling simple actuation though limiting the design space. With regards to locomotion, being able to modulate the friction acting on a leg or foot could enable a single degree-of-freedom system to move forward by creating asymmetric surface traction [72].

It is common practice to apply textures and materials to the surface of grippers to passively modify their contact mechanics. The benefit of this is generally common knowledge but some of the subtleties of strategically compliant contacts have recently been described for the purpose of robotic grasping and manipulation [73, 59, 74, 47]. Incorporating suction on the fingertips of a underactuated gripper is a form of friction modulation that can increase the normal forces between a gripper and contact surface without increasing the forces applied by the digit of the gripper [31, 60]. More recent publications have also introduced active

friction tuning elements for rigid robotic grippers [61, 75], as well as friction reduction for soft grippers [76].

In contrast to the work mentioned above, this chapter described a fully soft active friction tuning mechanism. The proposed mechanism relies on local pneumatic actuation with positive-pressure. This approach may have roots in biology, as geckos have been hypothesized to modulate pressure in their vasculature to aid in attachment to and release from substrates [77]. The mechanism described in this chapter can be incorporated into a soft system in either a fully integrated or modular fashion. Directly integrating into the existing actuation and control systems of a pneumatic or hydraulic soft robot provides enhanced function with little to no additional complexity to the existing system. Alternatively, when independent articulation is necessary, modularity can also enable separate adhesion control and actuation.

3.3 Soft mechanism for active friction modulation

3.3.1 Principle of operation

The fully soft, friction-tuning mechanism consists of two main elements: an inflatable membrane and a restraining layer. The inflatable membrane is an elastomeric material that exhibits high friction, while the restraining layer is a relatively inextensible, low-friction material that features periodic holes. Before inflation, the restraining layer is in contact with a substrate of interest. When the membrane is inflated, it pushes through the holes in the restraining layer such that the elastomer contacts the substrate, thus enhancing friction. Schematics and photographs illustrating this mechanism can be seen in Figure 3.1.

3.3.2 Model

A theoretical analysis using the Kirchhoff-Love theory for thin plates assisted in the choice of design parameters for the tunable friction mechanism. Because not all of the assumptions of this theory hold for large elastomeric deformations, the model was used to guide design rather than to precisely predict performance. The elastomer was modeled as a circular plate subject to a uniform pressure with a zero displacement boundary condition along the edge. With the assumption of an isotropic material, the governing equation

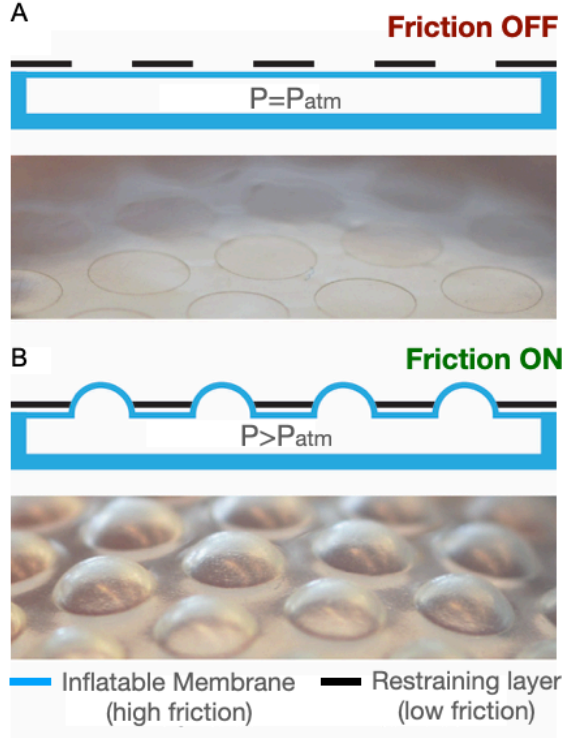


Figure 3.1: (a) Before inflation, the membrane does not protrude beyond the thickness of the restraining layer, so the substrate only touches the low-friction restraining layer. (b) Upon inflation, the membrane pushes through the holes in the restraining layer, increasing the effective friction.

simplifies to:

$$\nabla^2 \nabla^2 h = -\frac{P}{C} \quad (3.1)$$

$$\text{where } C = \frac{2Et^3}{3(1-\nu^2)} \quad (3.2)$$

Here h is the maximum vertical deflection, P is the applied pressure, ν is the Poisson's ratio of the elastomer, E is the Young's modulus of the elastomer, and t is the elastomer thickness. Solving the above for h , we obtain:

$$h = \frac{3Pa^4(1-\nu^2)}{32Et^3} \quad (3.3)$$

where a is the radius of the hole in the restraining layer.

Equations (3.1) – (3.3) provide an analytic expression for the relationship between pressure, hole size, membrane thickness, and maximum deformation. This model does not account for deformation of the restraining layer that occurs at high inflation pressures, nor the deformation of the elastomer upon contact with an object. Nevertheless, the equations indicate feasible combinations of geometries and actuation pressures for the mechanism and prove useful in guiding design parameters.

3.3.3 Geometry and materials

Preliminary testing with a number of different materials led us to use polydimethylsiloxane (PDMS) for the membrane material (Sylgard 184, Dow Corning). Regardless of the fabrication technique (in this work we used both molding and spin coating), all membranes were fabricated to be 200 μm thick.

The restraining layer was fabricated from a 75 μm thick polyester film (Duralar, Grafix Arts). We chose this material for its inextensibility, low-friction, and ease of machinability. This particular thickness was chosen to ensure minimal plastic deformation upon actuation. We laser-cut the film with a hexagonal array of circular holes that were 3 mm in diameter spaced 4 mm apart (center-to-center). The size and spacing of the holes in the restraining layer were chosen in conjunction with the thickness and material of the inflatable membrane to enable actuation at a low pressure. As described by equation (3.3), a thinner (thicker) membrane could be used with smaller (larger) holes to achieve a similar actuation pressure. Two laser cutters were used for fabrication: a diode-pumped solid state (DPSS) laser (E-355, Oxford Lasers Ltd.), and a CO₂ laser (VLS 6.60, Versa Laser). The DPSS laser minimized reflow and charring when cutting the polyester film. The CO₂ laser was otherwise able to cut larger areas and cut faster than the DPSS laser. The CO₂ laser also worked well in cutting the rip-stop nylon fabric used to create the bridging material described in the previous chapter. This bridging material was reused to incorporate the friction tuning mechanism into the gripper discussed in Section 3.5.1.

From equation (3.3) in the preceding section, the calculated actuation pressure required for the membrane to extend up to the thickness of the restraining layer is approximately 0.7 kPa. To extend one millimeter beyond the restraining layer, an actuation pressure of approximately 9.7 kPa is required. For a point of comparison, a typical soft bending actuator operates at 69 kPa [19].

3.4 Characterization of friction modulation mechanism

The soft friction modulation mechanism described above was evaluated first as an independent module and then as an integrated feature in the finger tips of a two-digit soft gripper. The purpose of characterizing the independent module was to have a performance metric that is not influenced by the shape, configuration, or application of the mechanism. Characterization of the effect of a mechanism integrated into a soft gripper is less readily abstracted, but offers a useful benchmark of how an instantiation of the mechanism might affect performance in grasping tasks as well as providing strategies for its integration into soft systems.

3.4.1 Module for isolated mechanism testing

We characterized the tunable friction mechanism performance on a universal testing machine (Instron 5544, Instron) to measure friction forces with varying preload forces, substrate materials, and inflation pressures. To facilitate characterization and mounting to the Instron, we made a standalone friction tuning device coupled to a rigid fixture. The friction tuning device consisted of an inflatable elastomer bladder with one (200 μm thick) side in contact with a polyester restraining layer. The bladder was cast as a single piece of PDMS using a mold made from a stack of laser-cut acrylic plates and 200 μm stainless steel shim stock to precisely control the membrane thickness. The restraining layer and bladder were mounted in a rigid acrylic fixture and clamped together with four bolts. A pneumatic line was plumbed into an inflation port in the side of the elastomer bladder to provide pressure. A schematic and photograph of the friction device can be seen in Figure 3.2. The device assembly served as a modular test device to facilitate swapping components and varying inputs in the experiments described below.

3.4.2 Testing setup

The friction tuning device was incorporated into a custom Instron fixture designed to enable measurement of horizontal friction forces. This lateral pulling configuration was used in place of the typical vertical setup to minimize off-axis loads applied to the load cell of the Instron and to simplify testing procedures. The Instron fixture used for the testing is illustrated in Figure 3.3. A pneumatic cylinder mounted to the Instron fixture allowed measurements to be made under a variety of preload forces. Because the friction tuning

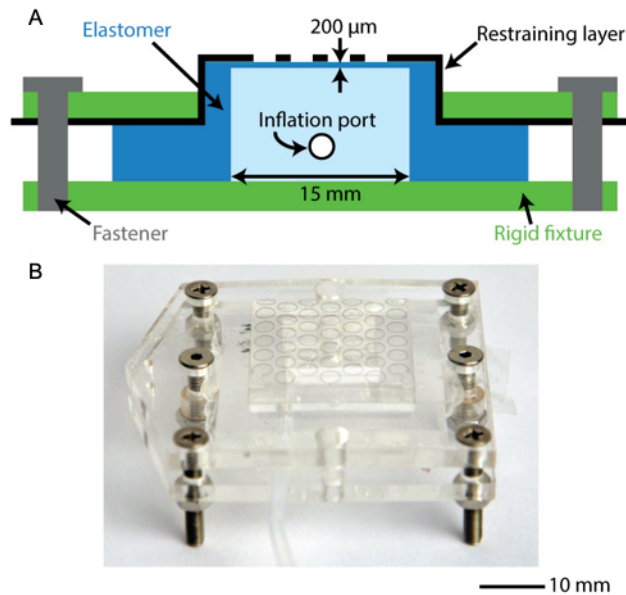


Figure 3.2: A (a) schematic and (b) photograph of the standalone friction tuning device. Note that the device is oriented upside-down in the photograph to better show the friction tuning features and the schematic is oriented to match the photograph. The restraining layer and elastomeric membrane were oriented downward for testing.

device remained stationary, the substrate of interest was fixed to a mobile sled. The top of the mobile sled was in contact with the inflatable membrane, and its bottom was coated with Teflon. To minimize the influence of frictional forces from sources other than the inflatable membrane on the substrate of interest, the mounting plate for the Instron fixture was also coated in Teflon, providing a Teflon-Teflon interface between the mobile sled and the Instron fixture mounting plate. The mobile sled was attached to a 0.64 mm diameter Kevlar string that, through a pulley, connected to the moving stage of the Instron. As the Instron stage moved, the load cell measured the force required to counteract the friction applied by our friction tuning device.

The effects of three variables (preload force, substrate material, and inflation pressure) on the performance of our friction tuning device were measured on the Instron. Preload forces were applied to the friction device via the pneumatic cylinder, which was controlled with a regulated pressure supply. We calculated the preload force as the pressure applied to pneumatic cylinder multiplied by the cylinder bore.

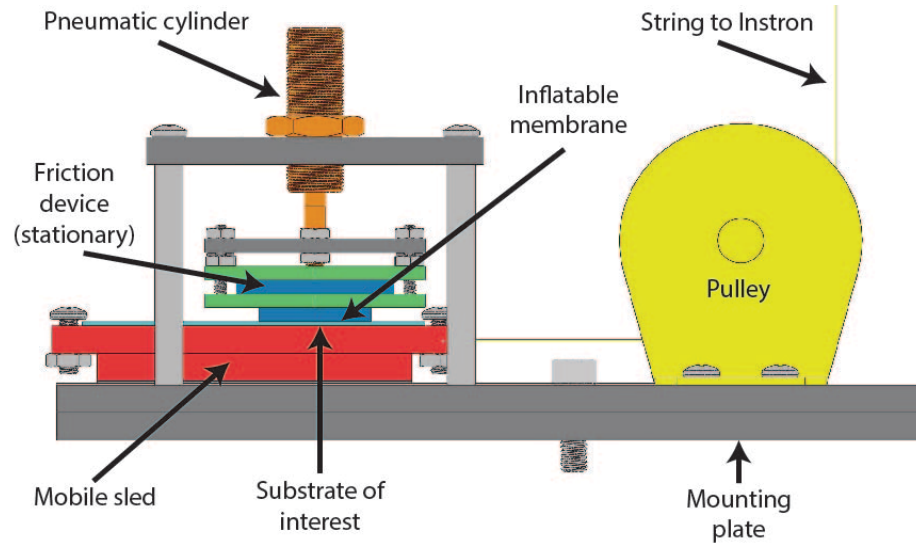


Figure 3.3: A schematic of the Instron fixture setup used to measure horizontal friction forces. The friction tuning device (with the inflatable membrane) remains stationary and is pressed downwards into the mobile sled via a pneumatic cylinder. The mobile sled, which carries the substrate of interest, is pulled by the Instron through a pulley.

3.4.3 Effect of preload force

In the first series of tests, we applied a constant preload force to the friction device and performed a ramping lateral pull force test (10 N/min) with the Instron. Each of these tests was performed on a glass substrate. We then determined the pull force at which the device began to slip. This test was conducted at three preload forces (2.46, 4.91, and 7.37 N), as well as four inflation pressures (0, 13.79, 27.58, and 41.37 kPa).

The resulting friction forces shown in Figure 3.4 suggest that the effect of preload force is minimal compared to other effects (see following sections). The preload force does, however, influence the efficacy of increasing the inflation pressure.

3.4.4 Effect of substrate material

In a second series of tests, again using a ramping force profile (10 N/min), we maintained a single preload force (4.91 N) but varied the substrate material and inflation pressure. This second set of tests compared the effect of glass, Teflon, and stainless steel substrates.

The effect of varying substrate material for a given preload force and varying

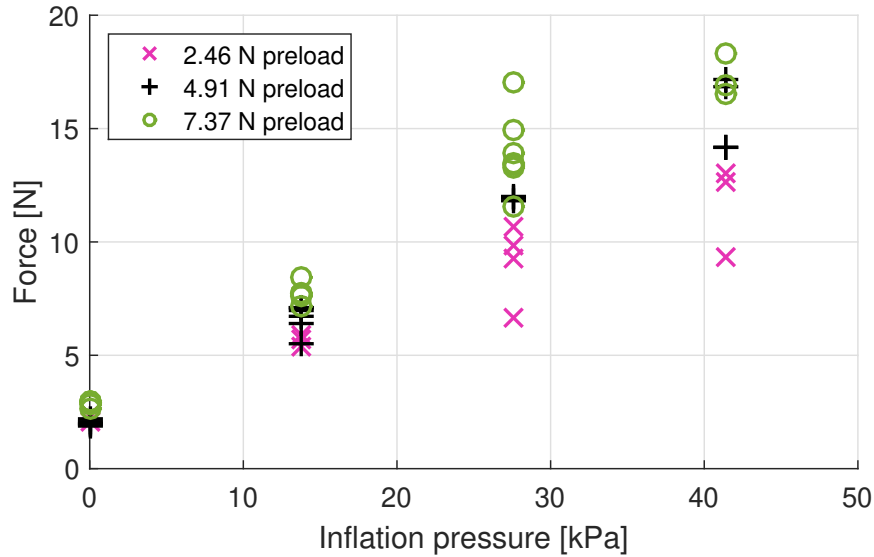


Figure 3.4: Graph of friction force data as a function of inflation pressure for different preloads, as measured on the Instron. These tests were performed on a glass substrate. Note that, for all conditions, each inflation pressure was tested at least three times.

inflation pressures is shown in Figure 3.5. As expected, the friction tuning device exerts lower frictional forces when applied to slippery surfaces such as Teflon. Higher-order effects that do not scale with inflation pressure, such as tribological variables or adhesion forces (e.g. van der Waals, bulk electrostatic, or capillary), may also be present; these effects could be an interesting area of future study. However, for all substrates, we do see that there is a significant increase in friction with any nonzero inflation pressure.

3.4.5 Effect of inflation pressure

We conducted a final set of tests to explore the differential in kinetic friction forces between the unactuated and actuated states of the friction tuning device. With the Instron programmed to move with a constant rate of extension (10 mm/min), we allowed the device to slide on a glass substrate in its unactuated state. After a short delay, we exerted a step input to the inflation pressure up to various values (13.79, 27.58, and 41.37 kPa). We recorded the average value for the force measured by the load cell before and after the step input (corresponding, respectively, to the unactuated and actuated states as recorded in Table 3.1). This test was also repeated at different preload forces (2.46, 4.91, and 7.37 N).

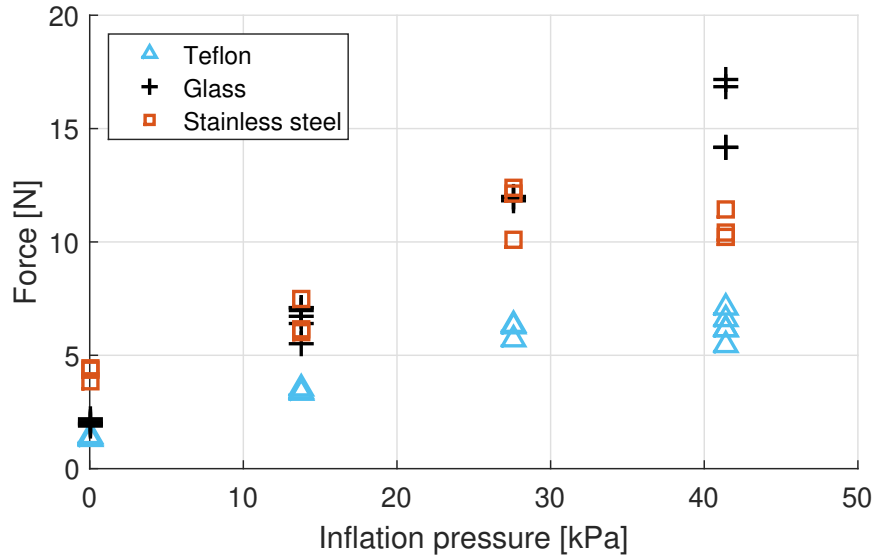


Figure 3.5: Graph of friction force data as a function of inflation pressure for different substrates, as measured on the Instron. These tests were performed with a constant preload force of 4.91 N. Note that, for all conditions, each inflation pressure was tested at least three times.

As alluded to above, the inflation pressure has a much more substantial effect than preload force on the measured friction forces. The increase in friction force measured between our unactuated and actuated friction device on glass exceeds an order of magnitude in some conditions, as shown in Table 3.1. Note that the data reported allow one to see the effects from variation in preload force with constant inflation pressure as well as the effects from variation in inflation pressure with constant preload force. The stronger dependence on inflation pressure is attractive for applications like crawling or grasping, where it may be advantageous for friction forces to be relatively insensitive to crawler weight or grasping force, and more sensitive to a controllable variable such as internal pressure.

In addition to considering frictional force, we can examine the effect of preload force and inflation pressure on the coefficient of friction (see Table 3.1). The coefficients of friction are simply the frictional forces divided by the preload forces. From this perspective, the data show that higher coefficients of friction are achieved at lower preload forces, which is beneficial for soft robotics given the typically low forces involved. This also makes intuitive sense as a high preload force will tend to compress the high friction membrane to the point where contact is then distributed between the high friction membrane and the low friction

restraining layer.

Table 3.1: Results of kinetic friction differential testing

Preload Force [N]	Inflation Pressure [kPa]	Unactuated		Actuated	
		Force [N]	CoF* [-]	Force [N]	CoF* [-]
2.46	27.58	1.14	0.46	12.15	4.94
2.46	27.58	1.27	0.52	12.50	5.08
2.46	27.58	1.43	0.58	12.82	5.21
4.91	13.79	2.16	0.44	7.26	1.48
4.91	13.79	2.01	0.41	7.78	1.58
4.91	13.79	2.77	0.56	8.57	1.74
4.91	27.58	2.66	0.54	13.46	2.74
4.91	27.58	2.82	0.58	14.49	2.95
4.91	27.58	2.25	0.46	14.69	2.99
4.91	41.37	1.77	0.36	18.88	3.85
4.91	41.37	1.73	0.35	20.04	4.08
4.91	41.37	1.80	0.37	19.35	3.94
7.37	27.58	2.68	0.36	15.94	2.16
7.37	27.58	3.31	0.45	16.54	2.24
7.37	27.58	3.38	0.46	17.05	2.31

This table details the change in the kinetic friction force (for a given preload force and inflation pressure) that occurs as the friction device is actuated on a glass substrate. The data are available to compare across inflation pressures for a given preload force as well as across preload forces for a given inflation pressure. One can see a much stronger dependence on inflation pressure than preload force. *CoF denotes the coefficient of friction.

3.5 Soft robot integration

3.5.1 Integration with a soft gripper

To demonstrate the application of friction modulation in soft robotic grasping, we created a soft robotic gripper that has the ability to modulate the friction of its fingers, which can be seen in Fig. 3.6. Each finger of the gripper is a pneumatic bending actuator with a tunable friction pad attached to its fingertip. The friction pads are made of two layers

of PDMS bonded together with oxygen plasma treatment. For a restraining layer, we used thermoplastic polyurethane (TPU) coated taffeta (heat sealable taffeta, Seattle Fabrics). We deviated from our typical restraining layer choice of polyester in this demonstration to take advantage of certain properties of the taffeta that aid in integration with the soft bending actuator; used as the bridging material described in the previous chapter, the TPU coated taffeta resists tearing under the tension of the actuator lacing and accommodates the flexing and bending of the underlying actuator. The taffeta also cuts well in the CO₂ laser. In addition to serving as the restraining layer for the inflatable membrane, the taffeta also mechanically secures the friction pads to the bending actuators and helps reinforce the body of the actuator via the lacing technique explained in Section 2.5.2.

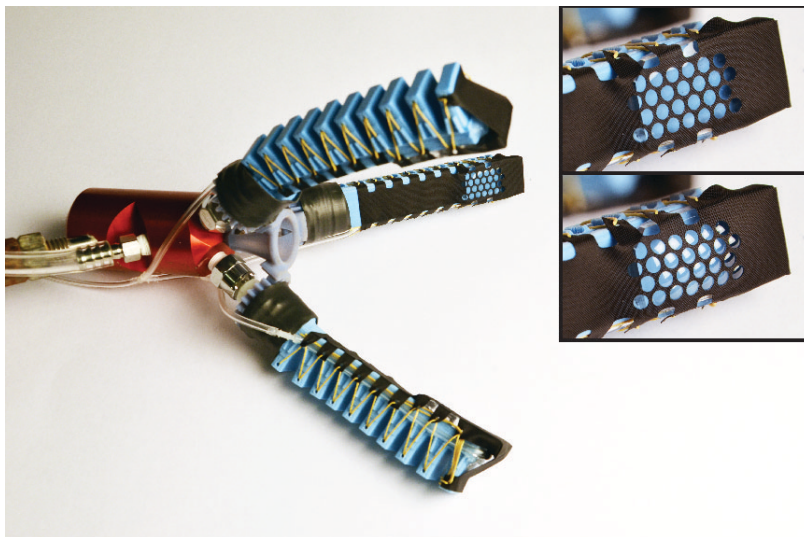


Figure 3.6: The gripper consists of pneumatic bending actuators that have been modified with friction pads at the fingertips. The friction pads are made of two layers of PDMS plasma bonded together. The taffeta anchors the friction pad to the bending actuator and serves as a restraining layer for the inflatable membrane. The two inset pictures show the friction pads unactuated (top) and actuated (bottom).

In this demonstration, the friction pads are actuated independently from the main bending actuators. That is, this gripper is a multiple degree-of-freedom system with independent control over finger actuation and friction modulation. The friction pads actuate at approximately 7 kPa, whereas the fingers are fully actuated at approximately 55 kPa. If found to be advantageous, the system could be redesigned with only minimal effort to directly couple the actuation of the fingers and the friction pads. As seen previously, the

actuation pressure of the friction pads has a strong dependence on both membrane thickness and restraining layer hole size, so altering these parameters is a simple way to modulate actuation pressure of the friction pads. In this way, the bending actuators and friction tuning elements that comprise the gripper could be actuated by a single pneumatic input. The friction tuning elements could then be adjusted to engage at a predefined pressure threshold that corresponds to a desired curvature of the bending actuators. Similarly, as discussed in the previous chapter, the calibration of curvature versus operating pressure of the bending actuator can be independently adjusted.

To evaluate the tunable friction performance of the soft gripper, we measured the force required to remove a plastic cylinder from its grasp with both actuated and unactuated friction pads. With the Instron programmed to move at a constant rate (50 mm/min), the grasp forces were measured for three cylinder diameters (25.4, 50.8, and 76.2 mm). The bending actuators were pressurized to 75.8 kPa and the friction pads were pressurized to 17.2 kPa for each of the tests. A picture of the test setup is shown in Figure 3.7 and it is worth noting that the off-set two finger setup shown provides an estimate of the retaining force that could be achieved from two bellows actuators, but this would likely not create a stable grasp in a less constrained setup. The fingers would be better arranged in line with one-another or in an arrangement of three digits in a cylindrical grasp or a spherical grasp arrangement as shown in Figure 3.6.

The resulting force-extension data from the cylinder grasp tests are shown in Figure 3.8. The plot shows the average values from the testing, as well as one standard deviation above and below the average values. As expected, the peak forces recorded as the cylinder slips through the actuated friction pads (represented by the solid lines) are much higher than those from the cylinder slipping through the same pair of pneumatic bending actuators with unactuated friction pads (represented as dashed lines).

Using the gripper setup shown in Figure 3.6, we successfully positioned a light bulb into a mating socket. Frames from a video of this process can be seen in Figure 3.9. The internal pressure of the bending actuators was held at approximately 50 kPa for the duration of the task. By switching between actuated and unactuated friction states, the gripper slid over the surface of the bulb to adjust its gripping position while still cradling and preventing the light bulb from falling. In Figure 3.9A, the bulb is carried to the socket and the gripper starts to install it with a quarter turn. At this point, the bulb would fall if the gripper were removed but the digits of the gripper continue to apply a light, stabilizing

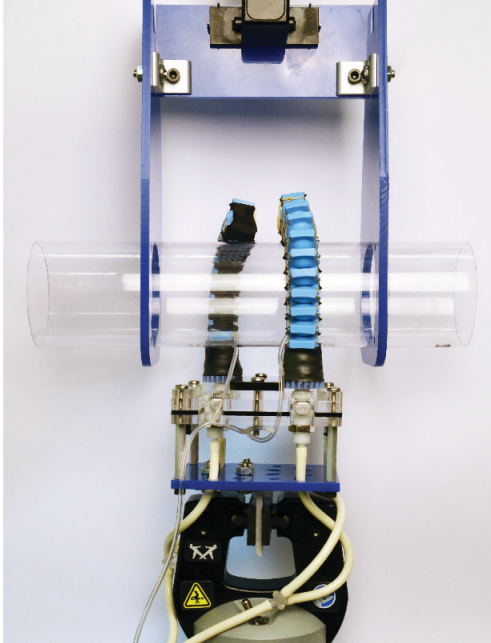


Figure 3.7: Instron test setup used to measure the force required to pull cylinders of various diameters. The two bending actuators feature friction pads on their fingertips, which were tested in both actuated and unactuated states.

force as the friction pads are turned off to allow the gripper to pivot over the surface of the bulb. Figure 3.9B shows six sequential frames where, in the first three frames, the gripper applies both a stabilizing force as well as traction from the friction finger pads to screw the bulb in clockwise. In the second three frames, the friction pads are disengaged to allow the gripper to slide counterclockwise over the bulb's surface. An 'x' drawn on the surface of the bulb helps to visualize this movement. Finally, in Figure 3.9C, the gripper finishes installing the bulb with the friction pads activated and then the pads are deactivated so that the gripper can pull away from the bulb.

3.5.2 Integration with a crawling robot

To evaluate a second use case, we incorporated our tunable friction mechanism into a crawling robot, which can be seen in Figure 3.10. The robot consists of a minimal body and two legs. Each leg is a pneumatic bending actuator, (similar to the ones used in other soft robotic applications [19]), that has been modified to accommodate tunable friction pads. The friction pads rely on the same mechanism as above, consisting of a

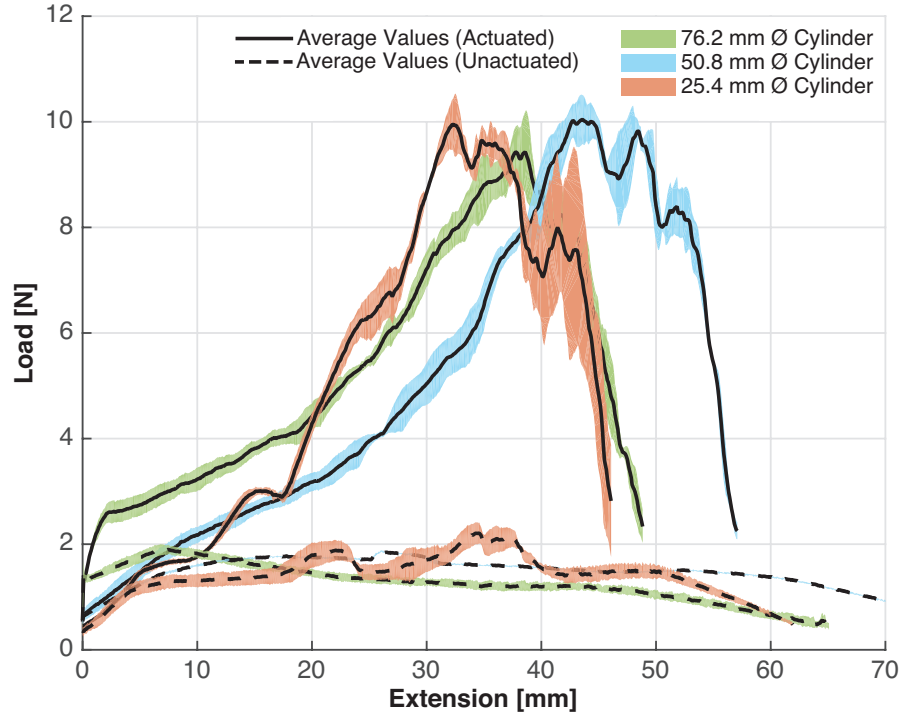


Figure 3.8: Forces required to pull cylinders of varying sizes from between two bending actuators with actuated (solid lines) and unactuated (dashed lines) friction pads. The shaded regions show one standard deviation above and below the average values ($n = 5$). In all tests, the bending actuators and friction pads were pressurized to 75.8 kPa and 17.2 kPa, respectively.

polyester restraining layer and an inflatable PDMS membrane. A second polyester sheet serves as a backing to the membrane, completing the inflatable structure. We sealed the membrane to the polyester backing with a silicone adhesive (Loctite Superflex Clear RTV, Henkel Corp.), and then sewed the edges with cotton thread for reinforcement. If stronger adhesion between these layers is required, success has been found by using silane treatment and oxygen plasma to bond PDMS to plastics [78, 79]. The friction pads were mechanically attached to the sides of the legs with an air port protruding into the internal cavity of the leg, thereby creating a direct pneumatic coupling and resulting in a single degree-of-freedom system.

Upon inflation, the friction pads actuate first (at approximately 7 kPa), providing a pivot point for each leg. Upon increasing the pressure, the legs begin to bend (at ap-

proximately 35 kPa), pushing the robot forward. When quickly vented, the friction pads and legs deflate simultaneously, allowing the elastomeric membrane of the friction pads to retract as the legs return to their initial, unactuated state. Without the high friction pivot points at the distal ends, the legs sweep back to their unactuated state without pushing the robot body backwards.

The crawling robot was tested on a glass substrate (Fig. 3.10). With an actuation frequency of 0.5 Hz, the crawler was able to propel itself forward at a speed of 0.2 body lengths per second (12 mm/s). To confirm the utility of our friction pads, we tried operating the crawling robot with small polyester sheets under the friction pads, effectively neutralizing our tuning mechanism. Additionally, we attempted crawling with legs made from unaltered bending actuators (i.e., without any friction pads). We found that, after numerous actuation cycles, neither modified robot was able to produce any net motion, proving the necessity of our tunable friction mechanism for locomotion in this configuration.

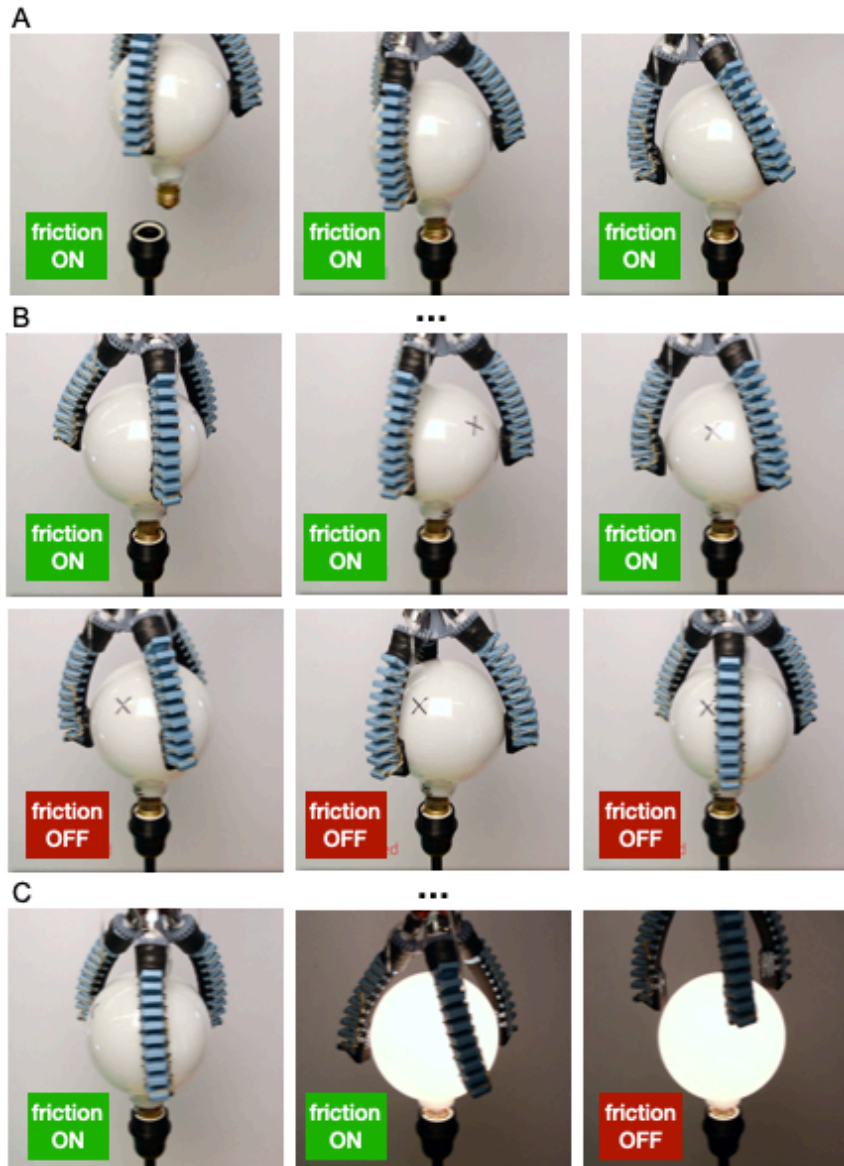


Figure 3.9: Example use case where the gripper with friction-tuning finger pads is used to screw in a light bulb. The gripper digits are pressurized during the entirety of the demonstrated to provide a light normal force and the friction pads are turned on and off as indicated. Three sets of frames show (A) the initial delivery and insertion of the light bulb, (B) screwing the lightbulb in further, and (C) securing the light bulb to the point of turning the bulb on and then pulling the gripper away.

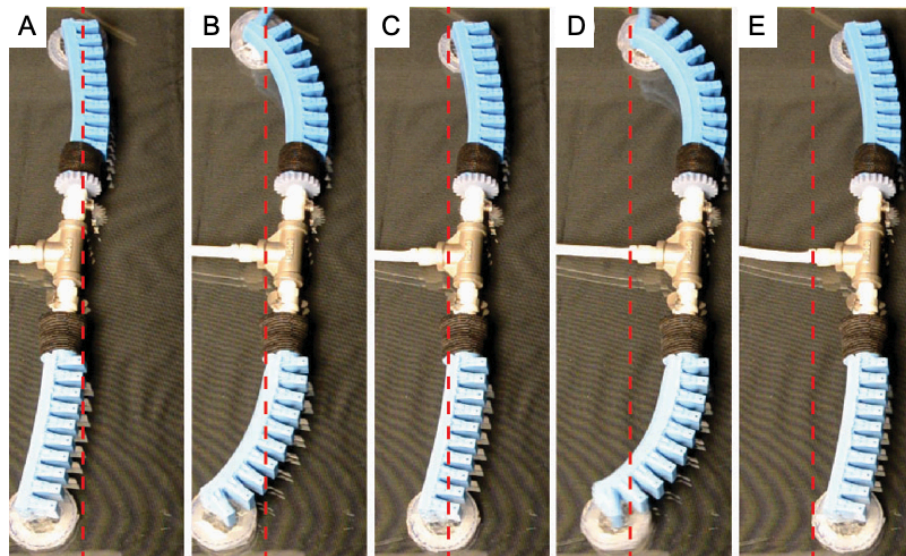


Figure 3.10: (A) The crawler in its initial state. Each leg consists of a bending actuator with a tunable friction pad at its distal end. (B) As the legs actuate during the power stroke, the friction pads engage, creating pivot points that allow the body of the robot to move forward. (C) As the legs are vented, the friction pads depressurize and the high-friction membrane retracts. With the low-friction restraining layer now in contact with the substrate, the friction pads slide forward with the legs in the return stroke, resulting in net forward motion. Frames (D) and (E) show another cycle. The dashed line serves as a position reference.

3.6 Conclusions and future work

Quantitative force testing shows that a tunable friction mechanism can modulate friction forces by over an order of magnitude between unactuated and actuated states. The mechanism described in this chapter can be used to actively modulate the surface contact of a soft system so as to augment its functionality. This augmented functionality is demonstrated in a gripper with the capacity to effectively turn friction on and off at its fingertips. This control over gripper friction allows for more dexterous manipulation of objects and a five times differential in grasping force. The augmented functionality is also demonstrated in a crawler that can produce forward motion with a single degree of freedom input. Furthermore, this mechanism demonstrates a broader concept of hierarchical functionality and structure built into a soft robot. The friction tuning structures are integrated with the grippers and can be independently controlled or directly coupled to the actuation of the underlying structure.

The instantiation of the friction tuning mechanism described above was achieved largely by integrating modularly fabricated soft components. Future work could focus on an approach of directly integrating these active surface structures into the body of the underlying actuators. Alternatively, a modular approach can make fabrication and repair simpler, and future work could instead focus on improving those methods for efficiency of production, reliability of performance, and a lower-profile to more easily incorporate similar mechanisms into a range of soft systems.

Also, while this work explores the use of active surface structure to modulate the contact interface, there is also much potential value to be achieved from the development of passive surface tuning structures. There is already a wealth of work in the soft robotics field on bio-inspired surface structures to achieve traits like enhanced adhesion [80], directional friction [81], and structural colors [82]. An area of interest going forward is the investigation of the infundibular surfaces of octopus and squid suckers where surface morphology can be brought to bear in passively tuning the contact interface of soft robotic devices.

Chapter 4

Distributed contact via soft arrays

4.1 Introduction

The compliant materials of soft robots demonstrate advantages over their rigid counterparts through passively adaptive mechanics, the ability to achieve complex motions with relatively few inputs, and the potential for safe human-robot interactions. This compliance also effectively limits the forces that an individual soft actuator can apply to its environment. Many actuators together, however, can create an array of distributed contacts that are individually gentle and collectively strong. Furthermore, high aspect ratio actuators are structurally compliant and can thus deform more than low aspect ratio actuators in ways to create greater engagement with target objects. Arrays of high aspect ratio soft actuators can be valuable in applications involving fluid manipulation, locomotion, grasping, and delicate object manipulation.

In this chapter, I describe new fabrication strategies to create high aspect ratio soft actuators individually as well as in integrated arrays. Fabrication of large arrays of high aspect ratios is challenging with the majority of techniques being used to create pneumatic and hydraulic soft actuators because it requires complex molds with high precision over large areas, or the need to join many soft components together. By developing a modified dip-coating process, I present an inexpensive, modular, and scalable method to build integrated soft actuator arrays, as shown in Figure 4.1. The molds are ‘open-faced’ and do not fully enclose all surfaces of the liquid elastomers. The exterior geometry of the actuators is instead defined by surface tension, gravity, and the viscosity of the mixed rubber, eliminating the need for tight tolerances between mold faces. Within this dip-molding approach, four

strategies are provided to mechanically program the motion of these actuators, including the use of fiber inclusions, gravity, surface tension, and electric fields.

These techniques were used to demonstrate the fabrication of soft actuators with aspect ratios up to 200:1 and integrated arrays of up to 256 actuators. Furthermore, these methods have the potential to achieve higher aspect ratios and larger array sizes. Operating pressure, curvature, and curling strength tests reveal the design space in which we can select fabrication parameters. This flexibility in fabrication parameters allows us to tune the input and output parameters of soft bending actuators. Integration with a fluidic demultiplexer demonstrates compatibility of dip-molded actuators with microfluidic controllers, for which the ease of tuning input and output parameters is particularly useful. Minor modifications to the process also allowed for the fabrication of tri-chambered actuators with two-degrees of freedom, which were driven by the demultiplexer.

An individual, 30 mm long bending actuator made with these methods weighs between 0.15g and 0.5g, and can hold up to 2N. They can also be designed to work in groups to increase collective grasping and manipulation forces of an array while maintaining distributed and low-force contacts. Individual actuators can also be made longer to achieve greater engagement and wrapping around target objects than the short actuators. In the following chapter, these long filament-like actuators are integrated into a novel gripper that leverages the structural and material compliance of the high aspect ratio actuators in a new grasping strategy, referred to as entanglement grasping. In entanglement grasping, an array of these highly compliant actuators are stochastically applied in grasping and excel in picking up topologically complex target objects. We chose to use actuators that are approximately 300 mm long for the entanglement grasper but have fabricated actuators with lengths up to 1 m.

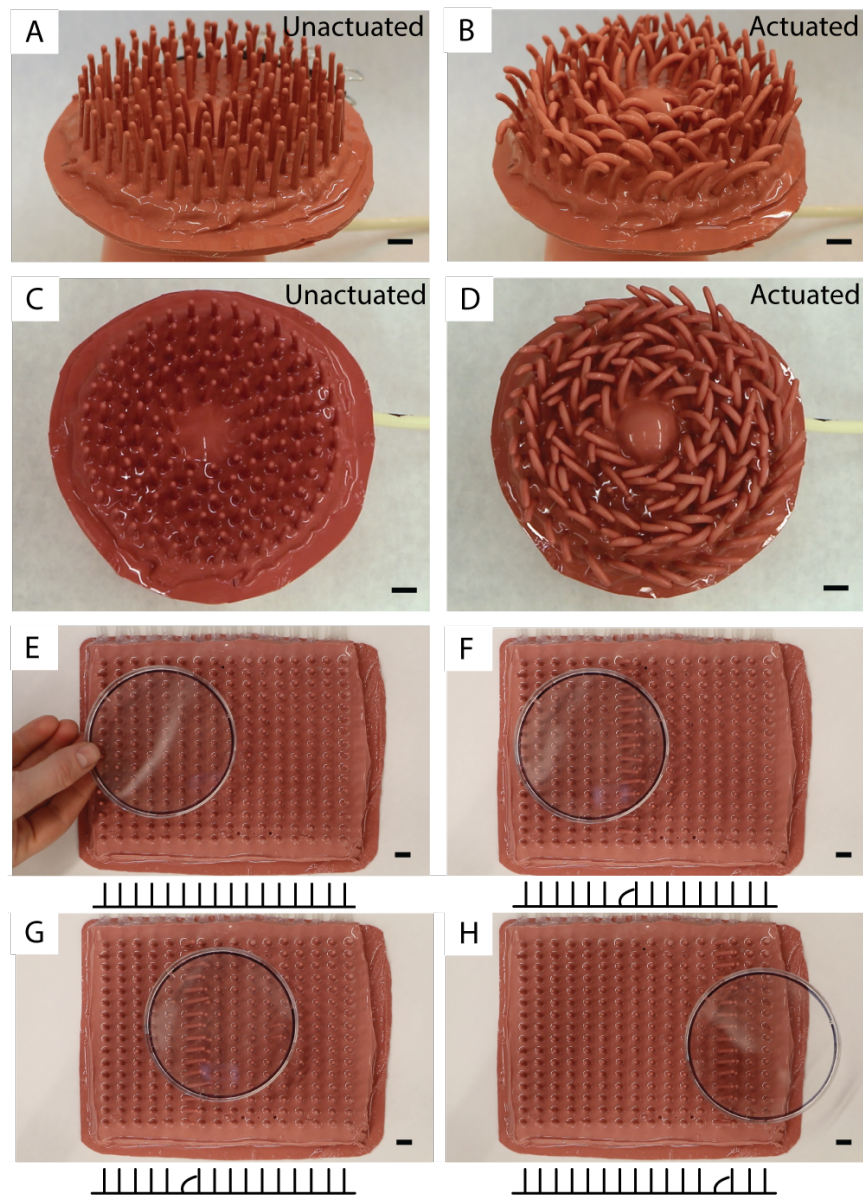


Figure 4.1: Examples of large arrays of structures made using open face molds. (A-D) A 149-part array, mechanically programmed to bend in alternating clockwise and counterclockwise rings defined by the placement of fibers on the pins of an open face mold. (E-H) A 256-part array of inflatable structures that are mechanically programmed to bend in the same direction using gravity augmented molding. Each column of 16 elements is controlled by a separate channel. Images (E-H) show frames from a video of a wave pattern moving through the actuator columns and pushing a petri dish. The pictures shown are from 0 s, 5 s, 15 s, and 104 s. The schematic below the images shows which column is being actuated. The scale bars in all images represent 1 cm.

4.2 Background and prior art

High aspect ratio actuator arrays can be leveraged in systems that emulate ciliary movement for the purpose of fluid mixing, fluid propulsion, general fluid manipulation, and low Reynolds number swimming. Test systems ranging from micron to millimeter scales have been fabricated by direct molding of actuators, casting into micro machined molds [83], casting into a deep-chemical etched silicon wafer molds [84], and casting into multi-part precision molds with the help of capillary action to create one [85] and two degree of freedom cilia arrays [86]. Passive arrays of branching structures have been formed with a three part mold for the purpose of passive locomotion [87] and similar methods could be used to create artificial ciliary systems. Larger arrays of smaller scale cilia structures have been demonstrated using a variety of alternative fabrication strategies including molding in a sacrificial filter that is later dissolved [88], self assembly of magnetic particles [89], magnetic manipulation of rubber with embedded magnetic particles [90], and roll touch molding [91]. Related work focused on ambulatory locomotion has also demonstrated the use of magnetic fields to form and later control large arrays of high aspect ratio structures from silicone filled with magnetic particles [90]. Most of the arrays mentioned above are either passive structures, indirectly actuated by deformations in supporting structures, or manipulated via changes in a local magnetic field. The arrays created by Gorissen et al. [85] and Milana et al. [86] however, are pneumatically actuated and the cilia are individually controllable.

Complementing fluid flow manipulation, a variety of high aspect ratio actuators have been made into tentacles and miniature grippers for delicate grasping and manipulation of small, discrete objects. Corrugated micro tentacles have been created by casting silicone rubber into a two part micro-machined mold [92] and also integrated into a three finger gripper [93]. Moving away from traditional molding, bulk silicon fabrication techniques were used to create a four-fingered micro-gripper driven with pneumatic Parylene film balloons [94]. Similarly, Parylene balloons have been used to create an array of bending actuators to emulate cilia capable of macro-scale object manipulation [95]. Researchers have also demonstrated casting PDMS into molds created with the use of MEMS fabrication techniques and stereo lithography to cast 2.5D components that are then bonded to construct microfingers [96] and microactuators for retinal surgery [97]. Arrays of similar actuators have then been integrated into a five-fingered micro-hand [98]. Microfingers have also been fabricated with

2.5D molding that has been augmented to incorporate nanofiber strain-limiting inclusions [99], similar to demonstrations of multi material actuators at larger scales [100, 101, 27]. As a novel alternative to molding, a micro-tentacle gripper has been fabricated by dip coating a horizontal rod, using gravity to bias the wall thickness in the rubber coating that was formed around the rod. Once cured, the rod coating is removed, sealed on one end, and used as a soft pneumatic bending actuator [102]. The fabrication methods presented in this paper are most closely related to this dip coating method and expand it further to larger arrays, longer actuators, and additional strategies to mechanically program bending motion into the actuators.

In the above examples, high aspect ratio actuators with diameters ranging from microns to a few millimeters have been used for fluid flow manipulation, locomotion, and miniature grippers. Individual high aspect ratio actuators have been demonstrated in the form of continuum arms, tentacles, and tendrils for grasping and manipulation [103, 56, 104, 105, 106]. Various other high aspect robots resembling worms and snakes have also been used to demonstrate locomotion [103]. The individual gripping actuator that most closely resembles the dimensions and curling behavior of the actuators presented in this paper was created by Must et al., and their tendril-like robot utilizes a novel reversible osmotic actuation that occurs on time scales of approximately one hour. Several macro-scale applications have made use of arrays of high aspect ratio actuators. McKibben actuators can be made very long with relative ease and Kurumaya et al. bundled a group of thin, high aspect ratio McKibben actuators to be used as artificial muscles, demonstrating an array working together in place of a single actuator. The array achieves a greater system compliance while maintaining comparable composite strength to more traditional individual McKibben actuators of larger diameter [107]. A different use of high aspect ratio features to incorporate compliance into a larger structure was explored by Zhou et al, who incorporated arrays of passive silicone pillars on the inner palm and finger surfaces of a soft robotic hand [108]. The effect of these pillars can be compared to the memory foam used by Galloway et al. to minimize the (already low) stress concentration induced by soft grippers [19]. Covering a soft robotic hand with macro-sized cilia can create a more gentle and robust grasp, where the compliant pillars conform to objects while offering lower resistance to shear deformations than memory foam [108]. By introducing fabrication strategies to enable high aspect ratios and large arrays of actuatable soft structures, we hope to contribute to this work of compliant structures that are able to provide distributed strength and manipulation

capacity. This could be in the form of enhanced object grasping and manipulation with an active array of short pillars to augment the grasping concepts proposed by Zhou, larger arrays of macro cilia for fluid and object propulsion, or systems for locomotion.

The molds introduced in this work consist of inexpensive and modular laser-cut acrylic parts and commercially available stainless steel pins. In place of machining high precision interlocking mold parts, the mold components are assembled into a structure that is dipped into liquid rubber or poured over with liquid rubber. These open face molds define the internal part of the final geometry and the remaining (outer) geometry is entirely dictated by gravity, surface tension, and viscosity. These open face molds can be used to create functional soft robotic actuators that are mechanically programmed to bend in the same uniform direction or to bend in an arbitrary predefined vector field of directions. As mentioned earlier, actuators made from a form of dip coating have also been demonstrated by Paek et al.[102] I extend these principles to achieve higher aspect ratio actuators as well as larger arrays of actuators. Through the use of modular open face mold forms, it is possible to rapidly and inexpensively make new molds, various sizes, and custom arrangements of soft actuators. We also introduce new strategies for mechanically programming the motion of these actuators, including modifications of familiar strategies such as fiber inclusions and gravity, as well as more novel strategies that make use of surface tension and electric fields. In this chapter, I focus on the fabrication of actuatable bending soft structures (soft actuators), but the same techniques can be used to create passive soft structures.

4.3 Open face molds and dip molding

The primary fabrication strategy presented in this work for the creation of high aspect ratios and large arrays of soft structures leverages the simplicity of open face molds, where a significant portion of the material being molded is not enclosed by a mold face. An example and schematic of how an open faced mold can be set up is shown in Figure 4.2. We are able to drastically reduce the complexity and tolerance requirements of the molds by relying on the balance of gravity, surface tension, and the rubber viscosity to determine the dimensions of the final structure, rather than requiring highly precise, fully enclosed, multi-part molds. This dip coating technique mimics those used in the fabrication of dipped candles, latex balloons, and doctors' gloves, where the thickness of the resulting structure is not controlled by a precise mold but the rheology of the liquid applied [109]. In the case

of some of the larger arrays, rubber is poured over the mold in place of dipping but the mold design and execution remains the same.

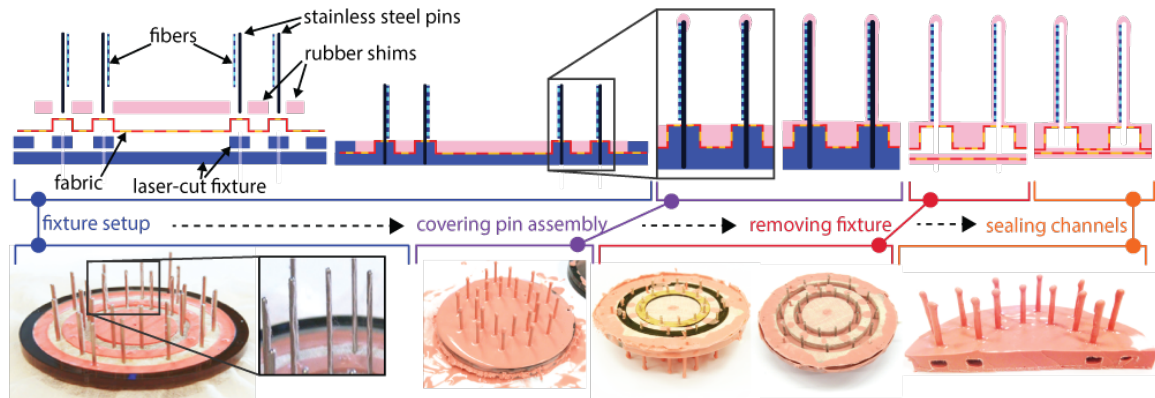


Figure 4.2: Overview of dip coating fabrication strategy including open face mold setup, dip coating results, mold removal, and sealing of pressure supply channels. Fibers are used for mechanical programming in this example and the resulting actuators bend toward the center of the assembly, in the direction of the fibers. The top row shows a schematic of the open faced mold assembly and dip coating with fiber inclusions, while the bottom row shows pictures of the dip coating process that correspond to the stages depicted in the schematics.

The basic form used for the open faced molds in this work consisted of arrays of stainless steel pins press-fit into laser-cut acrylic plates, strips, and rings. A laser-cuter and acrylic plates were chosen for convenience but the molds could be made via additive manufacturing, injection molding, milling, or even hand drilling in a variety of plastics or metals. In the work presented here, the use of laser-cut acrylic forms and commercially available pins allowed for easy creation of cut files and rapid, inexpensive construction of new molds. With standardized spacing, modular molds could be constructed with interchangeable parts for the purpose of reusing mold components as well as creating larger composite mold forms.

The general dip-coating process used to make an array of actuators similar to those shown in Figures 4.1 and 4.2 begins with assembling an open face mold. The mold form is assembled onto a laser-cut acrylic base plate that fixes the relative positioning between components. Acrylic rings or bars are then placed on top of the base plate as rails that define the open channels that will supply fluid flow to the actuators. Rubber shims are cast in the region between the rails. Once cured, the acrylic fixture and rubber shims are pulled apart and then reassembled with fabric woven between the components, as shown in Figure 4.2. The pins that will define the interior dimension of the actuator are then press

fit into holes going through the rails and base plate.

Before the first full dip coating of the open faced mold form, the tips of the pins are dipped into liquid rubber and allowed to cure upside-down so that rubber does not drip along the length of the pin. This prevents thin spots from forming on the pin tips and later creating holes in the actuators. After the tip coatings are cured, the pins are dipped into liquid rubber or, in the case of larger assemblies, poured over with liquid rubber, taking care to obtain full coverage of the pin surfaces. Once fully coated, the pin assembly is left at room temperature to cure with the pins pointing upward. The purpose of curing at room temperature is to allow ample time for the rubber to flow to a steady state and minimize variations in rubber thickness. After curing, another layer of rubber can be added to increase the overall actuator thickness. The thickness of an individual layer is determined by the balance of gravity, surface tension, and viscosity of the rubber used. Thinners and thickeners may be mixed into the uncured silicone rubbers to adjust this but may also affect the stiffness and tear strength of the cured rubber. The pins can also be preheated or placed into an oven after dipping to speed up the curing time, thereby increasing viscosity soon after dipping, resulting in thicker layers. In order to limit the variables tested in the initial exploration of this concept, we chose to only vary the number of layers to control the outer diameter of the actuators.

Once the desired number of layers are added, the acrylic fixture and pins comprising the open face mold are removed and the resulting rubber structure can be sealed by pouring a thin sheet of liquid rubber over a piece of fabric and lightly pressing the open pressure supply channels into the liquid rubber. The fabric that was previously pinned between the rubber shims and base plate helps to mechanically anchor the previously cured rubber structure with the liquid rubber. Further detail of this process and the role of this interwoven fabric layer can be found in section 4.7.

4.4 Four methods of mechanical programming

While the dip-coating and pour-over techniques mentioned above are the fundamental methods used to create the arrays of soft structures presented in this work, a secondary component of the fabrication process is necessary in the creation of bending actuators. The purpose of the second component, described below, is to introduce an intentional structural bias that causes the soft structures to bend and curl when internally

pressurized. This mechanical programming is accomplished with the use of fiber inclusions, gravity, surface tension, and electric fields to complement the forms created by the open face molds. A schematic of these modification methods is shown in Figure 4.3, as well as cross-sections of soft actuators that were created with each method. A brief explanation of the four modification methods follows, and further fabrication details can be found in Section 4.5.

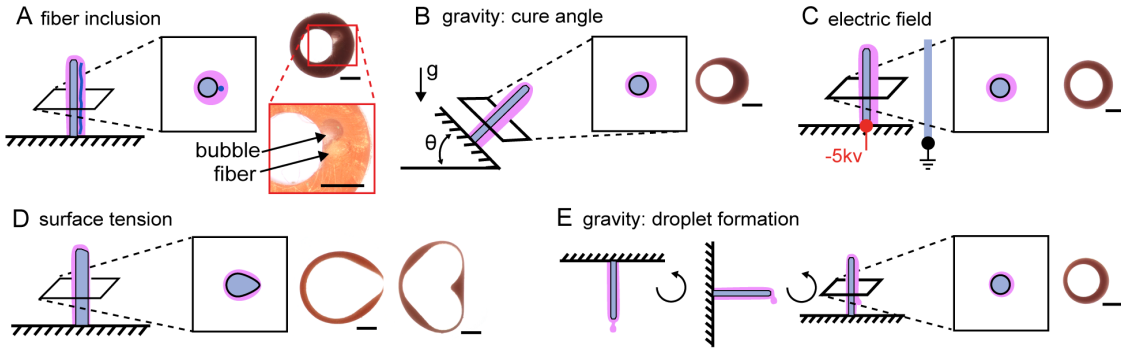


Figure 4.3: Schematics and cross-section examples of different methods of mechanical programming used with open face molds. The scale bars indicate 1 mm. The first cross-section shown in (D) is torn because the actuator ruptured in pressure testing prior to removing the cross section.

While exploring strategies for mechanically programming the soft actuators formed with open-faced molds, modeling of similar soft actuators presented by Gorissen et al. provided a guide of advantageous design characteristics for the cross-sectional geometry. From their model, it is expected that bending actuators with larger internal diameters and high eccentricity will achieve the highest bending curvature for minimal stress in the material. The eccentricity is defined as the offset between the center point of the internal void and the center of the external shape. This is, of course, inherently limited by the fact that the internal diameter and eccentricity of the structure should not create non-zero wall-thicknesses. Furthermore, wall thicknesses nearing zero pose higher fabrication challenges [110]. Gorissen et al. chose to constrain their analysis to actuators with a 1 mm outer diameter, while the variety of actuators in this work were constrained to a fixed inner diameter, as prescribed by the pins of the open faced molds. The guiding principle remains the same, though fabrication methods influenced which variables were constrained while exploring the design space. Further, while this model provides a valuable design guideline,

the exploration in the work presented in this chapter is predominantly focused on assessing manufacturing feasibility and the design space achieved by our new fabrication methods.

4.4.1 Actuation direction programmed via strain-limiting fibers

Within an array of dip molded actuators, each individual actuator can be mechanically programmed to bend in an arbitrary direction with appropriately positioned strain limiting fibers in the fabrication process. An example array programmed with this method is shown in Figure 4.1A-D and an overview of the fabrication process, including the fiber incorporation, is shown in Figure 4.2. Encasing fibers into the side wall of the structures causes asymmetric stretching of the actuator when internally pressurized, thereby inducing a bending motion. A schematic of this mechanical programming method and a resulting cross-section can be seen in Figure 4.3A. This strategy is similar to larger scale soft actuators that use fiber reinforcements to program bending motions in fluidic soft actuators [111, 33], as well as similarly-scaled devices [99, 112]. To accomplish this, we lightly tack the fibers onto the open mold pins prior to inserting them into the mold form for dip coating. When the open face mold is dip coated or poured over, and the rubber cures on the pins, the fiber is mechanically incorporated into the side wall of the actuator, and releases from the pin when the mold assembly is removed.

Due to surface tension, a side effect of the fiber on the side of the pin is that the wall thickness is greater on the fiber side of the actuator. This is visible in Figure 4.3A. The corners between the fiber and pin are also more likely to trap bubbles in the dip coating process and one such bubble is shown up close in Figure 4.3A. The greater thickness increases the stiffness of the actuator side wall, while bubbles reduce the stiffness, creating a weak point if they are too large. These effects on stiffness, however, are second to the strain limiting effect of the fiber and we did not observe any failures from popping through bubbles trapped near the incorporated fibers.

4.4.2 Unidirectional actuation established via gravity

The use of gravity as a mechanical programming method is limited to uni-directional actuation, but it is also the least complex and least labor-intensive of the strategies presented in this work. As depicted in Figure 4.3B, the open face mold that has been dipped in liquid rubber is propped at an angle with respect to gravity during the curing process.

As a result, more of the rubber drifts to the lower side of the pin, creating a thickness bias in the side wall of the actuator. When pressurized, the actuators will thus bend in the direction of the lower side because the thinner side wall inflates and stretches more than the thicker side. Given its simplicity, this method is convenient for constructing large arrays of actuators, such as the 256-part array shown in Figure 4.1E-H, as well as the construction of very high aspect ratio actuators like the one shown in Figure 4.4. In a prior demonstration of this mechanical programming strategy in the micro-tentacle created by Paek et al., the soft actuator was formed by curing rubber on a horizontal rod and later sealed after removal from the rod [102]. In this work, curing angles ranging from five to sixty degrees offset from vertical successfully produced bending actuators, though we focused on thirty to sixty degrees. The open face mold creates a sealed actuator tip while also pneumatically coupling the actuators to the rest of the array.

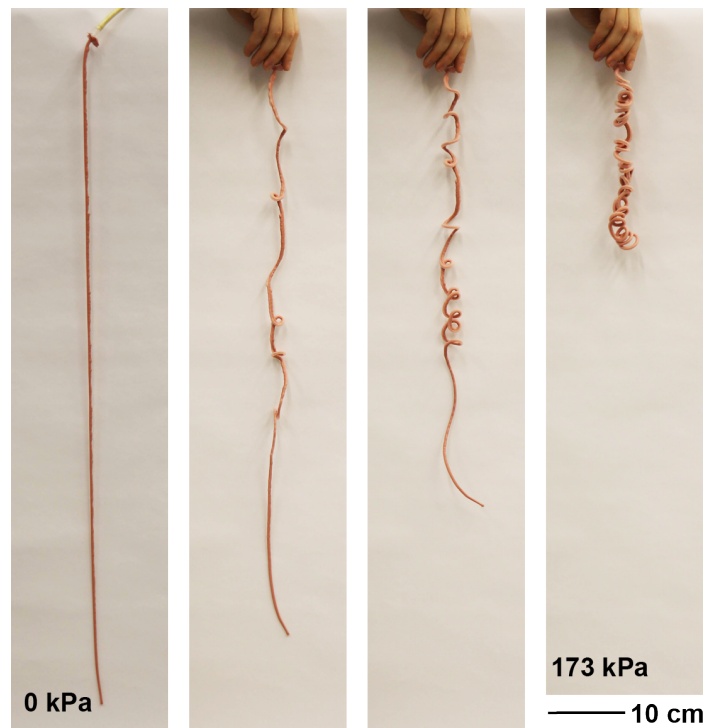


Figure 4.4: Inflation of an actuator that was formed on a 1.59 mm diameter, 1 m long pin.

An alternative strategy using gravity to create a structural bias in the dip-molding process, depicted in Figure 4.3E, uses droplets formed at the tips of an inverted open faced mold shortly after dip coating. The mold is then rotated 90° and the liquid silicone droplets

shift to one side of the pin tips. The mold is then fully reverted such that the pins are pointing upward and the droplets then run down one side of the pins, leaving a thicker coating of rubber on one side.

4.4.3 Actuation direction established via surface tension

Similar to programming the bending motion of an actuator with fiber inclusions, the use of surface tension as a mechanical programming strategy allows for arbitrary arrangement of bending directions within an array of actuators. The bending motion is determined by biasing wall thickness through the use of pins with non-circular cross-sections. The cross-sectional profile of the pins is designed to leverage passive effects of surface tension on the liquid silicone to create thick and thin portions in the rubber coating. A schematic of this concept is shown in Figure 4.3D, as well as images of cross-sections from two actuators. The interior profile of the actuator is defined by the pin shape while the exterior profile of the pin coating will tend toward a cross-section that minimizes the overall surface area, owing to surface tension acting on the liquid rubber. The pin geometry can thus be used to create thicker sections where rubber fills into concave pin surfaces, and thinner sections around features that protrude further and have tighter convex curvatures than neighboring features. We explored pin designs that focus on the creation of thick and thin features, and found that designs that leveraged convex protrusions to create thinner wall sections were more successful at achieving a bending motion through differential wall stiffness and greater curvature at lower actuation pressures. Additional pictures of pin designs and functional actuators can be found below in Section 4.5.4.

4.4.4 Actuation direction established via electric fields

The final method for mechanical programming makes use of static electricity to introduce a net charge into the liquid rubber-dipped pin. The pin is connected to a high voltage power supply and a nearby grounding electrode is used to attract the mass of the rubber off center with respect to the axis of the pin. This method does not allow for the creation of a fully arbitrary vector field of actuation, but does enable non-uniform actuation directions depending on the electrodes employed and electric field formed in the vicinity of the open-faced molds. A schematic of this setup and a cross-section of a resulting actuator is shown in Figure 4.3C. In this work, demonstrations were limited to single pins and small

arrays connected to a -5 kV potential, which are shown in Section 4.5.5. Future work can be done to expand these into larger arrays, taking care to account for effects of multiple pins in the same electric field. To develop an understanding of the electric field acting on the rubber coating a single pin, a simulation of the electric field was made using an approximation of the pin as a point charge and the electrode as an infinite ground plane. Results from this simulation are shown in Section 4.5.5.

4.4.5 Comparison of mechanical programming strategies

The modification methods presented here have different advantages and disadvantages. The gravity method is the easiest to set up for large arrays in that any mold can be propped to a fixed angle while curing to accomplish the goal of mechanical programming, but is limited in that all actuators will then bend equally in the same direction. Fibers allow for arbitrary direction selection but must be manually placed in the desired direction. This can be automated but is time consuming when assembling by hand. Surface-tension programming also allows for arbitrary direction arrangements and could provide variation in output curvature between different pins, as well as over the length of one pin, for a given input pressure. The output curvature versus input pressure can also be varied axially along the pin by varying the pin shape along its length. The surface-tension strategy does, however, require custom pins, (though pins may be reused). Electric-field programming can also support custom arrangements of actuation directions but this is limited by the complexity of electric field interactions as the number of charged pins increases.

Because the gravity and fiber programmed actuators achieved a higher burst pressure, tighter curvature, and higher engagement forces, we focused on these two methods for further exploration and characterization in Section 4.6. The surface tension and electric-field programmed actuators were not able to curl sufficiently to engage with some of the characterization tests described below but there is documentation of several functional examples in Section 4.5.5. The surface-tension method was limited to one or two dip coatings at the scale used for this exploratory work. The first and second coatings achieve the greatest differential in wall thickness and, as the pin geometry is covered by rubber, successive dip coatings add even layers and thus reduce the relative difference in wall thickness. Adjustments might be made to work around this and achieve a tighter curvature and higher engagement forces by exploring the use of different rubbers, alternative pin fabrication

methods that would allow further geometry exploration that is not possible with the 3D printers used in this study, or multiple rubbers of varying stiffness to exaggerate the effect of the first layers while successive layers could just provide a soft skin to increase the overall thickness. Similarly, the electric-field actuators were limited by a low differential in wall thickness, as is visible in Figure 4.3C. This differential could be enhanced with a stronger electric field by increasing the applied voltage, adjusting the electrode shape, or moving the pins closer to the electrode. The rubber could also be doped with magnetic materials to make it more responsive to the applied electric field.

A summary of the mechanical programming methods that we were able to successfully demonstrate with our dip coating process is shown in Figure 4.5. This is similar to Figure 4.3, with the addition of specific dimensions on the cross-section images of the example actuators. These dimensions are from a small sample set and thus do not represent the dimensions of the full design space of the actuators made with our dip coating method, but are meant to help illustrate patterns and distinctions between the various mechanical programming strategies. One such pattern is that the gravity-angle programmed methods showed the greatest differential in wall thickness within a single actuator. By contrast, the wall thickness differential in the electric field and gravity droplet formation strategy methods are very low. In the case of the fiber-inclusion strategy, it was not the goal to create a thickness differential in the side wall of the actuators, but a difference still resulted from the presence of the fiber and its effect on the pin shape and surface tension in the dipping process. Though there is a thickness differential within the sidewalls of the fiber-programmed actuators, the strain limitation of the fiber creates a more significant effect on the bending motion of the actuator than the wall thickness variation. The two example cross-sections of the surface-tension programming strategy also exhibit unique distributions of thickness in that there are more abrupt, almost discrete transitions between thick and thin portions of the side wall. This could be further exaggerated with different pin designs, although the thickness differential created using surface tension cannot continue to increase with successive dip coatings. The absolute difference between thick and thin sections increases with successive dips for the gravity and electric field strategies, but decreases for the fiber and surface tension strategies. Furthermore, while the fiber-inclusion actuators continue to function with the increased number of dips and overall thickness, as do the electric field and gravity programmed actuators to a degree, the surface tension strategy is limited to creating relatively thin actuators of one or two coatings with the current rubber and pins

being used.

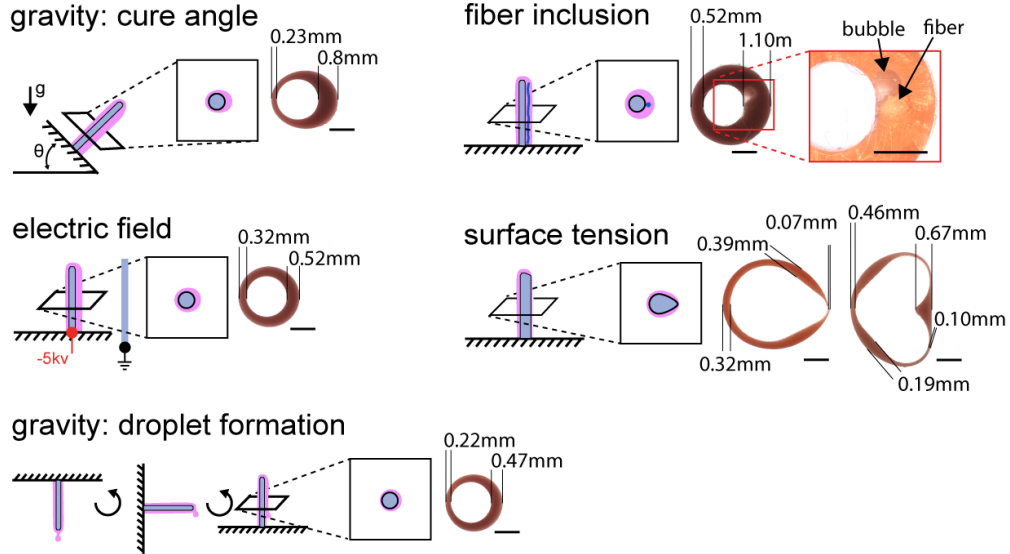


Figure 4.5: Motion programming fabrication schematics with measured cross-sections of sample actuators.

4.4.6 Scale and aspect ratio limitations

To explore the size and aspect ratio limitations of this process, dip-coated actuators were made on pins ranging from 0.4 mm to 6.35 mm in diameter, and 6.35 mm in to 1 m in length, some of which can be seen in Figure 4.4 and Figure 4.6. Qualitatively, 0.4 mm was found to be challenging because the rubber starts to collect into droplets due to surface tension and these droplets significantly affect the function of the final actuator. The next size up, 1.59 mm, was found to reliably produce functioning actuators without the formation of droplets during the dipping and setup process. A small actuator diameter is appealing in the pursuit of high aspect ratios, lower bending moments, and a higher packing density in arrays. Therefore, as the smallest reliable size, we used 1.59 mm pins to create actuators ranging from 6 mm 1 m in length. Most of the process characterization was done with actuators formed on 38.1 mm long pins. These were chosen primarily by price point from the supplier and to have sufficiently long actuators to characterize bending radius versus operation pressure and to be able to curl fully around small objects.

The longest actuator fabricated for the purpose of this study was formed in three coatings on a 1 m long rod with a diameter of 1.59 mm, and cured at an angle of 45° to create

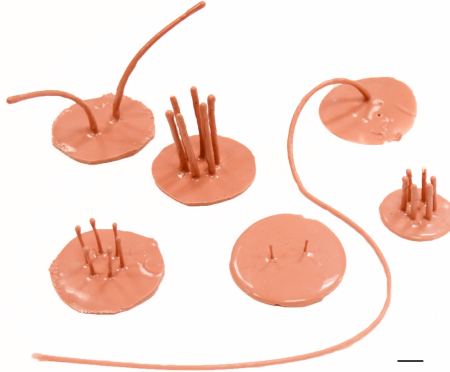


Figure 4.6: Demonstration of a range of aspect ratios achievable with variations on the dip coating fabrication method. The shortest actuator pictured is 6.35 mm long, and the longest is 30 cm. The scale bar in the image represents 1 cm

a bias in the wall thickness. A picture of this actuator at several stages of inflation between 0 kPa and 173 kPa is shown in Figure 4.4. After three coatings of rubber, the effective aspect ratio of the actuator was 200:1 in its resting state. The appropriate length, and thus aspect ratio, of a desired actuator will depend on the intended application. Actuators with embedded fibers were also fabricated up to 1 m in length, but the gravity programmed actuators were easier to demold and create a more consistent curling radius over the length of the actuator. Ultimately, the limiting parameters for the maximal aspect ratio are the curing time, viscosity, and surface tension of the rubber used. Additionally, long pins used for dip coating will start to bend under their own weight. We found that a steeper curing angle, such as 10° from vertical, is sufficient to mitigate this but it is also yet unclear what the utility of actuators longer than 1 m may be.

4.5 Fabrication details for motion programming methods

The actuators in this work were made from silicone rubber, Elastosil m4601 (Wacker Chemie) because of its high elongation at failure (700%), high tearing stress, and relatively low cost. The open faced dip coating molds were fabricated with laser-cut acrylic and stainless steel pins. The pins used to demonstrate the gravity, electric field, and fiber inclusion strategies were 1.59 mm, 38.1 mm long stainless steel pins (McMaster PN:90145A427). The surface tension pins were custom pins and are discussed in Section 4.5.4.1. The fabrication process was also successfully reproduced with pins and molds made

from varying plastics, including polyethylene, Teflon, and Delrin. The rubber does not stick to these materials and, once cured, they can be removed without the use of mold release. This is important to avoid mixing mold release into the liquid rubber, which would create a risk of thin spots and holes in the sidewalls of the actuators. While all of these materials successfully produced actuators, acrylic was used for mold structures because of its ease of laser-cutting and stainless steel pins were selected for their ability to rigidly hold their form, thus making it easier to assemble large, well-aligned arrays of pins. The pins could also be temporarily press-fit into a laser-cut acrylic fixture without risk of bending. For all variations of the fabrication process other than fabricating the actuators on the 300 mm and longer pins, the tips of the pins were dipped in rubber and allowed to cure before applying the first full coating. Without this step, the actuator tips would be too thin, resulting from gravity and surface tension affecting the rubber distribution. If all pins in an open-face mold assembly are the same length, the assembly can all be dipped at the same time for efficiency.

4.5.1 Actuator plumbing

For testing purposes, the individual actuators were pulled off of the printed pins after fully curing and mounted onto a 1/16" barb to Luer Lock fitting. Cotton twine (same as above) was wrapped two to four times around the base of the actuator to help secure the actuator to the barb fitting and a small amount of silicone glue (silpoxy, Reynold's) was added to further secure the twine. Without this wrapping to secure the actuator to the barb, the base of the actuator expands at relatively low pressures and is blown off of the barb. The same process was used to mount the gravity-programmed and electric-field-programmed actuators for testing, as well as for the gripper described in Chapter 5. A larger barb was used to mount the surface-tension-programmed actuators, as mentioned below.

4.5.2 Fiber inclusion pin preparation

To incorporate fibers into the actuator side walls, we lightly tack the fibers onto the open mold pins prior to dip coating. A small amount of silicone glue (Silpoxy, Smooth-on) was used for the tacking because it can be incorporated into the final actuator structure. A minimal line or several spots of glue was first applied to the pin and then lightly pressed against a pre-cut fiber. Cotton fibers were found preferable because they have a high surface

area for better mechanical integration into the liquid rubber. For the demonstrations shown in this thesis, a cotton twine (McMaster-Carr PN1929T12) was untwisted to isolate one of the plies. One of the plies was then cut to size, and tacked onto the pins. The length of the fiber should cover the exposed length of the pin after it is inserted into the fixture for dipping (or pouring). We did not find that this needed to be precise, and gaps between the pin and fiber end up to 4 mm on either side were tolerable, although we tried to keep them below 2 mm or 3 mm. When fabricating the longer actuators, (approximately 300 mm and longer), the ends were trimmed after curing and thus the fiber positioning was less critical.

4.5.3 Fixtures for gravity programmed actuators

Laser-cut acrylic fixtures, such as the ones shown in Figure 4.7, were used to create the gravity programmed actuators with different angles of tilt during the curing process. Our testing focused on angles of 15°, 30°, 45°, and 60° from vertical. For each batch of actuators, we dipped a set of nine pins and removed one or two actuators after each successive dip to create and compare actuators with different numbers of dip coatings that were fabricated in the same production run.

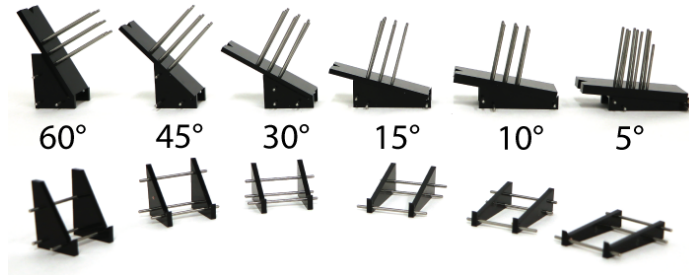


Figure 4.7: Fixtures used to fabricate gravity programmed actuators at varying degrees of tilt for the curing process.

For the gravity-programmed actuators used in the gripper presented in Chapter 5, the angle was reduced to 10° from vertical to minimize bending in the rods, which were mounted from above with the bottom hanging free to facilitate dipping long pins, further described in Section 4.7.2. For the 1 m long actuator shown in Figure 4.4, the pin was supported on both ends.

4.5.4 Fabrication of surface tension programmed actuators

4.5.4.1 Surface-tension pins

Custom sets of pins were printed for the surface tension tests. They were printed both as individual pins and sets of four to nine pins, similar to the set shown in the CAD image in Figure 4.8. The custom pins used for the surface tension experiments were printed on a Formlabs Form 2 printer in the clear resin (RS-F2-GPCL-04, Formlabs). This printer and resin were chosen because it had sufficiently high print resolution and the printed pin could be pulled from the cured Elastosil M4601 rubber without the use of mold release. Furthermore, the printed parts did not inhibit the rubber from curing, as was the case with parts printed with Stratasys resins. Other silicone rubbers were tested with molds created with Formlabs resins, including Reynold's Dragon Skin, Smoothsil, and Ecoflex series. The use of Elastosil M4601 was chosen for reasons mentioned above, but it also released from the Formlabs resin without mold release more easily than the other rubbers that were explored. The approximate pin diameters were increased from the 1.5 mm used in the other programming methods to 2 mm to 3 mm in order to achieve sufficient stiffness such that the pins could be printed with little to no support structure contacting, and thus marring, the molding surfaces. For larger production of custom pin forms, one could switch to injection molded or extruded plastic pins. This may also allow for smaller diameter pins than 3D-printing, if desirable.

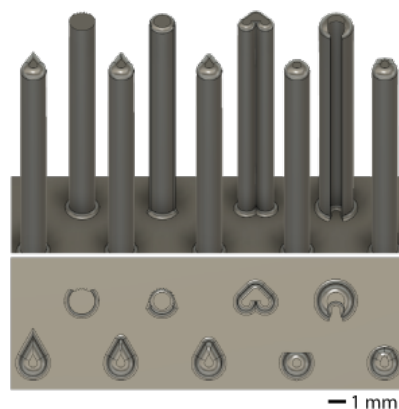


Figure 4.8: Example CAD model of custom pins printed for surface tension motion programming method.

As mentioned in Section 4.4.3, the most successful pin designs were those designed

to specifically control and place the thin sections of the actuator side wall for high expansion areas, as opposed to the designs that prioritized the concentration of material to limit strain. The placement of thinner sections is dictated by convex surfaces with tighter curvature. From the initial testing, this programming of thin sections was achieved most successfully with “tear drop” and “heart” shaped cross-sections, as shown in 4.9. The radius of curvature in the wide and narrow sides of the tear drop is 1.5mm and 0.25mm, respectively, and the radii of curvature of the heart bottom and upper lobes are 1.5mm and 1mm, respectively.

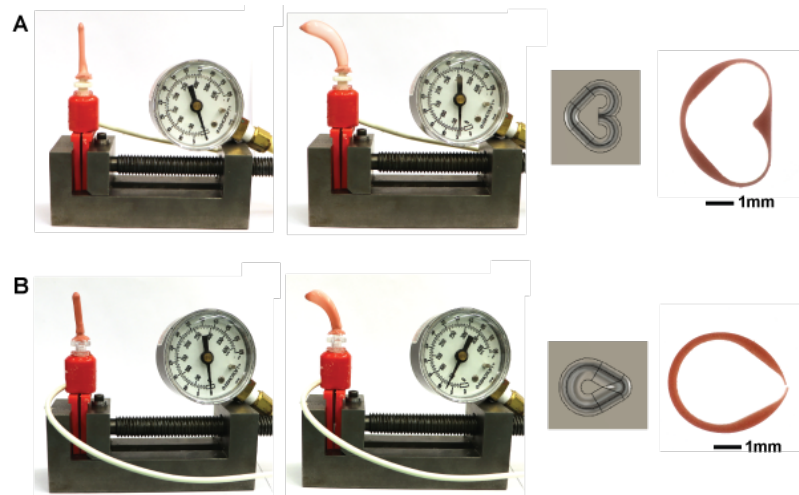


Figure 4.9: Picture of pressurized actuators programmed with surface tension and their cross-sections. The actuator shown in (B) was inflated to the point of failure and the point of rupture can be seen in the cross-section photo.

4.5.4.2 Surface-tension actuator plumbing

One or two coatings of the heart and droplet pins produced a functional actuator, but further dips reduce the functionality of the resulting actuators because the first dip creates a layer that inherently obscures the pin geometry, making it less influential on successive dips. For testing purposes, the individual actuators were pulled off of the printed pins after fully curing and mounted onto a 1/8” barb to luer lock fitting. Cotton twine was used to help secure the actuator to the barb fitting and a small amount of silicone glue (Silpoxy, Smooth-on) was used to fill gaps between the base of the actuators and the barb that result from the non-circular cross-section.

4.5.5 Fabrication for electric-field programming

4.5.5.1 Fabrication setup

Two examples of dip molded actuators programmed with the use of an electric field are shown in Figure 4.10. These actuators are the result of one and two dip coatings, using a -5kV potential to bias the thickness of the rubber coating the pin to the side nearest to a grounded plate. This results in a small difference in wall thickness, but is sufficient to produce a bending motion when the actuators are pressurized.

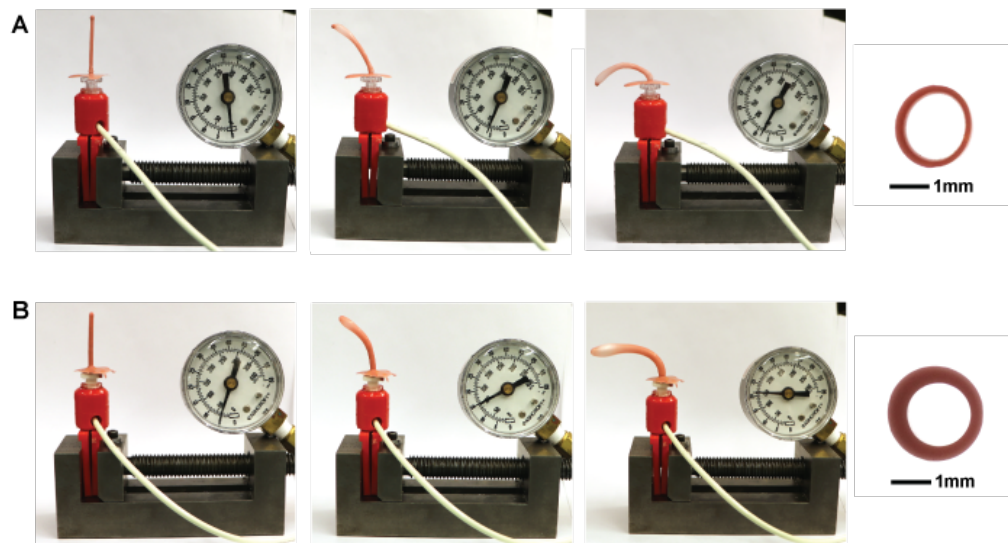


Figure 4.10: Picture of actuators programmed with electric fields and their cross-sections. The actuator shown in (A) was made with one dip coating and the actuator in (B) was made with two dip coatings.

One setup for the electric field programming strategy is shown in Figure 4.11. The same 38.1 mm long stainless steel pins referenced above were used for the electric field experiments. The pins were press fit into holes laser cut into 3.2 mm thick acrylic plates. The bottom of the pin was pushed through the acrylic plate to the point of sticking out approximately 6 mm and a copper wire was striped and wrapped around the base of the pins to provide a connection to the high voltage power supply. Underneath the wire wrapped pins, another acrylic plate was added to the bottom of the assembly for stability.

With the copper wire attached to the pins but not the power supply, the pin (or multiple pins) in the assembly was dipped first on the tip and cured to prevent thin spots at the tip. They were then fully submerged into a freshly mixed cup of rubber and then

placed next to the grounded plate. The copper wire was then connected to a power supply set to provide an electric potential of -5 kV . An aluminum plate, 0.2 cm thick, 3 cm tall, and 2 cm wide, was positioned 1.5 cm from the pin and connected to ground. This was successfully tested with the flat side of the plate most proximal to the pin as well as having the thin edge most proximal to the pin. The cross-sections and inflation tests shown are from the setup with the thin edge of the electrode positioned nearest to the pin in order to generate a stronger field concentration in the vicinity of the pin.

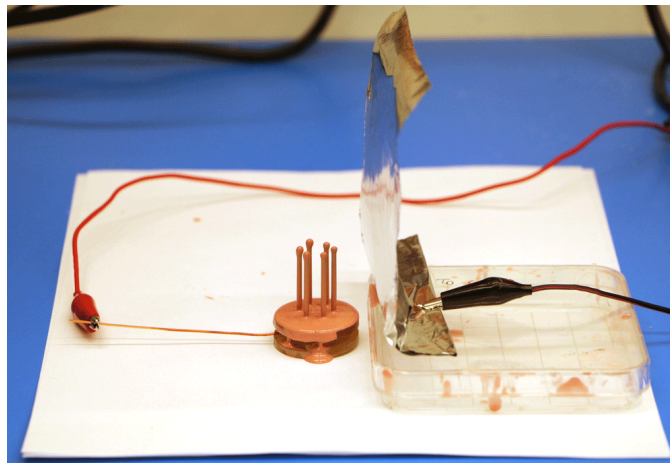


Figure 4.11: Picture of electric field programming test with an array of pins connected to a -5 kV potential and positioned next to a grounded sheet of aluminum.

The setup was left to cure at room temperature while in a charged state until the rubber reached a point where it would not reflow and change the thickness distribution once the potential field was removed. The power supply was turned off approximately three hours after the initial dip. Another trial was run with the help of a heat gun to speed up the curing process. In this run, the power supply was turned off twenty minutes after the initial dip. The flow of the heat gun was directed downward over the pin and kept on a low setting so as not to blow the uncured rubber around on the pin. Both trials produced similarly functional actuators. Once sufficiently cured and the power supply turned off and disconnected, the pins were removed from the rubber.

Another example of the electric field programming strategy setup is shown in Figure 4.12. The primary differences between the two setups shown in Figure 4.11 and Figure 4.12 are the grounding plate and its orientation, and the number of pins included in the array. Both setups produced similarly functional actuators. For simplicity, the setup in

Figure 4.11 was used as the sample setup to explore in the simulations below. Intuitively, we would expect the edge of a plate to create a more concentrated electric field than the flat side of a plate, and that the presence of multiple pins will affect the field that is experienced by each individual pin.

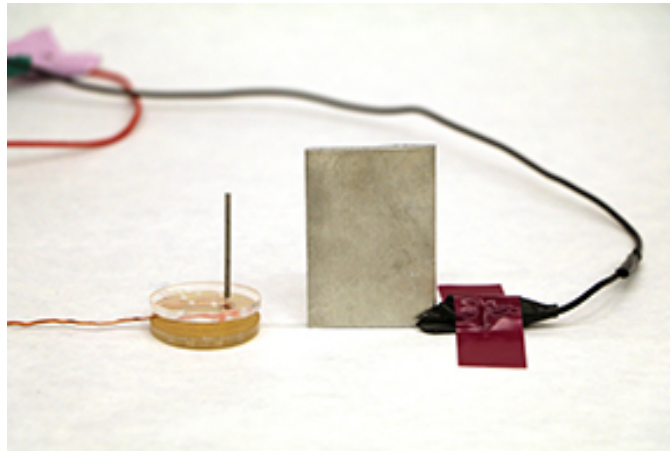


Figure 4.12: Picture of electric field programming test with a single pin connected to a -5kV potential and positioned next to the edge of an aluminum plate.

4.5.5.2 Electric-field modeling

A model was created by Kevin Chen to help illustrate the electric field for a simplified setup similar to that of Figure 4.11. The pin was approximated as a line charge of -5kV and the aluminum plate as a grounded infinite plane. Results from this model are shown in the plots below, in which the axes represent the physical spacing of the experimental setup in meters. A representation of the predicted electric field is shown in figure 4.13. The relative intensity and polarity of the electric field is then mapped in Figure 4.14, showing the magnitude of the X, Y, and Z components of the electric field at the base, mid point, and top of the pin. Each of the plots depicts the experimental setup as viewed from above, with the grounding plate indicated by a red line at the top of the plot. While the modeling of larger, more complex arrangements of actuators programmed with the use of electric fields would be out of the scope of this work, we used the simplified model to aid in our understanding of the forces acting on the rubber during the forming and curing process and the sensitivity of these forces to the charge provided to the pin and the spacing between the pin and the grounded plate. Further modeling of complex setups could provide a fruitful

exploration of how to mechanically program functional motion patterns into a larger array of these actuators but we limited our experimental variables. For our feasibility tests, we were interested to know whether individual actuators could be successfully fabricated and demonstrated, whether an array fabricated in parallel could be made functional despite the possible electrical field complications, and whether this mechanical programming strategy would be compatible with the dip coating process.

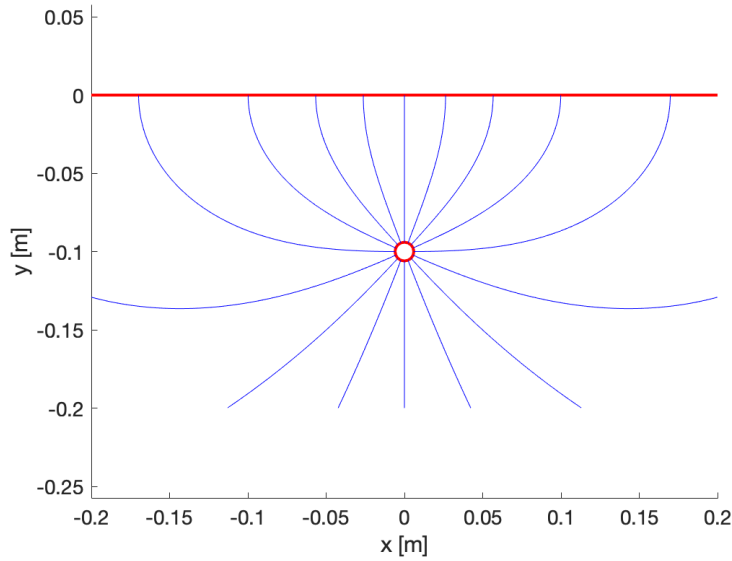


Figure 4.13: Above view of the electric field formed between pin charged to -5kV and a grounded plate with a 10cm gap between the grounded plate and the dip coating pin. The lines represent the direction and relative concentration of the electric field as compared to the field shown in Figure 4.15. From the plot, a fabrication setup with this spacing seems unlikely to be successful in creating a bias in the wall thickness of a dip-coated actuator.

The model represented in Figure 4.13 and Figure 4.14 depicts a setup where the dip coating pin is 10cm from the grounding plate. Figure 4.15 and Figure 4.16 show how that compares to a setup in which the dip coating pin is 2cm from the grounding plate, assuming all other parameters are held constant. Figure 4.14 and Figure 4.16 show that the orientation of the electric field is similar between the two setups and, as expected, the z-component of the field is radially symmetric and goes to zero in the middle of the pin. Comparing Figure 4.13 and Figure 4.15, it can be observed that the increased proximity of the grounding plate, reducing the gap from 10cm to 2cm , changes the distribution of the electric field surrounding the pin, creating a bias where the magnitude of the electric field

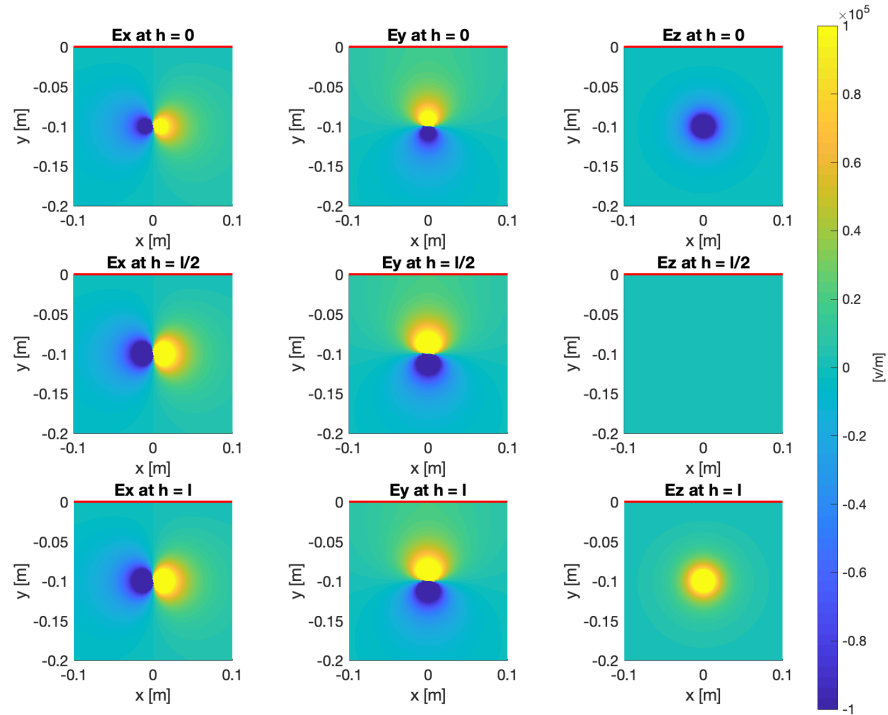


Figure 4.14: Electric field intensity map for various orientations with 10cm between the pin charged to -5kV and a nearby grounded plate.

near the grounding plate is larger. This is important to be able to pull the rubber to one side of the pin, thereby forming the bias in the wall thickness of the resulting actuator, which then induces a bending motion upon inflation. This bias could be further increased by applying a larger charge to the pin, decreasing the distance between the pin and the grounding plate, and using a narrower geometry of the grounding plate to create a local concentration in the electric field. An example of a narrower geometry would be to simply turn the edge of the plate toward the pin, as depicted in Figure 4.12. Material-based options for exploration could also include additives to adjust the material's permittivity, or incorporating magnetic particulate. It would be important, however, to be mindful of effects on the bulk mechanical properties of the resulting composite material. Adding particles to the rubber could also increase the risk of pin holes and thus leaky actuators.

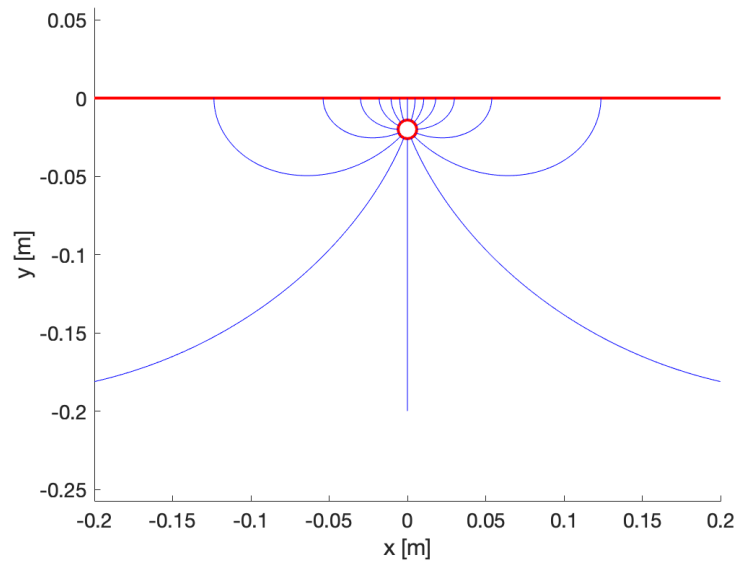


Figure 4.15: Above view of the electric field formed between a pin charged to -5kV and a grounded plate with a 2cm gap between the plate and pin. The lines represent the direction and relative concentration of the electric field as compared to the field shown in Figure 4.13.

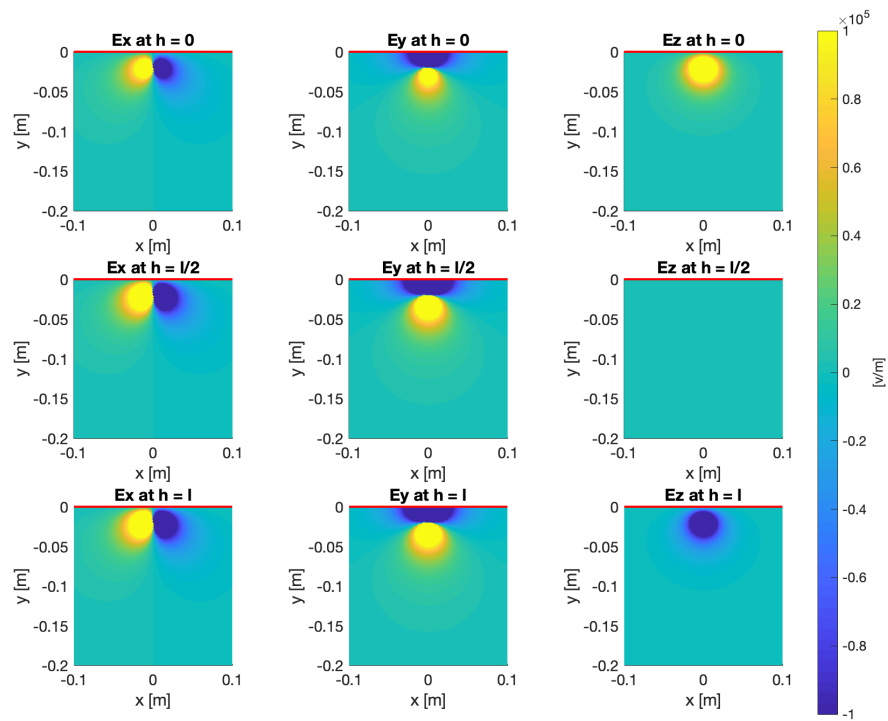


Figure 4.16: Electric field intensity map for various orientations with 2cm between the pin charged to -5kV and a grounded plate.

4.6 Characterization of individual actuator performance

The characterization of the actuator arrays produced by the dip coating and programming strategies presented here was motivated by potential applications in manipulation of fluid flow and discrete objects, distributed grasping tasks, and locomotion. In the interest of these applications, the unconstrained curvature and holding force were measured for various fiber and gravity programmed dip coated actuators. The goal of these tests was to assess the sensitivity of actuator performance to fabrication parameters, including the number of dip coatings, the mechanical programming method, and variations within the programming method such as the pin angle. In the case of pneumatic actuators, one might want to tune a structure to bend a certain amount at a fixed pressure or tune a structure to have a specific threshold of engagement force. These tests are aimed to map a portion of the design space, as affected by fabrication variables, to allow intentional selection of the operating parameters.

Having a map of the operating pressures, resulting curvatures, and grasping forces is useful in selecting appropriate fabrication recipes to build actuators for an intended task. Another important consideration is matching to a suitable pneumatic power and control system that must be balanced with the operating parameters of the actuators. The internal pressures applied to each of the actuators was varied between the point when minimal pressure before deflection was observed up to failure by leaking or rupture. The results of these tests were used to inform fabrication parameters for the construction of the two arrays of actuators in Figure 4.1, as well as the high aspect ratio actuator in Figure 4.4. Following curvature and force characterization, a subset of the actuators were subjected to destructive testing. They were inflated to rupture to measure burst pressure and sliced to expose the cross-sectional distribution of thickness.

Smaller sample sets of operational pressure tests were also performed on actuators programmed with surface tension and electric fields but they were not subjected to grip force testing because they did not achieve a sufficiently tight curvature to hold on to the testing fixture. Further development of these mechanical programming strategies may enable greater curvature, otherwise they may only be used for applications that require less bending range, such as fluid flow manipulation.

4.6.1 Operational pressure and curvature characterization

The unconstrained curvature was measured through a range of inflation pressures from the initial deformation up until the actuator curled onto itself. Tests were stopped when the actuator came in contact with its own base, or earlier if the actuator leaked or burst before fully curling up.

4.6.1.1 Automated measurement of curvature and operating pressure

To help with the characterization of operating pressure and curvature, Kevin Chen wrote a custom image processing script in Matlab (Mathworks) to track the edge of actuators in a series of pictures taken at various pressurization levels. Though the image tracking program was set up to find the inner and outer edge of the actuators, the outer edge was used for the curvature measurements below because it was more easily identified in the pictures by the tracking script due to the lighting in the pictures taken for this data set.

Given a raw image like the one shown in Figure 4.17A, the algorithm thresholds the image based on the color differences between the actuator and the background. The largest component in the foreground is identified as the actuator. Based on this segmentation result, the raw image is converted into a black and white binary image, such as the one shown in Figure 4.17B. Next, the algorithm finds the outer contour of the actuator. The result is shown in Figure 4.17C and it is accomplished by computing the gradient of the binary image shown in Figure 4.17B. Based on this edge contour (shown in white in Figure 4.17C), the algorithm identifies an outer arc (red) and an inner arc (green). These arcs are found by first identifying the actuator's base and tip locations, and then splitting the edge contour into two parts. Figure 4.17C shows that the middle 30% of the upper and the lower contours are identified as the outer and the inner arcs.

We calculate the arc radii and centers through least-square regression. The equation of a circle is given by:

$$(x - a)^2 + (y - b)^2 = c^2,$$

where a , b , and c are the unknowns. We rearrange the equation into the matrix form: $A\mathbf{v} = \mathbf{s}$, where $A = [x, y, 1]$, $\mathbf{v} = [2a; 2b; c^2 - a^2 - b^2]$, and $\mathbf{s} = x^2 + y^2$. Figure 4.17D superimposes the fitted outer and inner circles on the original image.

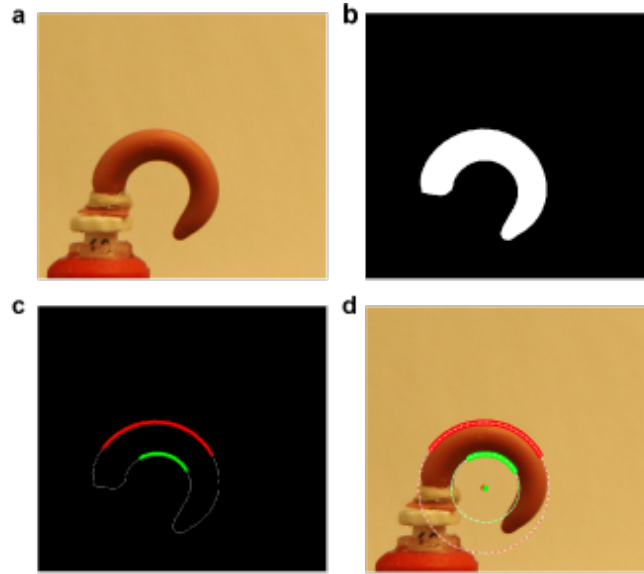


Figure 4.17: An illustration of an automated curvature tracking method. (A) The original image. (B) A binary image distinguishing the background and the actuator. (C) The outer arc (red) and the inner arc (green) are segmented from the actuator’s edge contour (white). (D) Circles are fitted to the upper and lower arcs to estimate bending radii.

4.6.1.2 Resulting curvature and operating pressure relationship

Figure 4.18 shows the curvature achieved at various operating pressures for actuators mechanically programmed with fibers and gravity. The gravity-programmed samples represented in Figure 4.18 were cured at 30° , 45° , and 60° from vertical for the purpose of biasing the side wall thickness.

As may be expected, the most significant fabrication variable affecting the relationship between curvature and operating pressure is the number of dip coatings, and thus the overall thickness of an actuator. As shown in the plots in Figure 4.18, this manifests as discrete jumps between samples with different numbers of dip coatings, where the operational pressures shift higher with each coating. A notably higher operational pressure is also achieved through the incorporation of fibers into the dip coated structures versus the operating pressure of the gravity-programmed structures. Among the gravity-programmed actuators, their curing angle can be used to make finer adjustments to the operating pressures and the initial engagement pressure.

There is an unexpected overlap between two of the lines in Figure 4.18A. Using images taken during each of these pressure tests, we do not notice aberrant behavior of

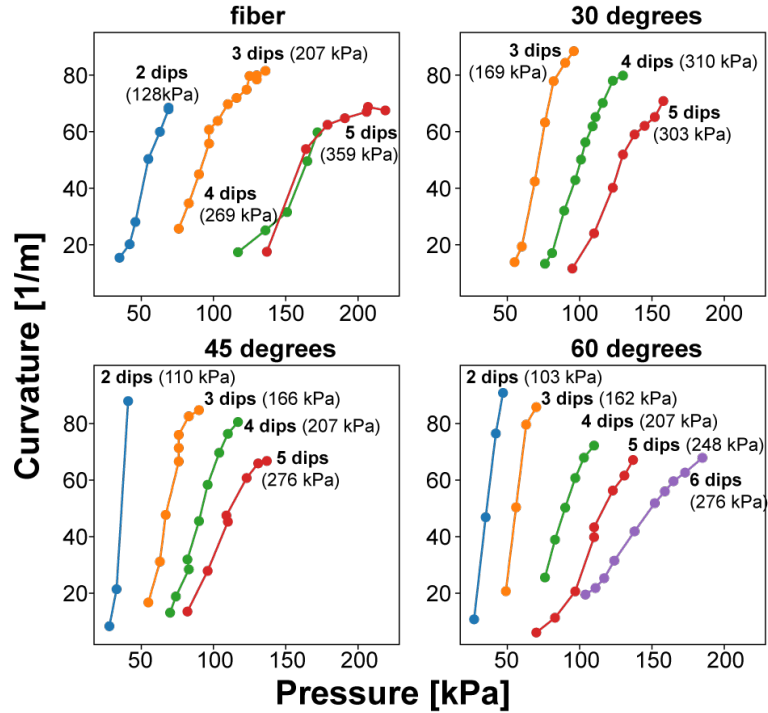


Figure 4.18: Plots of the curvature versus input pressure for actuators made with varying numbers of coatings and programmed with different gravity curing angles as well as fiber embedded actuators.

the actuators other than the fact that the five dip actuator begins to bend out of plane at higher pressures. Bending out of plane would register as an artificially higher curvature in the tracking script. Adjusting for this might move the five dip line downward but does not fully explain the fact that the two, three, and five dip actuators set a pattern that the four dip actuator does not closely follow. From this data and our experience in building these actuators, we draw the conclusion that there is some uncontrollable variance in the fiber programming method due to the hand-placement of the fibers. This may be improved with automation as well as the sourcing of straighter fibers. (The fibers used were unwound from cotton twine to achieve the desired diameter and thus have a residual helical shape that is difficult to straighten.) We do not expect the small variations to be problematic when averaged over large arrays, and the accuracy can be improved if necessary. Another option is to use the gravity programming approach for a higher degree of accuracy and consistency. This also influenced our decision to use the gravity programming method for the largest array and longest actuator prototypes, which benefit from a high degree of consistency.

4.6.2 Holding force characterization

In the interest of gauging the potential for grasping, manipulation, and attachment with these fluidic bending actuators, their holding force was evaluated by measuring the force required to pull a 6.35 mm diameter rod out from an encircling actuator. The effect of varying internal pressurization values was also measured. These tests were performed on an Instron material testing machine with the setup shown in Figure 4.19. The range of pressures represented in the holding force test plots below varies for each actuator due to the variance in operational pressures. For the actuators made with different fabrication parameters, the low end of the pressure range measured was chosen based on the pressure at which the actuator was sufficiently curled to wrap around the rod, as shown in Figure 4.19. The high end of pressure testing was determined by the point at which the actuator could no longer maintain a seal around the barb and Luer lock connection, or the actuator failed. The progression of increasing pressure was also stopped if the actuator showed signs of being near to failure, such as when the rubber reaches sufficient strain to begin turning white. Therefore, plots with a small number of lines had a smaller functional range in which the actuator curled sufficiently and had capacity to operate at increased internal pressures.

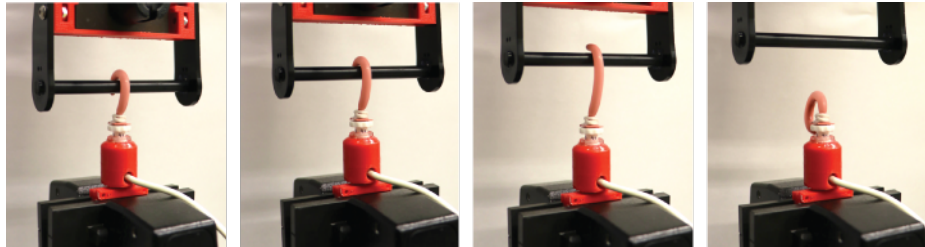


Figure 4.19: Picture sequence of a grip test.

Examples of holding force measurements for three individual actuators with different fabrication parameters are shown in Figure 4.20. The first three example actuators represented in the plots in Figure 4.20 were made with four dip coatings and mechanically programmed by curing at inclines of 15°, 30°, and 60°. The example actuators in Figure 4.20D and 4.20E were programmed with fiber inclusion and made with three and four dip coatings. These plots represent a subset of the collection of tests shown in Figures 4.22, 4.23, and 4.24. Each black line on the plots represents an average value of five trials and the shaded colored line represents one standard deviation above and below the average value. The color of the shaded region behind the lines corresponds to the operating pressure that

was used for each test and the same scale is used on all of the plots. The pressure values for each test are also labeled individually for each line. The oscillations in the plots are due to the stick slip interaction between the actuator and the rod as they slide past each other. A summary of the peak forces for four-dip actuators and various mechanical programming parameters is shown in Figure 4.21.

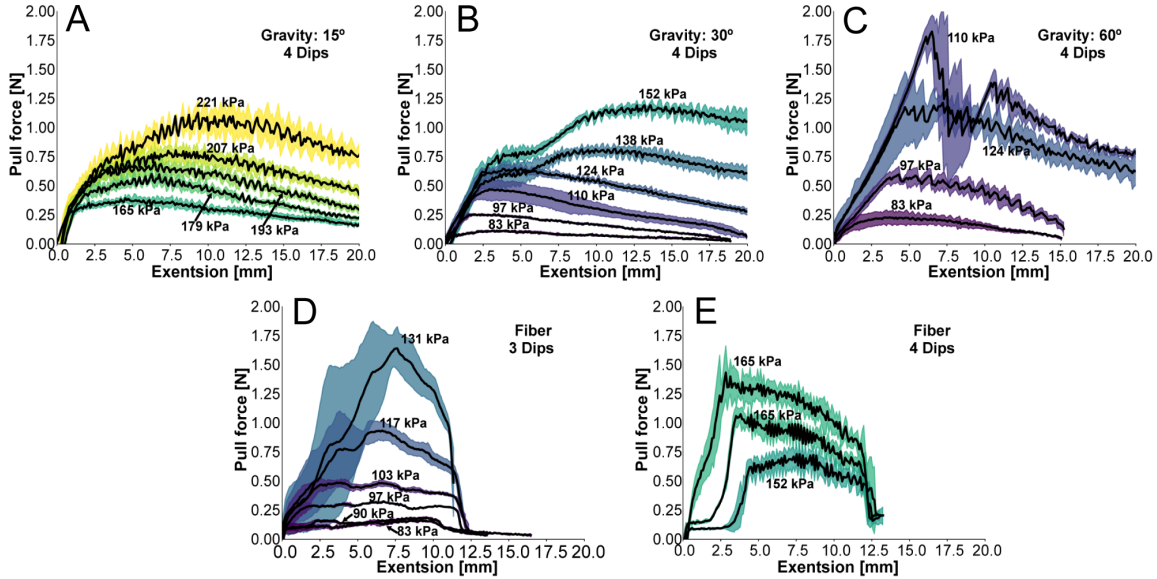


Figure 4.20: Example results from holding force tests. The center line represents the average value of five tests and the colored band is one standard deviation above and below average. The inflation pressure is labeled directly for each line and also corresponds to the color. The actuators represented include gravity programmed samples with four dip coatings and cured at a A) 15°, B) 30°, and C) 60° angles. Plots are also shown for fiber programmed actuators with D) three and E) four dip coatings. Plots of maximum holding forces values for actuators made with four dip coatings are summarized in figure 4.21.

From the results shown in Figure 4.20 and Figure 4.21, it can be seen that the force output is affected by the fabrication parameters, as well as the relationship between curvature and input pressure. In other words, a thicker actuator and higher input pressure does not automatically translate to higher holding forces. The results in these figures show that increasing the pressure in a given actuator will generally lead to an increased pull force, but a different actuator recipe may be able to achieve the same pull force with more or less internal pressure. Comparing this information to the curvature data shown in Figure 4.18 suggests that the relationship between operating pressure and curvature has an effect on the holding capacity of an actuator, likely related to the size of the object being grasped in

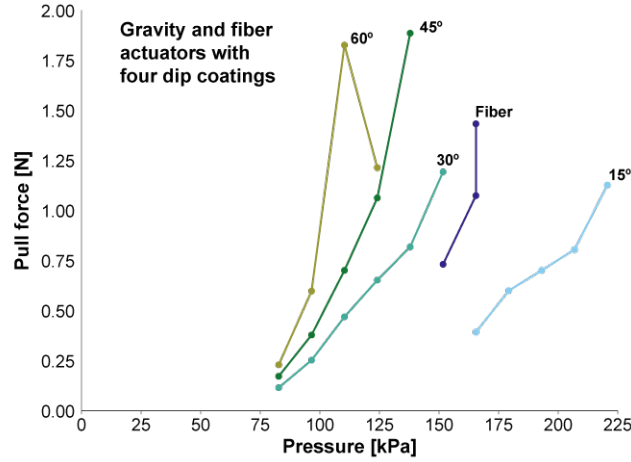


Figure 4.21: Overview of pull test data for actuators with four coatings. Each point represents the maximum average value of a set of five pull test trials, such as the ones shown in Figure 4.20.

relation to the enclosing geometry formed by the actuator.

The force applied to the rod as it is pulled away from the encircling actuator is largely dependent on the friction force between the actuator and the rod, which is affected by the actuator curl and the local contact shape. As would be expected, actuators that do not fully curl around the rod cannot apply an appreciable force in this test. As the rod is pulled out of the encircling actuator, the actuator is extended upward and uncured, which results in a reduced holding force. When uncured, a more distal portion of the actuator is in contact with the rod, creating a more compliant path between the rod and base of the actuator. As the actuator uncurls, there is also less engagement with the rod, resulting in lower friction between the two. As expected, we see that the holding force decreases as the actuator nears its fully uncured extent in all of the plots in Figure 4.20. The actuator surfaces were not specifically cleaned or prepared in any way for the test, but were minimally handled prior to testing. An interesting point for future study would be to test the holding force in the presence of contaminants and lubricants.

The shape of the test curve is also affected by the initial curvature of the actuator, as determined by the inflation pressure and fabrication parameters. For example, Figure 4.20B and Figure 4.20E show trends in several operating-pressure trials that suggest that the actuator becomes better seated with a small amount of extension. Artifacts on the

inner surface, such as bumps from underlying fibers, as well as the tension in the actuator skin can also affect the measured grip force. When the actuator is fully curled but still compliant, the surface of the rubber conforms and sticks to the rod. By contrast, when an actuator is maximally pressurized, the surface conforms less to the rod and does not achieve that same adhesion. A fully pressurized actuator also provides greater resistance to uncurling and will lead to disengagement with the rod. In some cases this translates to reduced contact as that actuator arc does not conform to the rod. In more extreme cases, the actuator may twist sideways and slip off the side of the rod without fully uncurling. We believe these effects at higher pressures are connected to the downward trend seen in the higher pressures in Figure 4.20C.

The compliance of these actuators is both a challenge and an asset. A strategy to navigate the trade-offs of compliance could be to use these fabrication methods to build arrays of actuators that work in concert to grasp and manipulate objects in a way where individual contact forces remain low and gentle, but the distributed forces may add up to a stronger aggregate force. The holding forces achieved by the actuators built in these studies ranged from 0.25 N to 2 N. While these are relatively small forces, one could increase the holding capacity of a system by increasing engagement with a target object by using longer actuators, like the one pictured in Figure 4.4, in addition to using an array of arrays to work in parallel. Chapter 5 explores a grasping strategy of stochastically distributed contact using an array of long (300 μ m) dip-molded actuators. The strategy is referred to as entanglement grasping and the high-aspect-ratio actuators as filaments.

Furthermore, the fact that holding force is not solely dictated by the internal pressure of the actuator, as one might have expected, opens paths for the next steps of this work and the entanglement gripper in the next chapter. Depending on the intended application of the actuators fabricated by these methods, the actuators could be specifically tailored and optimized for certain tasks, optimized for interacting with objects of interest that have characteristic features within a specific range of dimensions, and tuned for desired holding force thresholds.

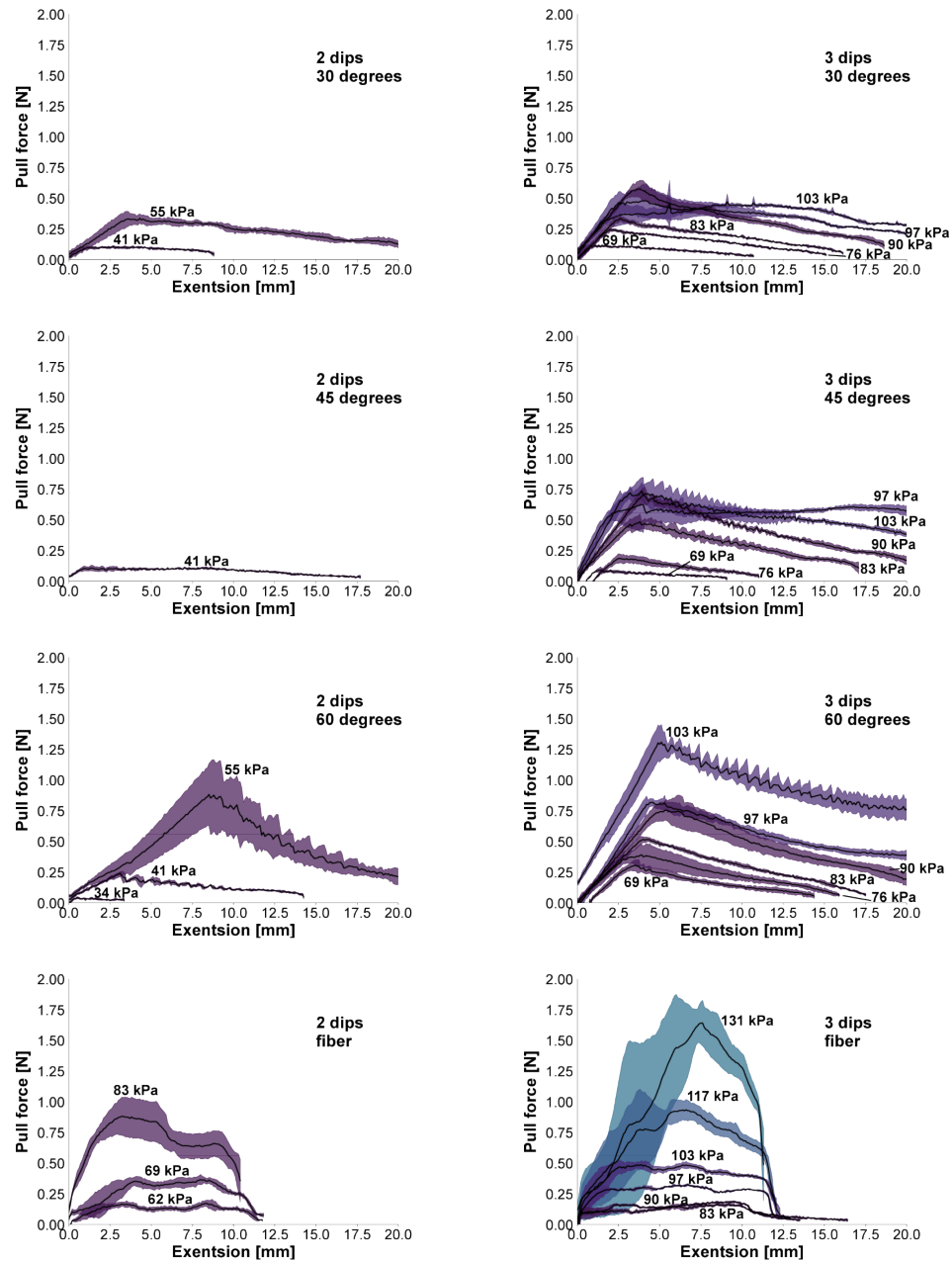


Figure 4.22: Results of actuator holding force testing for actuators with two dip-coatings (left) and three dip-coatings (right). From top to bottom, the actuators were programmed at a 30° angle, a 45° angle, a 60° angle, and with a fiber inclusion.

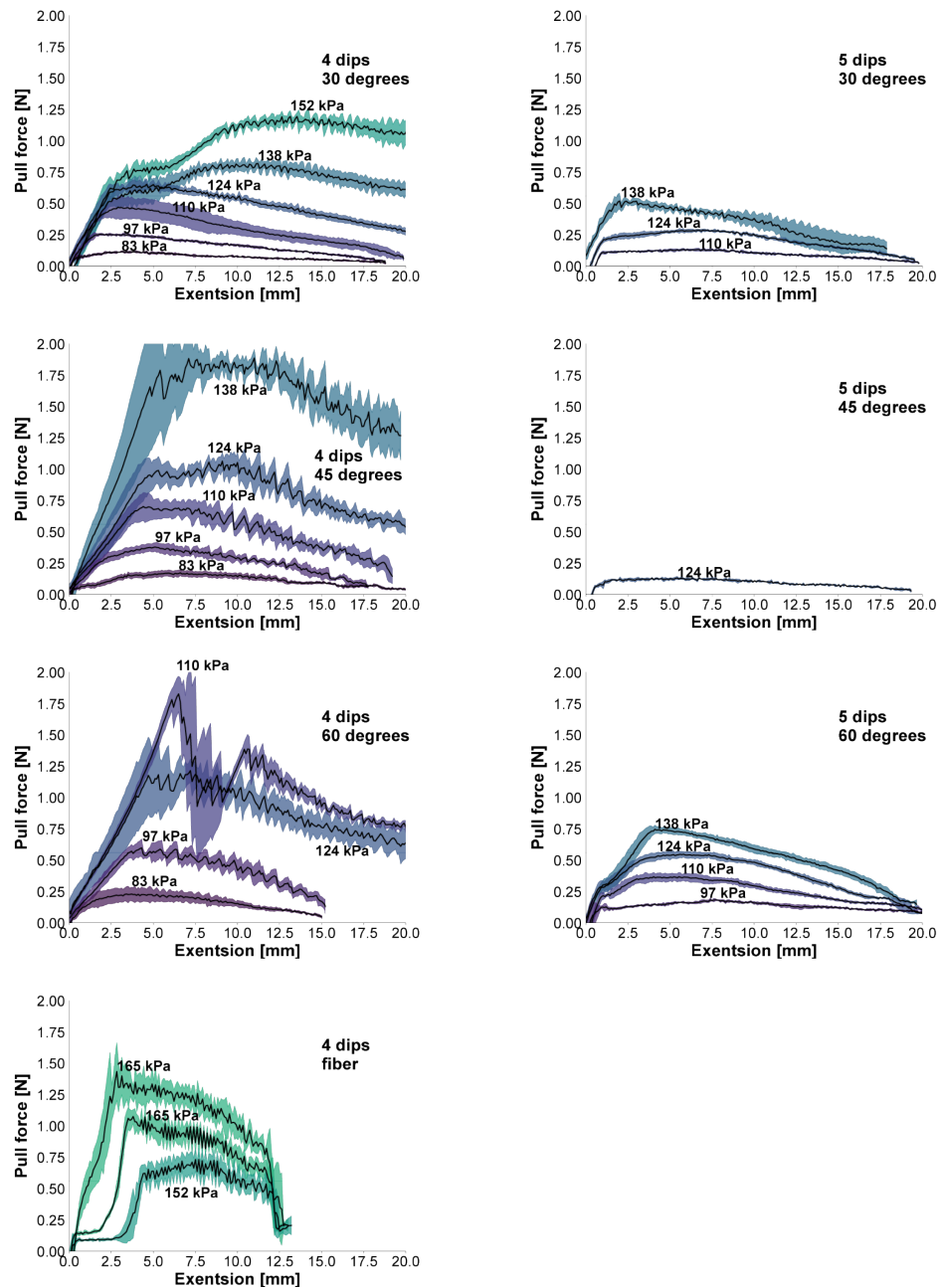


Figure 4.23: Results of actuator holding force testing for actuators with four dip-coatings (left) and five dip-coatings (right). From top to bottom, the actuators were programmed at a 30° angle, a 45° angle, a 60° angle, and with a fiber inclusion.

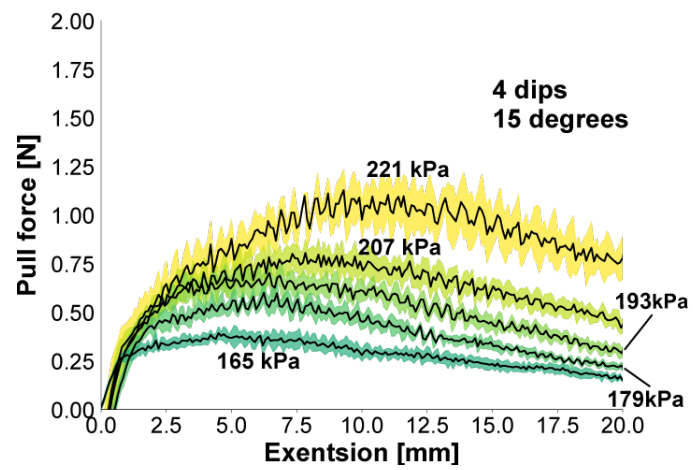


Figure 4.24: Results of holding force test for four dips, fifteen degree gravity programmed actuator.

4.6.3 Burst pressure

After operational pressure testing and holding force tests were performed, individual actuators were pressurized to the point of failure by bursting. In each case, the failure point was a rupture in the thinner side of the actuator wall, near the base. Intuitively, this was expected because the actuators are formed as a seamless body and the weakest point undergoing the most strain is the thinner side wall a couple millimeters above where the actuators is attached to a barb fitting. The rubber covering the base of the pin tends to be slightly thinner due to surface tension and gravity. A picture of this is shown in Figure 4.28 in the context of the fabrication process for large arrays in Section 4.7. The cotton twine fixing the actuator to the barb covers this thin spot and also constrains extension of the rubber. This edge effect leads to a higher combination of axial and radial strain and thus creates the most probable failure point.

Burst pressure values for the actuators represented in Figure 4.18 are shown in parenthesis, next to the line labels. Figure 4.25 also shows a table of the same burst pressure values that are consolidated, color coded by pressure value, and organized by fabrication variables. Burst pressure values ranged from 103 kPa to 448 kPa for gravity and fiber programmed actuators with two to six dip coatings. As expected, burst pressures increase with the number of dip coatings. Within sets of actuators of the same number of dip coatings, gravity-programmed actuators formed at low tilt angles and fiber-programmed actuators had the highest burst pressure. Burst pressures decreased with increasing tilt angles, related to the fact that larger tilt angles lead to a greater difference between the wall thickness on either side of the pin and thus thinner walls on the upper side of the dip-coated pins overall. The values in Figure 4.25 represent only a single trial each and future work will incorporate larger sample sizes for burst pressure testing, to evaluate variance in the results.

In all fiber-programmed and gravity-programmed actuators at tilt angles of 30°, 45°, and 60°, the actuators were able to curl to their full extent, which was limited by the point at which the actuator tip made contact with the base of the actuator. Gravity-programmed actuators fabricated at tilt angles of 15° and three, four, and five dip coatings were able to curl to their full extent, while those with two coatings only curled up to 180°. Two- and six-coat actuators programmed at 15° were not tested.

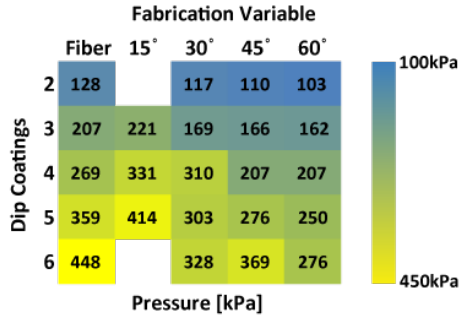


Figure 4.25: Bursting pressure of gravity and fiber programmed actuators made with varying numbers of dip coatings. The colors (ranging from blue to yellow) correspond to the measured burst pressure of a single actuator in each cell, and are mapped to the maximum and minimum values of the table.

4.7 Fabrication modifications for large arrays, long actuators, and control integration

4.7.1 Large arrays

4.7.1.1 Rubber pouring and cycling for large arrays

To fabricate large arrays of actuators without requiring a large reservoir of rubber for dipping, rubber was poured over the top of the pins. Angling the mold for the purpose of using gravity to bias the wall thickness also allowed the rubber to be collected at the lower edge of the tilted mold, funneled into a cup, and re-poured. Care should be taken to limit pouring (and re-pouring) within the working time of the rubber. The rubber will otherwise start to set and it becomes impossible to get an even coating across the array.

4.7.1.2 Strain limiting in the base of arrays

Cotton cheese cloth (McMaster-Carr PN8808K11) was used to help mechanically anchor the layers of rubber forming the top and bottom of the pressure supply channels underneath the actuator array. The cheese cloth also limits the strain in the walls of the pressure supply channels. We chose to use cotton cloth as a means of mechanical anchoring in place of plasma bonding techniques to achieve higher strength with lower equipment requirements, and potentially less material and process sensitivity. The upper surfaces of the cheese cloth are incorporated into the first dip coated layer. As depicted in Figure 4.2,

after the mold components have been removed, the cheesecloth on the underside of the array is later used to mechanically bond the structure to a new layer of rubber that closes the bottom side of the pressure supply channels. The new layer is poured on a flat surface and the array is carefully pressed into the pool of liquid rubber and allowed to cure. A layer of cheesecloth is also incorporated into the bottom layer of the assembly to limit strain. Without this strain-limiting element, the support structure of the arrays may balloon in unwanted ways. In the array overview shown in Figure 4.2, the channels are then fully closed and a small hole is cut in order to insert an air supply. In some layouts, however, the channels are left open from the molding process and are sealed with silicone glue (Silpoxy). Another overview that includes this step as well as more details of the other steps for creating large arrays can be seen in Figure 4.26.

4.7.1.3 Fabrication steps for Large Arrays

An overview of the process used to make a large rectangular array of actuators is shown in Figure 4.26. This process leverages modular mold pieces made out of laser-cut acrylic, making them cheap and fast to fabricate, and easy to reconfigure. The mold materials also do not require the use of mold release in the process. The primary mold parts consist of a bottom plate that controls the relative positioning of the pins that will be dip coated to form actuators and the acrylic rails that define the open channels that will later serve as pneumatic lines that connect to the actuators. The pieces of the mold are held together with press fit pins, which are the same pins as those used for the dip coating process. The press fit assembly allows the mold to be assembled and disassembled by hand or with a pair of needle nose pliers for every step of the molding process.

For the first step in making an array of actuators, the mold parts are pinned together, as shown in panels A and B of Figure 4.26. Panels C and D show the process of casting rubber spacers that will later be used to define the walls that separate pressure supply channels under the array of actuators. In this case, the spacer divides the array into sixteen rows that can be individually actuated. Each row can later be joined or kept pneumatically independent. These channels can also be redefined to group different zones or arrangements of actuators, without requiring a redesign of the mold. The spacers are created by first adding a retaining wall around the assembled mold parts and then pouring rubber into each of the gaps between the acrylic rails. In the example, a simple retaining

wall was made with masking tape attached to and overhanging the edge of the base plate of the mold. In the example shown, the rails are 3.15 mm tall and 7.5 mm wide and the rubber for the spacers is poured up to approximately the same height as the rails. Once the rubber has cured, the mold is pulled apart and the spacers separated and trimmed of excess rubber.

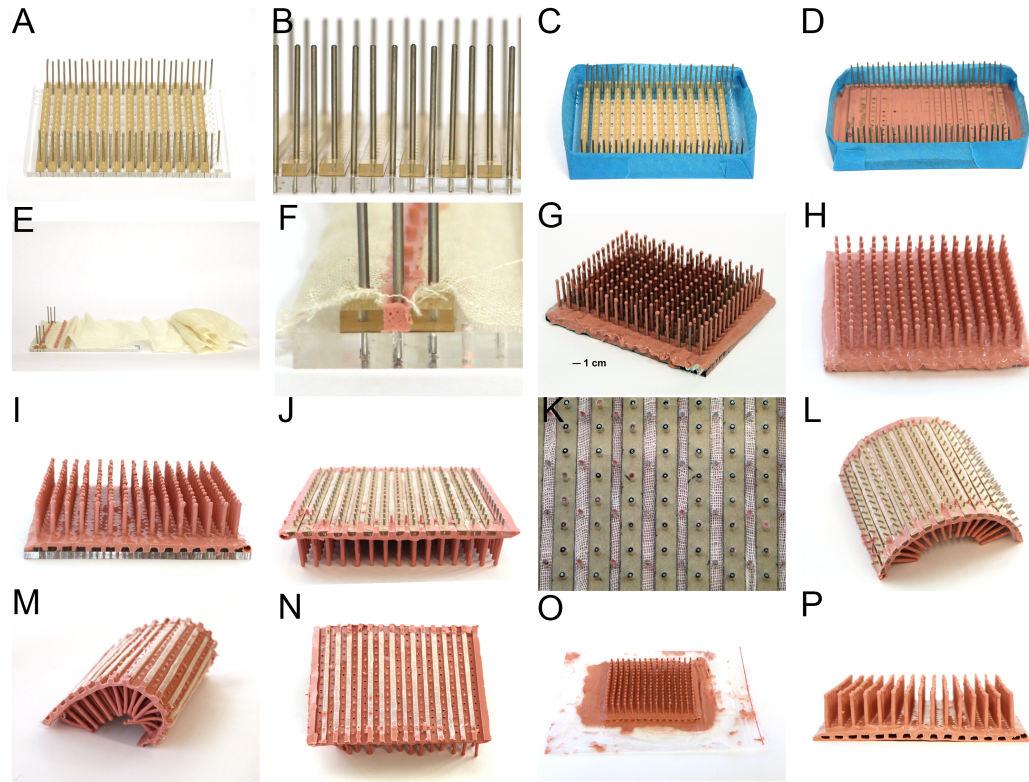


Figure 4.26: Overview of the fabrication process for actuator arrays. (A-B) The mold is pinned together, (C) masking tape is added, and (D) rubber is poured to form spacers. The mold is disassembled and (E-F) reassembled with cheesecloth weaving under the acrylic rails and over the rubber spacers. After coating the pin tips (G) a layer of rubber is poured over the top of the array, which is then cured at an angle. (H) Additional layers are poured over the mold and cured at an angle. (I) The array is trimmed and (J) the base plate of the mold form is removed. (K) The cheese cloth on the bottom has been intentionally kept clear of the rubber poured on top. (L-M) The acrylic rails are removed and (N) then the pins are removed. (O) The bottom is sealed by placing the array over a pool of rubber with a layer of cheesecloth. (P) The array is trimmed and ready for plumbing.

With the spacers cured and trimmed, the mold is then assembled again to prepare for the fabrication of the actuator array. In this process of assembling the mold, a strip of cheese cloth is woven up and down between the rails, spacers, and bottom plate of the

mold, as shown in panels E and F of Figure 4.26. The direction of the weave is important, with the cheese cloth wrapping about the acrylic rails and below the spacers. This wrapping direction allows the rails to later be removed from the bottom of the array, while the rubber spacers are incorporated into and remain in the final assembly. This cheesecloth layer may be omitted, depending on the desired size and arrangement of actuators, but is helpful in the example design for the purpose of strain limiting the air supply channels, which are not intended to expand, and anchoring successive layers of rubber. The strain limitation can be especially important where the pneumatic supply channels have greater internal surface area than the actuators. The air channels and strain limiting cheese cloth are indicated in the schematic of a nine-part array of actuators and cross-sections in Figure 4.27.

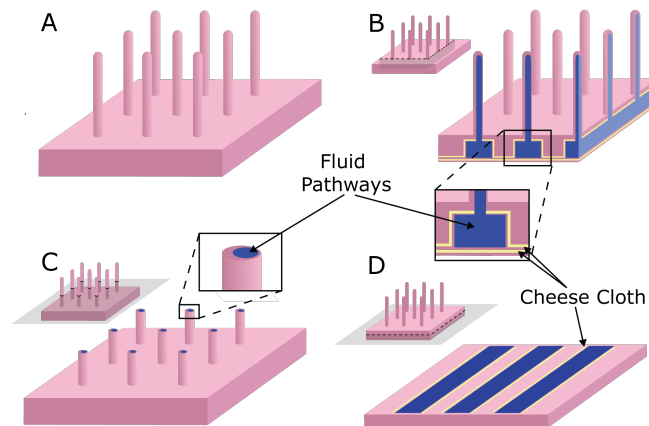


Figure 4.27: Schematic showing various cross sections of a nine-part array of actuators.

During mold assembly, the rubber spacers are slightly compressed to fit the added thickness of the cheese cloth. This compression helps to prevent rubber from flowing from the top surface of the array to the bottom surface by traveling between the spacers and rails. The cheese cloth on the top surface is integrated with the rubber that is poured over the pins to create the actuator array, while the bottom facing cheesecloth is kept clear of rubber. This result can be seen in panels J through N of Figure 4.26, where the bottom facing cheese cloth was preserved from the rubber that was poured over the mold assembly. Later, when the assembly is removed from the mold, these exposed portions of cheesecloth on the bottom are used to create a mechanical anchor into a new layer of rubber that forms the bottom of the pneumatic supply channels. Cured silicone is difficult to bond to, but the natural fiber

of the cheesecloth helps increase the surface area that incorporates with the new rubber for mechanical anchoring and distribution of forces. This mechanical bonding is not required for low operating pressures and can be accomplished with an adhesive treatment or plasma bonding. This strategy of mechanical incorporation, which is inspired by fiber reinforced soft actuators, requires some design and fabrication consideration but provides a useful and straightforward bonding alternative that is robust to high pressures.

As the cheese cloth, rails, and spacers are placed, the pins are pressed through the cheese cloth, into the rails and underlying bottom plate. Once all of the pins, rails, spacers, and cheesecloth are assembled, the tips of the array of pins are dipped in rubber. This is shown in Figure 4.2 of the main text. This tip dip is to prevent thin spots and is accomplished by pouring a puddle of rubber onto a flat surface so that the dip mold assembly can be turned over and all of the pins dipped simultaneously. The assembly remains oriented such that the freshly dipped pin tips are still facing downward until the rubber is cured and is no longer at risk of running down the sides of the pins. Once the tips have cured, the assembly is then turned right-side up again, back to the orientation shown in panels G and H of Figure 4.26. The assembly is then propped at an angle using a scaled up version of the fixtures in Figure 4.7. In the case of the large array demonstration shown in Figure 4.1E-H, the assembly was propped at a 30° angle for the dual purpose of using gravity to mechanically program the motion of the actuators under inflation and to allow runoff of excess rubber.

For the example array shown in Figure 4.1E-H, we poured three coatings of rubber over the pins to create the actuators. Prior to this, we also tried a version with two pourings but observed five small holes over 256 pins that had to be located and covered, and thus increased to three coatings to make the process more robust to small defects. Panel G of Figure 4.26 shows an array after one coating and Panel H shows an array after three coatings. In the coating process, it is important to get full coverage of all of the pins, however the coating is ultimately made uniform passively by gravity and surface tension forces. To ensure full coverage, we applied two passes of freshly mixed rubber over the array. To make this slightly easier and minimize waste, a collection tray and funnel of aluminum foil was placed under the mold to direct and concentrate flow into a cup that could then be poured back over the assembly. While pouring over the pins and recycling the collected runoff rubber, it is important to also keep in mind the working time of the rubber. Related to the working time, we limited each coating to two pour-over passes, completed

in approximately fifteen minutes or less. After much longer, the rubber starts to cure and increase in viscosity. The increased viscosity means that the flow is slower and cannot even out the thickness of the coating as readily, ultimately resulting in uneven coverage. Some of this effect can be seen in the nonuniform actuators in Figure 4.28.

Another effect that can be seen in Figure 4.28, other than the uneven coating from pouring rubber too far past its initial mix time, is the development of thin spots at the base of the actuators. In arrays that have otherwise been evenly formed (i.e., rubber is only poured shortly after mixing and is given time to even out to a uniform thickness), thin spots develop consistently at the base of the pin, on the higher side of the pin as they are oriented at an angle. The cause of the thin spots is a combination of gravity and surface tension pulling the rubber to the lower side of the pin and toward the pool of rubber along the floor of the array surface. These thin spots inflate before the rest of the actuators, causing them to lean over in a straight shape rather than curling over. With a further increase in pressure, if the thin spots do not pop, the rest of the actuator will then begin to curl. While this may be an interesting effect to exploit for the purpose of exploring more complex and non-linear deformations as a part of the mechanical motion programming strategy, we decided to counteract this behavior to simplify the design considerations and make a more robust array of actuators. Our solution to counteract this behavior involved pouring a final layer of rubber along the floor of the actuator array. While still in the angled setup used for the overall coatings, we started the pour at the base of the upper edge of the array and let it flow down the array, thus leaving the majority of the length of the actuators uncovered, but flowing over and coating the base of the actuators and thus covering the thin spots.

After the final coating of the actuator bases (to cover the thin spots) was fully cured, the arrays looked like the one shown in Figure 4.26H and the edges of the array assembly were trimmed with a pair of scissors or razor blade, using the edge of the base plate of the mold as a guide. A trimmed array is shown in Figure 4.26I. After trimming the edges, the base plate is removed, as shown in Figure 4.26J, revealing the rails and cheese cloth, which are shown up close in Figure 4.26K. It can be helpful to push the pins partially through the base plate with a spare pin to make removing the base plate easier. With the base plate removed, the array is flexible in one direction, but the rails still enforce some directional rigidity. Once the rails and pins are removed, the array looks like the pictures in Figure 4.26M and Figure 4.26N. The rails and pins can be removed in either order. A

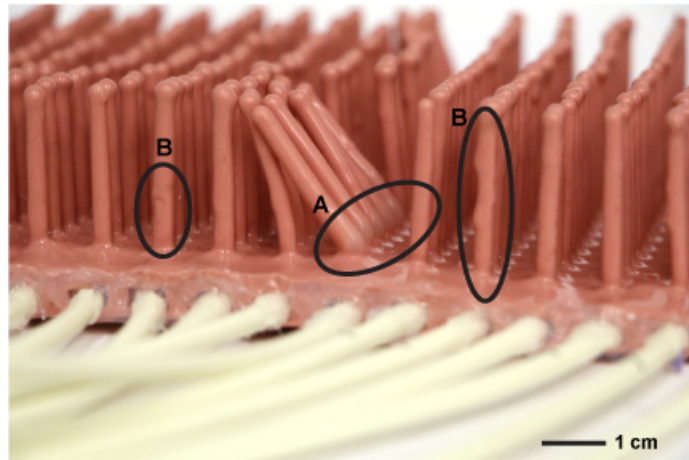


Figure 4.28: Photo showing area where arrays of dipped actuators develop a thin spot (A) and areas of uneven coating (B).

pair of needle nose pliers makes the pin removal much easier and care should be taken to not invert the actuators while removing the pins.

Once all parts of the mold have been removed, the bottom face of the air supply channels are then enclosed by pouring a puddle of freshly mixed rubber and then carefully placing the array assembly into the puddle to cure. The rubber is first poured onto a sheet of polyethylene (or another plastic film), which releases easily from the rubber without the use of any mold release. After pouring and spreading a layer of mixed rubber on the polyethylene sheet, a piece of cheese cloth was placed on top of the wet rubber. The cloth was pressed into the rubber, and then additional rubber was spread over the cheese cloth. Once the cloth is fully saturated, embedded in the rubber, evenly spread, and degassed, the array of actuators and the exposed cheese cloth on the bottom of the array was carefully pressed into the wet rubber. Care should be taken to press the array down enough to help the cheese cloth woven into the bottom of the array to soak up and incorporate the new rubber, but not press so much that the new rubber plugs the air supply channel or the holes that lead to the inlets of the actuators.

Once the bottom layer is fully cured, the assembly can be pulled off of the polyethylene sheet and again trimmed to the previously defined edges. The holes on the side of the air supply channels, like the ones visible in Figure 4.26P, can then be plugged on one side with silicone glue, such as Silpoxy (Smooth-On). Inlet tubes can then be inserted on the remaining open end. For this, we used silicone tubing with a 3mm inner diameter, (Boxer

Pumps, model 9000508). We first applied glue around the outer rim of the tubing, inserted the tubing into the end of the air supply channel of the array and then smeared the glue around the outer edge of the connection with a cotton swab to roughly create a filleted geometry, adding glue if necessary to fill any holes. The tubing sizing can be reduced and the resulting gaps filled with additional glue, or the pressure supply channel hole size can be reduced by adjusting the size of the mold rails. Similarly, to increase the tubing size, one can increase the size of the molding rails to thus increase the size of the pressure supply channels. An example of polyurethane tubes plumbed into the end of the air supply channels is shown in Figure 4.28. The polyurethane tubing connections were less able to bond to the Silpoxy and we therefore switched to the silicone tubing in later array iterations. These are intended to be makeshift connections for actuator testing. A cleaner pneumatic connection can be made by fully sealing the supply channels, punching connection holes in the side wall with a biopsy punch, and inserting a barbed tube fitting.

4.7.2 Fixture and pouring modifications for long actuators

For the fabrication of actuators longer than a few centimeters, including the one shown in Figure 4.4, we adjusted the process to minimize the amount of rubber and size of the container needed to dip coat a pin. This slightly modified process was used to form the ‘filament’ actuators described in the following chapter. By cutting a hole in the bottom of a small cup, we can dip coat an arbitrarily long pin. The cup is held at the top of the pin with the pin passing through the hole, partially filling the cup with newly mixed rubber, and then pulled down the length of the pin. To facilitate this, the pins were suspended from above with a fixture designed to hold the pin at the desired angle. Pulling the cup down rather than up the length of the pin is helpful in making the process relatively insensitive to the size and position of the hole because the pin exits through the meniscus at the top of the vessel instead of through the hole at the bottom. The hole needs to be large enough to allow the pin to pass freely and small enough that the rubber does not pour out quickly, though some rubber leakage is tolerable. Having the cup lightly touching the pin while pulling up would be problematic in that it would scrape rubber from the side of the pin, while pulling down ensures that there is full coverage. Care should be taken so the cup is not tilted such that the upper lip can scrape the freshly coated pin. Because the cup can also be refilled during this downward pull, this can effectively act as an infinitely deep vessel

for dip coating pins of arbitrary length. For parallel fabrication of long actuators, a shallow laser-cut tray with multiple holes and a retaining wall was used as a liquid rubber vessel. With this “infinite dipping vessel,” the primary limitations on the length of actuators will be the available space and encumbrance of working with large rods that are difficult to maneuver, the sag in the rod when tilted over a longer distance creating a variation in the tilt angle, and the mix viscosity and cure time of the rubber limiting the ability of the rubber to flow and fine out to an even coating.

4.7.3 Two degree of freedom actuators

All of the actuator variants presented above have one DOF (degree of freedom) of motion but the dip-coating process can also be modified to create tri-chambered pneumatic bending actuators [113] capable of two DOF of motion. Using the same pins and materials described above, the pins can be press-fit into an open-face mold assembly in sets of three, as shown in Figure 4.29. When the three pins are sufficiently close together, liquid rubber bridges between the three pins. When the pins are removed, the result is three individually addressable pneumatic chambers that are coupled in a single soft actuator body. Because each chamber is offset from the neutral axis of the actuator, pressurizing any one chamber produces a moment which causes the actuator to bend. By modulating the pressure in each chamber, the actuator can bend in any radial direction. An example of a 2DOF actuator and the cross-section is shown in Figure 4.30

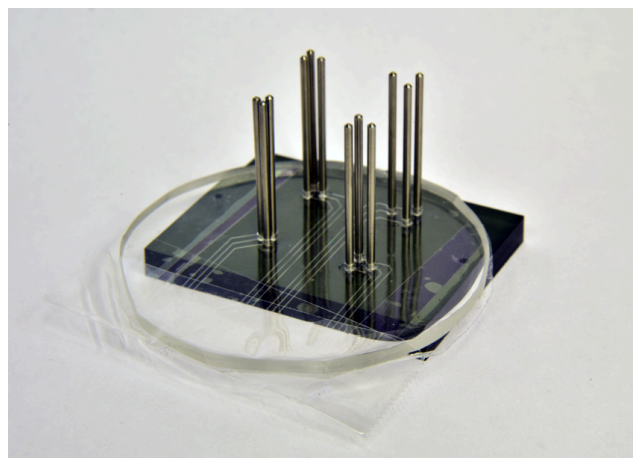


Figure 4.29: Pins for dip molding 2DOF actuators pressed through the elastomer with microfluidic components, and into an alignment fixture.

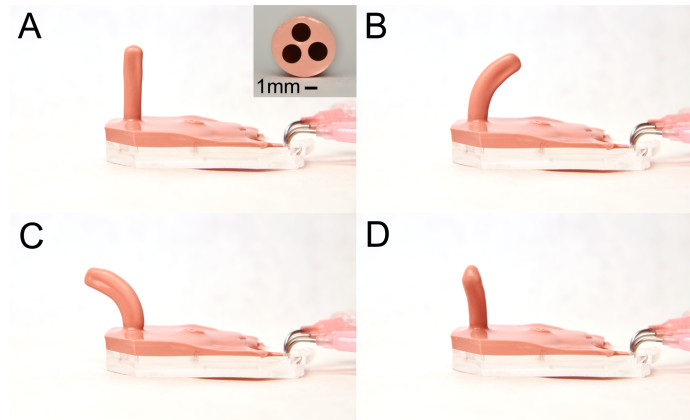


Figure 4.30: Photos of a 2-DOF dip molded actuator (A) in a rest state with and inset of the cross-section of an actuator and (B-D) with three of the separate chambers actuated.

The spacing between the three pins is an important variable to consider when designing tri-chambered actuators for dip-coating. Tighter spacing leverages surface tension to counter gravity forces and holds rubber between the pins as it cures. The rubber trapped between the pins bridges the walls of the three chambers together into a single tri-chambered actuator. When the sets of pins are more closely spaced, fewer dips are needed to completely cover and connect the pin triplets. However, tighter spacing also increases the likelihood of cross-talk or leaking between chambers. Leaking between chambers is most often caused by a bubble trapped between the pin upon dip coating. Wider spacing between pins, conversely, minimizes the likelihood of leaking but the larger central gap creates wider overall actuators, which are stiffer and thus more difficult to bend. The larger gap also requires more dips to fill, resulting in thicker chamber walls that demand a higher pressure to induce bending. A 3 mm center-to-center spacing of pins prevents cross-talk failure modes while maintaining low actuation pressures (approximately $90kPa$), which was desirable for the integration with a fluidic control system, such as a microfluidic de-multiplexer, described further in Section 4.7.4 below. The design and fabrication of the demultiplexer was developed by Nicholas Bartlett [114]

Similar to the steps for the one-DOF actuators above, the tips of the pins were dipped into liquid rubber and then hung upside-down to cure. Because the tri-chamber serves the purpose of motion programming, the pins were dip coated without any of the mechanical programming modifications described above. The first dip coating resulted in pins that were coated but not bridged. Cotton twine (McMaster-Carr PN1929T12) soaked

in liquid rubber was then inserted between the sets of pins, ensuring that liquid rubber wetted to the interior edge of each pin to avoid gaps. The cotton twine was allowed to cure again with the pins pointing upward. A final dip was added over all of the pins and left to cure with the pins pointing downward. The twine served two purposes, creating a strain-limiting core in the tri-chamber structure and helping to fill and bridge the gap between the pins.

The actuators can be made without inserting fibers in the central axis. Additional layers of dip-coating can be added with a combination of upright and hanging curing orientations. Hanging cure steps are useful for bridging without fibers. Connecting the pin tips with rubber in the initial tip coating step or adding paper or fiber to prematurely bridge the tip can also help bridge the rest of the internal gap in successive dips but was observed to also increase the risk of trapping bubbles between the pins. The advantage of including fibers in the central axis of the actuators is that bubbles are less likely to occur if done carefully and it is less problematic when bubbles do occur.

4.7.4 Integration with microfluidic control

With large arrays of soft actuators, the need for compact and integrated control becomes more pressing. The 2-DOF actuators described in Section 4.7.3 demonstrate how this need can be exacerbated if each actuator in an array requires multiple inputs. A solution developed by Nicholas Bartlett to help address this need is a microfluidic demultiplexer, a device capable using two static pressure lines and n high/low input pressure lines to address 2^n output pressure lines. As a demonstration of the demultiplexer and 2-DOF dip molded actuators, we created an integrated system of a demultiplexer with four logic input lines to drive an array of five 2-DOF actuators, which can be seen in Figure 4.31. Because the actuators only required 15 pressure inputs, one output of the demultiplexer was left unused. Details of the demultiplexer development can be found in the original paper [114] and a brief description of the related modification to the dip molding process to facilitate integration with the microfluidic controls is below.

The first consideration in integrating the demultiplexer with an array of actuators was to tune the operating pressure of the two subsystems. This is a key consideration in the integration with all microfluidic circuits and soft actuators. By changing the number of layers added, we have been able to make the 1-DOF dip-coated actuators functional over an

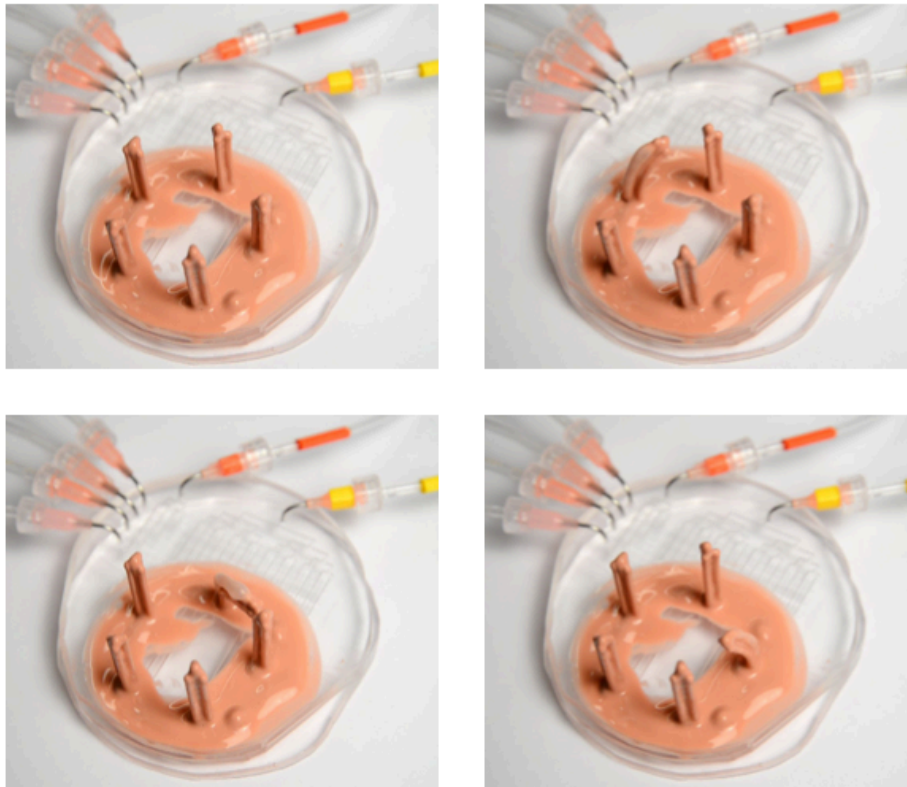


Figure 4.31: Photos of an integrated system with a four (variable) input, 16 output demultiplexer couple to five tri-chambered actuators arranged at the vertices of a pentagon. The stem is shown at rest and in three modes of actuation. Only 15 of the available 16 outputs from the demultiplexer are used by the actuators.

operational pressure range of 7 to 344 kPa. The microfluidic logic and fabrication are more robust at lower pressure. On the other hand, the tri-chamber actuators exhibit a trade-off in that fewer coatings during fabrication enable a lower actuation pressures, but also pose a higher risk of failure due to a defect in a thin chamber wall. In a large array in which a single failed actuator would compromise the entire system, we prioritized robustness over a lower operating pressure. We determined the minimum required actuation pressure to be 90 kPa, which we accomplished with two dip coatings.

After picking an appropriate operating pressure, which was aided by the characterization in Section 4.6.1, relatively few modifications to the two fabrication procedures were necessary to integrate the two halves of the system. Coupling points appropriately spaced to create vias to the pins were designed into the microfluidic circuit. Holes for the vias

were punched manually with a 14-gauge needle with the aid of an acrylic alignment fixture wetted to the top of the elastomer. After removing the punching aid, the stainless steel pins were pressed through the holes in the elastomer and into a second acrylic fixture underneath the elastomer as shown in Figure 4.29. This helped to rigidly constrain the pin with a 3 mm center to center spacing perpendicular to the circuit surface. Packing tape was applied to areas that needed to be kept clear of errant rubber in the dipping process. Dip coating then followed the process outlined in Section 4.7.3. We ensured the surface of the demultiplexer was kept clean prior to the dipping process but no other step was necessary to achieve a sufficient bond between the two elastomers used at the chosen working pressure (90kPa). If necessary, a strategy of mechanical reinforcement like the approaches described in Sections 4.7.1.2 could be incorporated into the process to support higher operating pressures. After the dip-coating process was completed and the rubber was cured on the pins and the top surface of the elastomer, the pins were removed through the bottom of the vias. The exit holes were then sealed by plasma bonding an additional layer of elastomer over the bottom of the assembly.

4.8 Conclusion

This chapter describes a fabrication strategy for using open-faced molds to create large arrays of dip-molded high aspect ratio soft actuators. It also describes four ways to modify those structures in the forming process in order to intentionally bias molding thicknesses or incorporate strain-limiting fibers. The thickness bias and fibers are then leveraged to mechanically program these soft structures to function as pneumatic bending actuators. Depending on the strategy chosen, actuators fabricated in integrated arrays may all bend in the same direction or can be prescribed an arbitrary vector field of bending directions. For more direct control of bending direction, methods for creating tri-chambered 2-DOF actuators are also presented along with the integration with microfluidic circuitry. Compatibility between the dip-molding process and microfluidic fabrication methods helps to address the need to reduce the bulkiness of control lines when driving individual fluidic actuators in large arrays. The achievement of long individual actuators as well as large integrated arrays of actuators is facilitated by the simplicity, low precision requirements, and low cost of the open face molding techniques that we present. We demonstrate a 1 m long actuator, as well as a 256-part array but believe that these processes could produce

longer actuators and larger arrays, if desirable. The use of laser cut acrylic mold parts also allows for rapid generation and iteration of mold designs at low cost. The designs can also be created and edited as relatively simple, two-dimensional designs in vector graphics software.

Future work with these fabrication methods could include exploring strategic actuation patterns or vector fields of bending motion direction mapped into large arrays of these actuators for the purpose of fluid manipulation, object manipulation, gentle grasping, and locomotion. A continuation of this work would also include the combination of multiple mechanical programming strategies in a single array or varying the parameters over the length of the pin to create purposeful variation in the bending profile. The programming methods utilizing surface tension and electric fields in particular may have a relatively low increase in manufacturing complexity to program variations in the bending profile over the height of the finished actuator. The pin cross section and proximity of electrodes could be varied along the length of the pin. Potential areas of exploration for the electric field strategy more specifically might also include placement of arrays of pins to intentionally affect the resulting electric field that biases the actuator thickness. The charging setup could also be modified to incorporate multiple charge states, such that the dipping mold could be segmented into different charge patterns that cycle at a frequency that allows two or more distinct electric fields to affect subsets of the forming actuators. More broadly, the open face molding strategies can also be further developed to incorporate these arrays onto non-flat architectures as well as underlying functional structures that might allow for active morphology changes, such as an array of grasping cilia built onto a soft hand or tentacle designed to securely and gently pick up items.

Chapter 5

Entanglement Grasping

5.1 Introduction

Leveraging the material and structural compliance of the high aspect ratio soft actuator arrays presented in the previous chapter, it is possible to achieve robotic grasps composed of distributed contacts. In this chapter, I present a novel grasping strategy, *entanglement grasping*, that uses the collective entanglement of an array of actuated high aspect ratio actuators called *filaments*. This collective entanglement can be used to create a grasp that is gentle, strong, and adaptive to object topology. An example gripper composed of twelve filaments is shown in Figure 5.1. As described in the previous Chapter, and depicted in Figure 5.2, the individual filaments curl when fluidically actuated. Upon actuation, the filaments randomly entangle with each other and with a target object to create a soft conformable grasp. This stochastic application of distributed contacts is a departure from most deterministic, feedback-driven grasping solutions. This stochastic strategy also excels in gripping complex and compliant topologies for which traditional grasp planning and execution is challenging due to visual and structural complexity. Through experimental demonstrations, I show that this intentionally unstructured collective of contacts is capable of adaptive grasps without any perception, planning, or feedback. Using a custom tool built to simulate the collective mechanics of filaments in contact with complex objects, I explore the design space of the filament-based entanglement grippers. I also show the capacity of this collective entanglement-based strategy to apply gentle yet robust grasps in scenarios that would challenge traditional grippers, from lifting a potted plant by entangling with its complex arrangements of shoots and leaves, to lifting a sea star from the ocean floor.

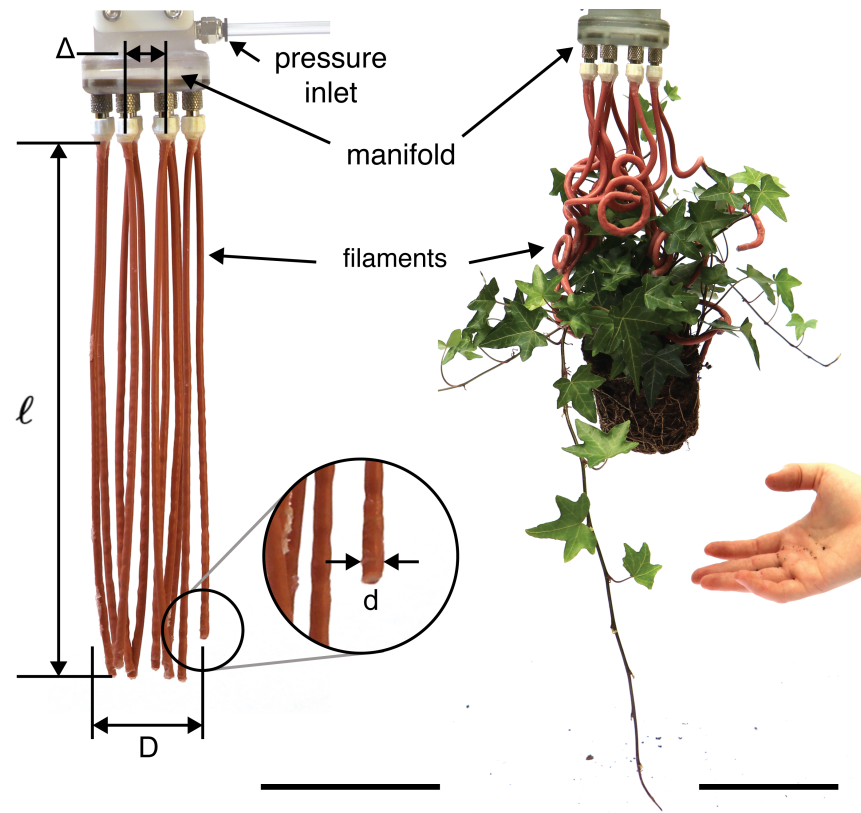


Figure 5.1: A) Picture of an entangling filament gripper consisting of 12 hollow elastomeric filaments in a resting state and pneumatically actuated around a house plant. The scale bar represents 10cm.

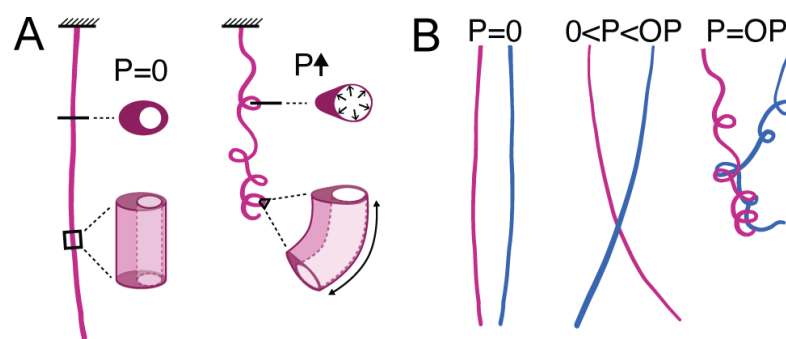


Figure 5.2: A) Schematic of filaments and section of filaments at ambient and increased internal pressure. B) Schematic of filaments intertwining. Filaments start mostly straight when hanging under gravity, develop a slight curve at low pressure, and then snap to a tightly curled shape close to the operating pressure (OP). The operating pressure for the filaments shown in this work is approximately 25psi (172 kPa).

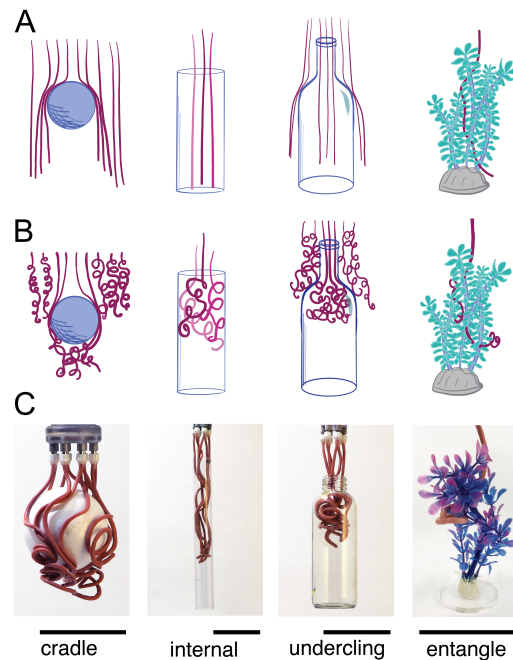


Figure 5.3: The final shape of the actuated filaments and resulting grasp is affected by object interactions. The schematic shows (A) unactuated and (B) actuated states in the presence of a sphere, tube, bottle, and artificial plant. (C) The photos show examples of physical tests corresponding to the objects depicted in the schematics.

The collective behavior of a large number of curling and twisting filaments allows them to entangle with a target and thus drape, cradle, or conform to it as a function of the actuation pressure, as shown in Figure 5.3. This further enhances the ability of an actuated array to grasp complex objects without perception, planning, or feedback, as a passive consequence of their geometrically-defined collective compliance. A schematic and a physical realization of how an array of such filaments interacts with different objects is shown in Figure 5.3. The filaments can engage on, around, and in a range of target objects such as spheres, cylinders, and corals, and can grasp them via collective entanglement. The numerous interactions are highly compliant individually, but capable of substantial stiffness collectively. This effect is not unlike tangled hair that is stronger than an individual strand [115]. The simplest grasps, as with the sphere, bear some resemblance to traditional grasping [116], whereas higher degrees of entanglement represent a larger departure from traditional grasping. Entanglement excels in grasping topologically complex, compliant, and often delicate structures ranging from common house plants to deep-sea corals, but can also be used to grasp common household items such as bottles, tubes, tools, and toys.

5.2 Background and prior art

Grasping an object securely typically requires some knowledge of its size, shape, and mechanical properties. Historically, a large effort in robotic grasping has focused on understanding the mechanics, dynamics, and control of grippers as they interact with target objects [116, 117]. One common approach is to study how the form and stiffness of the grasper (relative to that of the target) determines the number (topology), shape (geometry), and magnitude (mechanics) of contacts and associated stresses, while also improving sensing and perception of the target [118, 119]. This has been implemented in both a hand-centric design paradigm [117], as well as more simplistic gripper morphology [39]. In either family of gripper designs, there is typically a high reliance on an opto-motor feedback loop linking perception, planning, and action to achieve a grasping goal. Modern rigid grippers show great promise with many controllable degrees of freedom and embedded sensors [120, 121, 122, 123, 124], but can present challenges for grasp planning and control in the presence of uncertainty, or with complex target geometries [125, 4].

More recently, the introduction of compliant elements and under-actuated control into otherwise-rigid fingers provides a form of embodied intelligence that drastically reduces the planning and control requirements for successful grasping. These graspers are exemplified by having a small number of degrees of freedom associated with the distal portions and a series of proximal joints that are soft and can thus allow increased adaptability of contact configurations with the target [126, 127, 128, 129, 130]. This concept of strategic compliance is further extended in fully-soft robotic digits, utilizing soft materials throughout the entire digit structure to enable them to conform to a wider variety of objects [42, 19, 108, 43, 131, 132, 41]. Fully soft graspers circumvent precise feedback control and instead rely on mechanical deformation, both distally and proximally, to passively adapt to target objects. Some of the mechanical complexity of a grasping task is thus resolved by morphology where passive mechanics and dynamics leads to conformable contact. Even in the absence of feedback, these soft grippers are thus adaptable and robust to a range of variations in the target shape, size, and properties [1, 47, 133]. However, even with integrated compliance, these same soft grippers typically still rely on relatively few digits (three, four, or five), and few regions of contact. This still leaves open the question of how to grasp objects that are geometrically and topologically complex, and mechanically heterogeneous, e.g. plants, produce, fragile marine fauna, or many human-made devices.

While soft gripper materials allow compliant interactions with target objects, the structural compliance of high aspect ratio actuators like the filaments introduce geometrical and mechanical flexibility. Applying both material and structural compliance allows a soft actuator to achieve greater engagement with and topological conformation to target objects. The basic building block of this strategy is a slender elastomeric filament with an eccentric hole running axially (sealed at one end). Filaments are made using the dip-coating technique [134] described in the previous chapter. These filaments are similar to, but much larger than, recently developed micro-tentacles [102], and also operate in a manner similar to plant tendrils [135] and tendril inspired robots [106], but are much faster owing to the rapidity of pneumatic actuation relative to growth or shrinkage driven tendrils and tendril-robots. Sinatra et al.'s nanofiber programmed fingers [99, 132] may be the closest relative soft robotic fingers given their high aspect ratios and highly compliant grasp strategies, but those efforts still aim to mimic a traditionally configured palm.

The key capabilities that make our gripping platform well suited for entanglement grasping stem from our actuator fabrication method. Our dip molding methods allow for easy and uniform construction of large array of actuators with a high aspect ratio for compliance, sufficient length for intertwining and engaging with target objects, and a sufficiently high actuation bandwidth for grasping tasks. The large arrays are particularly important in allowing for random contacts and the graceful degradation to failure of an individual filament. Our dip molding methods (see Chapter 4) allow for cheap, easy, and uniform construction of large arrays of actuators with a high aspect ratio (up to 200:1). The configuration shown in Figure 5.1 and used in the experiments below uses 12 300mm long filaments distributed in a 50mm diameter circle and connected to a single pressure source, but this design can easily be modified. When an individual filament is pneumatically or hydraulically actuated, it bends because of the eccentricity of the hole, as shown in Figure 5.2. This enables an individual filament to hang straight down under ambient pressure, form a slight curve and approach nearby filaments at low pressures, and then snap into a high curvature state to form soft distributed contact zones either with a target object, itself or other filaments as it reaches its operational pressure, as shown in Figure 5.2. The operating pressure can be tuned via fabrication methods described in the previous chapter and is set to 25psi (172 kPa) in this application.

Applying collective arrays of compliant, adaptive, and tangling filaments to a target object, we can rely on stochastic interactions to create a robust grasp in the absence

of perception, planning, or feedback control. In this way, our grasping strategy resembles that of tentaculate entangling predator behavior of many medusae, siphonophorae, and ctenophorae [136]. With entanglement grasping, we propose the next paradigm shift in the design of robotic grasping devices toward utilizing “strategic randomness” and a combination of both material and structural compliance. The entanglement grasping strategy we present in this work is based on larger arrays of soft high aspect ratio “digits” (filaments) engaged in non-deterministic motion. As a result, the contact interactions are intentionally random, relying on the quantity and compliance of the filaments to achieve a stable grasp. While we do not anticipate entanglement replacing traditional rigid or soft robotic grasping, it extends the variety of objects that can be successfully manipulated via robotic grasping. Traditional grippers are better at grasping simple objects like spheres and cubes, while the strategic randomness of entanglement grippers are better suited for topologically complex objects. This intentional randomness makes the entanglement strategy less sensitive to noise or the demands of path planning for computationally difficult or demanding scenarios or objects.

5.3 Evaluation of entanglement strategy: physical testing

We evaluated the performance of entanglement grasping using a task-based experimental and simulation approach. Analytical frameworks used to understand and plan grasps such as form and force closure, and contact curvature analysis become intractable with the large degree of randomness in contact interactions that entanglement relies upon. Furthermore, our strategy suggests that the notion of force closure used in deterministic grasping [118, 137] may be less relevant to entanglement and should be revisited in a probabilistic setting. In addition, the notion of static equilibrium that is necessary for stable grasping is very different for simple contacts typical of deterministic grasping compared to the present case of redundant soft distributed contacts. Experimental (Section 5.3) and simulation (Section 5.4) based evaluations allow for comparison with similar experimental studies used to evaluate traditional grippers. In defining an appropriate task, we use the common definition of a stable grasp: A grasp is statically-stable if the grasped object is in static equilibrium. Additionally, a common practical definition of grasp success during a manipulation task is used as a proxy for grasp stability since the actual force balance is intractable to measure in hardware: A grasp is successful if the target object is able to

be moved from its initial position to a desired location without being dropped. Using this evaluation framework, we explored the effects on grasp success rates when varying approach strategies, target object topology, and position offsets between the gripper and target object during the grasp sequence.

5.3.1 Object set for grasp testing

The object set used for the experimental testing in this study is shown in Figure 5.4 and the object masses, materials, and characteristic dimensions are listed in Table 5.1. The tubes and sphere were selected to represent a few variants on simple geometric primitives similar to the YCB object set [138]. The torus and branched structures were included to introduce a set of objects for testing that are more topologically complex. The simple branched structures are more complex than the objects in the YCB object set but simple enough to be reproduced on widely available FDM printers and simple enough to be implemented in simulations without high computational cost. Dimensions for the branched structures are shown in Figure 5.5.

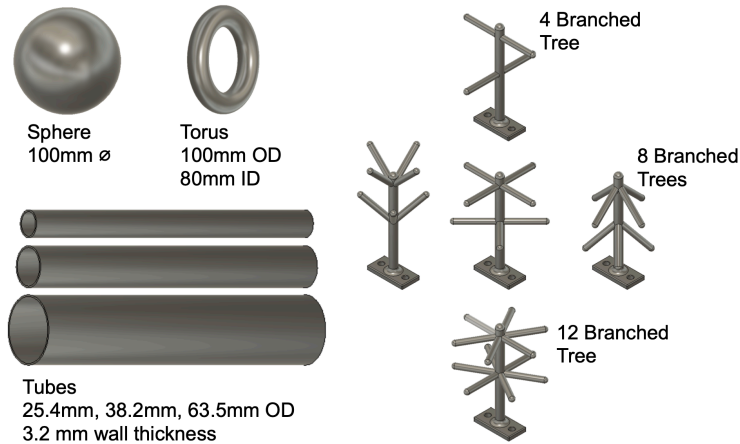


Figure 5.4: Set of target objects used in testing. The dimensions and weights of the objects are listed in Table 5.1. Not shown are the Aluminum bars that were attached to the bottom of the tree structures for adding weight for the robot arm grasp tests. These aluminum bars are visible in Figure 5.6.

Within the set of simple branched structures, “trees”, used for testing, we explored the effect of two geometric parameters, branch angle and branch number, on grasping success with the entanglement grasping strategy. The number of branches (distributed

Table 5.1: Physical properties of the objects used in this study

Object	Dimensions (mm)	Mass (g)	Material
Sphere	100 diameter	10	Styrofoam
Tube	25 OD \times 300 length	43	Polycarbonate
Tube	25 OD \times 300 length	91	Polycarbonate
Tube	64 OD \times 300 length	130	Polycarbonate
Torus	80 ID \times 100 OD	69	PLA (3D printed)
Tree (8 branches, 45 deg)	80 width \times 120 height	147	PLA + aluminum base
Tree (8 branches, 90 deg)	100 width \times 100 height	148	PLA + aluminum base
Tree (8 branches, 135 deg)	80 width \times 120 height	147	PLA + aluminum base
Tree (4 branches, 90 deg)	100 width \times 120 height	144	PLA + aluminum base
Tree (12 branches, 90 deg)	100 width \times 120 height	153	PLA + aluminum base

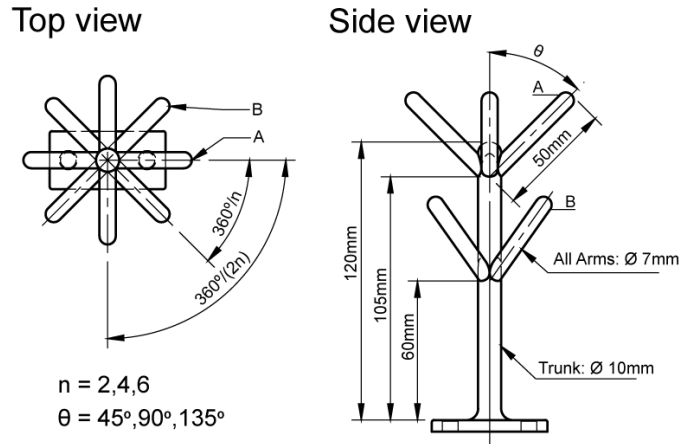


Figure 5.5: Dimensions for one of the branched structures. The number and angle of the branches changes for the other structures while all other dimensions are held constant.

evenly between two rings on the trunk) and the angle between branches and the trunk were varied as shown in Figure 5.4 and Table 5.1. The other characteristic dimensions were held constant, including the trunk height of 120 mm, trunk diameter of 10 mm, branch diameter of 7 mm, and location of branching points at 60 mm and 105 mm (from the bottom of trunk to the bottom of the branches).

5.3.2 Evaluation of approach strategies

We evaluate the efficacy of a grasp minimally in terms of successfully lifting and moving an object from its initial to its final position and begin by varying the initial approach and interaction with a target of varying complexity. For trajectories, we tried draping

from the top (“top-drape”), draping from the side (“side-drape”), and dropping from the top (“plop”), as shown in Figure 5.6. A top-drape approach was a slow lowering of the filaments onto the object and then actuation occurs, in a side-drape approach the filaments were lowered next to the object and then horizontally translated in the direction of the object to 50 mm past the center point of the object, and in a plop-on-top approach the filaments were first actuated above the object before being lowered to the intended grasp height and then released to fall around the object and actuated again for a grasp. These strategies were tested using a robot arm (UR5e, Universal Robots) on a sphere, a hollow cylinder, a torus, and two tree variants, as shown in Figure 5.7. The robot arm attempted five grasp trials per strategy and object, with each object centered on a table below the gripper. The resulting success rates are shown in Figure 5.7.

Overall, the top-drape approach strategy had the highest success rate for both simple and complex objects, whereas all other approach strategies failed to grasp the three simplest objects. The side-drape did, however, outperform the other two trajectories in grasping the simple branched structures and could potentially compensate for centering errors.

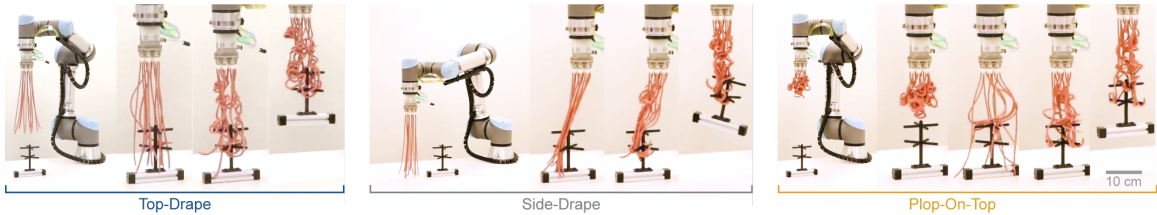


Figure 5.6: Three heuristic grasping approach trajectories used for evaluating entanglement grasping success rates. Pick-and-place operations with each of the three approach trajectories are shown, where the object’s initial pose remains constant for all tests.

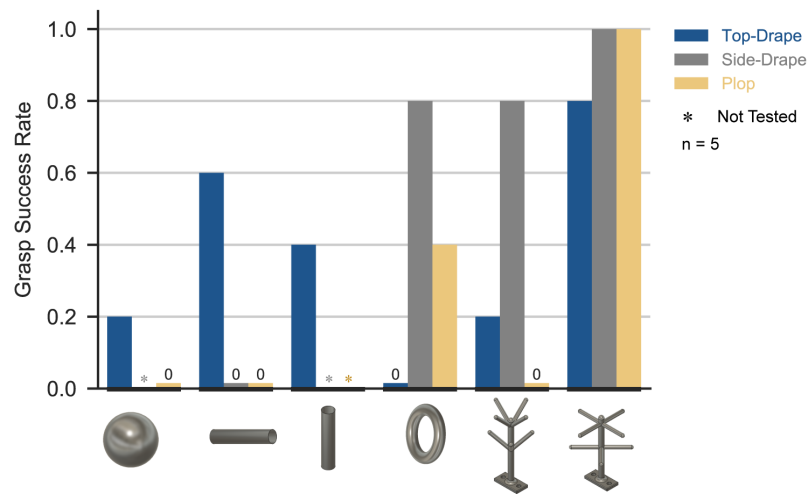


Figure 5.7: Grasp success rate with objects centered beneath the gripper. Grasps on morphologically complex objects are most successful, particularly with a side-drape grasp. Conversely, the gripper has a lower success rate when attempting to grasp simple objects, with only a top-drape producing successful grasps for the three simplest objects.

The same three grasping approaches were applied to each of the tree variants described in Section 5.3.1. As can be seen in Figure 5.8, the side-drape approach strategy gave the highest performance for all branched structures, with 100% grasp success rate for all but the eight-branched tree with a 45 deg branch angle. The top-drape achieved higher performance for objects with more branches. The plop-on-top approach worked well for the tree with eight branches and branch angle of 90 deg, but performance dropped off as both number of branches and angle of branches changed, up or down.

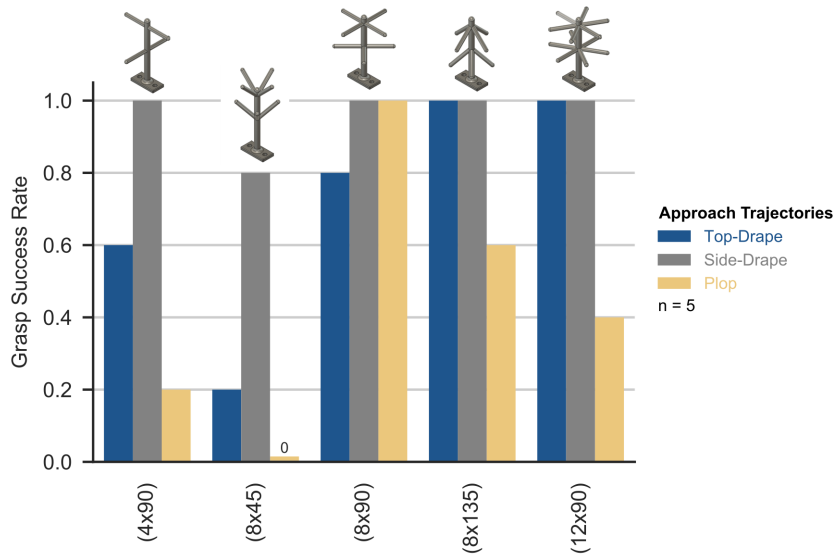


Figure 5.8: Three heuristic grasping approach trajectories were evaluated on the set of branched objects using the same procedures as for the tests represented in Figure 5.7

Another influential variable for future study is the height of the gripper at the point of actuation. Most of the robot arm mounted tests were performed with the tips of the filaments approximately aligned with the surface of the table. Shown in Figure 5.9 and Figure 5.13, however, is another set of data taken from a physical centering test where the filaments were lowered -80mm below the point where they touched the table. This produced a significant increase in performance, where the grippers were able to retrieve the tree some portion of the time up to 50mm away from the center position (100% of the object radius). Some of the performance increase may be explained by the fact that, upon hitting the table, the filaments can splay outward, effectively extending their horizontal reach.

5.3.3 Work space and sensitivity to position error

Using the top-drape as the most broadly-successful method of approach, we evaluated the entanglement gripper’s sensitivity to positioning errors following the methods used by Aukes et al. [139] and Sinatra et al. [132]. Using a subset of objects (a sphere, cylinder, and branched structure), we performed grasps with controlled centering offsets in increments of 10mm, and measured the resulting grasp success rate over five trials at each location. The results of these experiments are shown in Figure 5.9, as a function of the offset between the center axis of the gripper and the center axis of the target object (normalized to the object radius). Overall, we found that complex objects are tolerant to large centering errors. Our empirical investigation of grasping performance using non-deterministic entanglement is particularly successful in grasping topologically and geometrically complex objects [125, 4] without the need for planning, but has trouble with simpler objects like spheres and vertical tubes where traditional deterministic grippers work well, e.g., the YCB object set of generally cylindrical, spherical, and cuboidal targets [138].

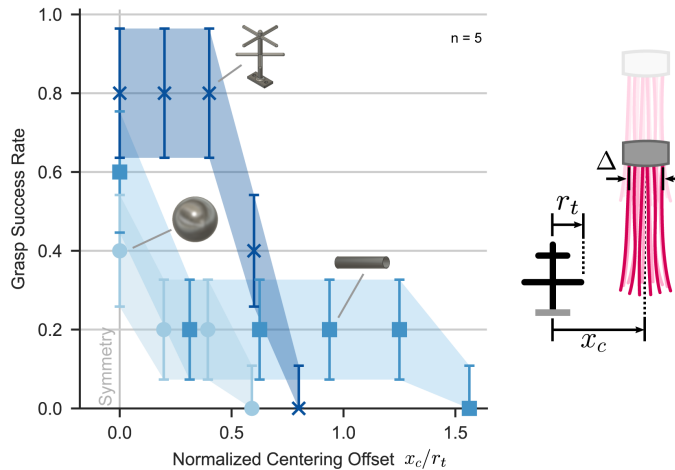


Figure 5.9: Grasp success rate test of the top drape approach with increasing centering offsets between the gripper and target objects. Offsets are normalized to the object dimensions. Top-drape grasps on complex objects are robust to centering errors up to $0.5\times$ the object diameter.

5.3.4 Grip strength

To characterize the strength of our gripper in the top-drape mode, we attached an object rigidly to the frame of an Instron universal testing machine and measured the

gripper force or entanglement force opposing object pull-out. Pictures of the test setup with a subset of the objects tested are shown in figure 5.10, along with plots of the raw force versus extension data. Only top drape approaches were performed because of the configuration limitations of the testing frame. The objects were also rigidly anchored, which was not true in the grasp success trials with the robot arm but the rigid anchoring provided a benchmark of the grip strength and a quantitative measurement to compare with simulation results. For the same gripper with 12 filaments and an operating pressure of 25psi (172kPa), the force-displacement curve was measured. We found that the maximum grasping forces achieved over the various objects was 27.6N , which is comparable to many robotic hands with soft, pneumatic fingers operating at similar pressures (e.g., in [19, 42, 108, 43, 40]). A summary of the average maximum gripping values observed from each trial as well as the maximum observed values across all trials is summarized in Figure 5.11. The examples of the trial sets from which these values are derived, shown in Figure 5.10, include the branched structure with eight limbs, the 63.5 mm diameter horizontal tube, the 25.4 mm diameter vertical tube, and the 63.5 mm diameter vertical tube.

As one might expect, the maximal gripping force achieved by the filament gripper was highly affected by the target object. Furthermore, the shape of the force versus extension curves shown in Figure 5.10 reflects the nature of the engagement between the filaments and the object. For example, the filaments predominantly rely on friction to hold the vertical tubes. As the object is pulled from the gripper, the forces in Figure 5.10C and Figure 5.10D are relatively level and show the friction forces as the object slides through the grasp of the filaments. By contrast, the trials from the branched structure in figure 5.10A and horizontal tube in Figure 5.10B appear to have a larger degree of variation that related to how many of the filaments wrapped around the tube or branches. There are also larger jumps in the data as individual filaments are pulled away and forced to release the object.

Using the shape of the data to discover information about an object may be an interesting direction for future study with entanglement grasping platforms. An example that could be investigated in greater depth is a slight upward trend in the data from the 25.4 mm tube and a slight downward trend in the data of the 63.5 mm tube, which may possibly be explained by the way in which the filaments engage with the two objects. The testing setup associated with these two trial sets is shown in Figure 5.10D and Figure 5.10C. As shown in the pictures, the filaments were draped around the outside of the 25.4 mm tube

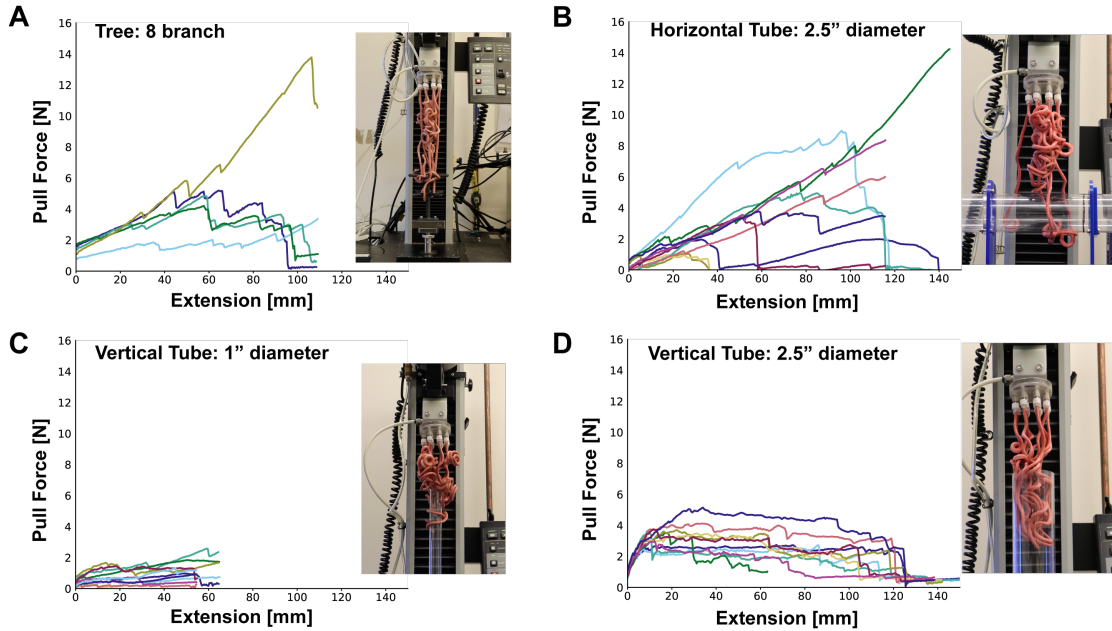


Figure 5.10: Examples of the raw pull force data. The plots show how much force was exerted on an object as it was pulled out of the grasp of the twelve filament entanglement gripper. The corresponding test setup for each plot is shown in the pictures. Objects are rigidly mounted to the bottom of the test frame and the entanglement gripper is mounted to a load cell on a moving platform above the object. The objects shown are (A) an eight branch tree, (B) a horizontal 63.5 mm diameter tube, (C) a vertical 25.4 mm diameter tube, and (D) a vertical 63.5 mm diameter tube.

but the 63.5 mm tube was large enough that they were lowered inside. As the filaments are pulled up from the object, their coils are extended, which would cause the coil diameter to contract and thereby cause a slight increase in forces as the filaments squeeze the outside of the smaller tube and decreased forces as the filaments pull away from the inner wall of the larger tube.

5.3.5 Grasp toughness metric

While grip strength is a standard metric for robotic grippers, we propose that a more comprehensive metric is the toughness of a grasp - i.e., the energy required to break it. Grasp toughness is evaluated by the integral under the measured force-displacement curve during a pull-out test, which encompasses the elasticity and compliance of a grasp in addition to its strength. This metric scales with both the bending energy to straighten the

	Average maximum value [N]	Maximum of maximum values [N]
4 Branch tree	3.92	6.03
8 Branch tree	6.86	16.18
12 Branch tree	9.14	12.66
8 Upward branch tree	2.306	4.68
8 Downward branch tree	5.99	13.42
1"∅ Tube horizontal	6.85	27.64
2.5"∅ Tube horizontal	8.65	34
1"∅ Tube vertical	1.7	5.5
1.5"∅ Tube vertical	6.98	8.64
2.5"∅ Tube vertical	3.77	9.91
Sphere	0.76	2.06

Figure 5.11: Maximum values observed in the grasping force tests. The left column is the average of the maximum values observed for each set of trials and the right column is the maximum value observed over all trials. The trees with levels arms and the 38.1 mm vertical tube had five trials performed, all other objects had ten trials performed.

filaments and is a function of the topological complexity of the target object and the level of entangling engagement achieved. Values for the entangling 12-filament grasper tested in this work ranges from $10mJ$ for a 10 cm sphere, to $380mJ$ for a simple branched structure, and $770mJ$ for a vertical 51mm cylinder. For comparison, values for the grasp toughness of recently developed soft grippers holding on to cylinders with diameters of 51 to 76mm are $200mJ$ [41], $300mJ$ [40], and $750mJ$ [19]

To calculate the grasp toughness metric, we numerically integrated the area under the averaged force-displacement curves of the grasp strength tests, such as the ones shown in Figure 5.10. The comparison values for the grasp toughness of soft grippers were similarly calculated from the data sets presented in prior soft gripper work, including the four-finger gripper with added tips around a 76 mm tube from Abondance et al. [41], the two finger power grasp around a 51 mm tube from Teeple et al. [40], and the two finger power grasp (with foam) around a 51 mm tube from Galloway et al. [19]. It should be noted that these values are low estimates owing to the fact that the raw grip tests trials were truncated to the shortest release in order to more easily calculate an average run.

5.3.6 Contact distribution

Randomly distributed contact points is a distinguishing feature of entanglement grasping with the filament gripper. To examine the collection of contacts in a given grasp, the filament gripper was mounted onto a frame on top of a rotating platform and five pictures of the example grasps were taken at 45 deg increments. The camera remained stationary while the platform supporting the gripper and support structure were rotated. The objects were manually raised into the filaments to simulate a top drape approach with the fixed gripper mount. Two examples of the results are shown in Figure 5.12. The contacts were grouped by filament, as indicated by the color. Individual contact points were visible in multiple views and thus have the same labels that appear in multiple images. This is difficult and time consuming to quantify in physical experiments but relatively easy to pull out of the simulation environment discussed below in Section 5.4. For comparison between simulations (Sec. 5.4) and physical testing (Sec. 5.3), we manually counted contact points on the four and eight branch tree objects and this is further discussed in Section 5.4.2.

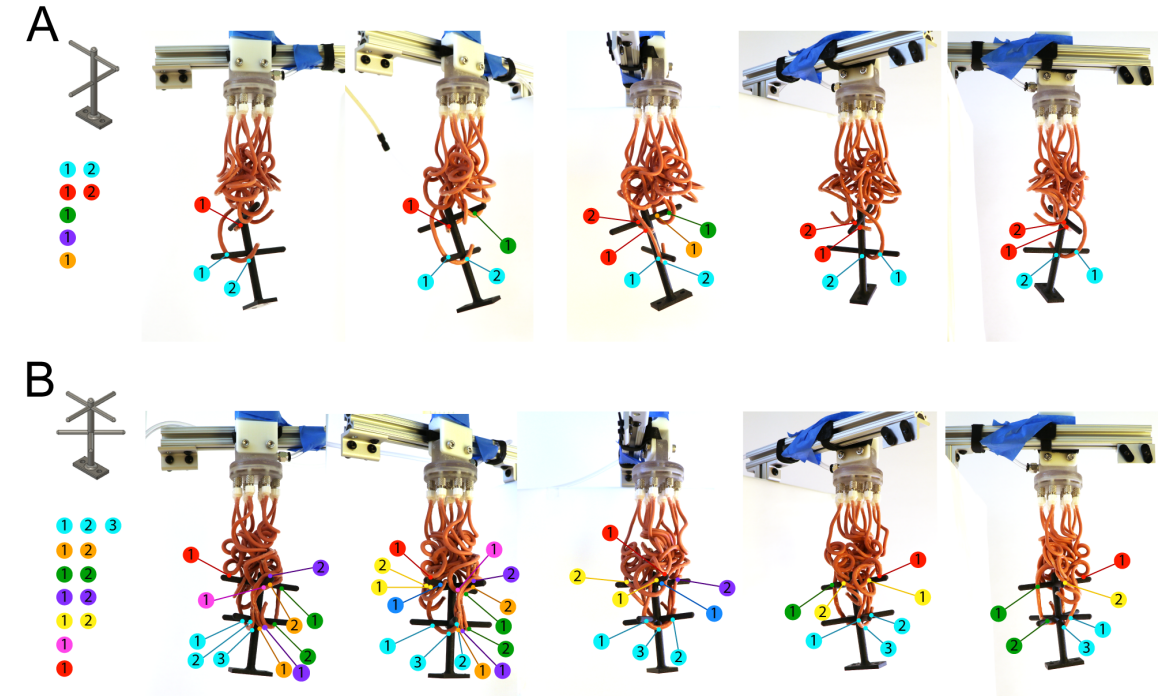


Figure 5.12: Manual count of contact distribution of a four-branch tree from the object set. The pictures are taken at five different orientations, each 45 degrees apart. Individual contact points are counted and labeled. The contacts are grouped by the filament with which they are associated, as indicated by the color of the circle used to mark a contact point. (A) This is an example grasp on a four-branch tree and has seven contact points from five unique filaments on the twelve filament entanglement gripper. (B) An example grasp on an eight-branch tree has thirteen contact points from seven unique filaments on the twelve filament entanglement gripper.

5.4 Exploration of entanglement gripper design space via numerical simulation

To explore the design space of a filament gripper, we use the director-based Cosserat continuum framework for slender filamentous objects [140, 141]. Simulations from this framework were created by Nicholas Charles and the original simulation platform from which it is modified is presented by Gazzola et al. [141]. Details on the framework used to capture the dynamics of entanglement grasping with elastic filaments can be found in the original manuscripts where they are first presented [141, 142]. In the numerical simulation of entanglement grasping, the filaments are suspended from one end and hang straight down

under the force of gravity and are lowered over an object in a top-drape approach. Then, the filament actuation is replicated by changing the intrinsic curvature of the filaments from a straight to a non-zero curvature at the instant of actuation. This curvature, calibrated by measurements of the physical filament actuators, is applied simultaneously over the length of the filament. This follows the assumption that the propagation of internal pressure happens faster than equilibration of grasping dynamics between the filaments and target objects. In isolation, the gripper filaments curl into helices, but the numerical simulation also captures their interactions with neighboring filaments and the target objects, which results in a soft entangled grasp.

The success rate predicted by the numerical simulation in trial grasps of the eight-branch test object compared to results of physical experiments is shown in Figure 5.13 and a side-by-side comparison of example experimental and simulated grasps are shown in Figure 5.15. The simulation framework is able to tangle with and lift a branched structure using a top-drape, remaining successful until the scaled offset is as large as 30% of the target size. The conservative nature of this estimate compared to the results of physical experiments is due to the fact that the simulation does not account for static-frictional effects. Though the simulation framework does not account for the effects of static friction, it is still capable of capturing the qualitative aspects of entanglement mediated grasping and replicating experimental observations, shown in Figure 5.13. The effects of static friction were substantial in grasping objects in the robotic arm tests but are quickly reduced when the grippers is used to grasp objects underwater.

A second influential force that leads to higher success rates in physical testing is electrostatic forces due to charge build-up in sliding filaments. The effect of charge build-up is that the filaments repel one another, casting a greater radius of spread in their free ends as they're draped over a target object. The effect of static charging is visible in the top-drape approach shown in Figure 5.6.

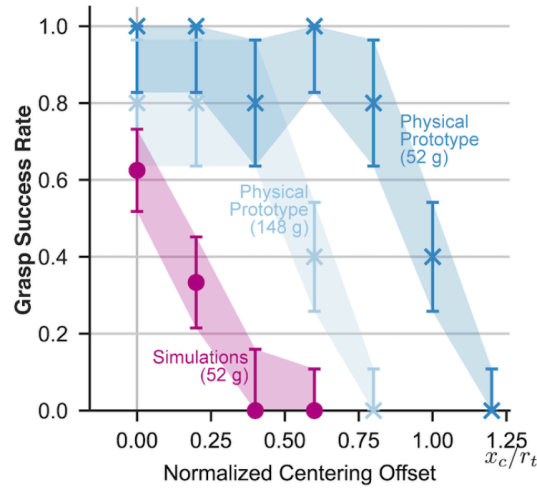


Figure 5.13: A plot of the experimental and simulated position error sensitivity while grasping a 52g eight-branch tree test object in comparison to the results presented in Figure 5.9 with a 148g eight-branch tree.

5.4.1 Entanglement grasp success phase space

Using the simulation to replicate the interactions among entanglement-grasper filaments and the branched structure target object, we explored the design space around the twelve-filament prototype gripper in terms of a phase space that spans the ratio of the target object spatial density ϕ_T , the filament spatial density ϕ_G , and a ratio of the density of the target object to that of the gripper. Three examples of these trials are shown in Figure 5.14, as well as their location on four planes of this phase space. Each point on the plots in Figure 5.14 represents the results of seven trial runs of a simulated object grasp-and-pickup of an eight-branch structure like the one used in physical testing. An individual trial was considered successful if the object was lifted off of the ground and remained suspended after 60s in the simulated time frame. The contour plot shows the success rate at the individual points and interpolates the predicted success rate between trial points using a Delaunay triangulation.

The effect of increasing target weights (from left to right in Figure 5.14) is predictable but still interesting to see the degradation of the successful grasping space as the gripper pulls on heavier objects. Similarly, lower spatial density in the target object (longer branches) makes the target easier to pick up until the benefit of accessible entanglement area is counteracted by cumulative mass. At first, one might also expect the filament spatial density to have similar implication on performance when, in fact, the grasp success rate shows much less sensitivity to this lumped variable than to the object spatial density. Observing the entanglement behavior of the physical system as well as the numerical simulation quickly clarifies that the starting spacing becomes less apparent as the filaments are actuated. With a dynamic actuation, the filaments bump into one another and the target object, swinging around and increasing entanglement. Additionally, in the initial moments of actuation, before the filament snaps into a coil, the tips of the filaments begin to shift several centimeters from their starting position, thus counteracting effects of their initial spatial density.

The dimensionless parameters above were selected as a tractable starting set with which to explore the generalized design or phase space of entanglement grippers. In future work, it will be interesting to expand the phase space to include additional parameters, incorporating more information about object topology and filament characteristics, as well as further exploration of the actuation and approach strategies.

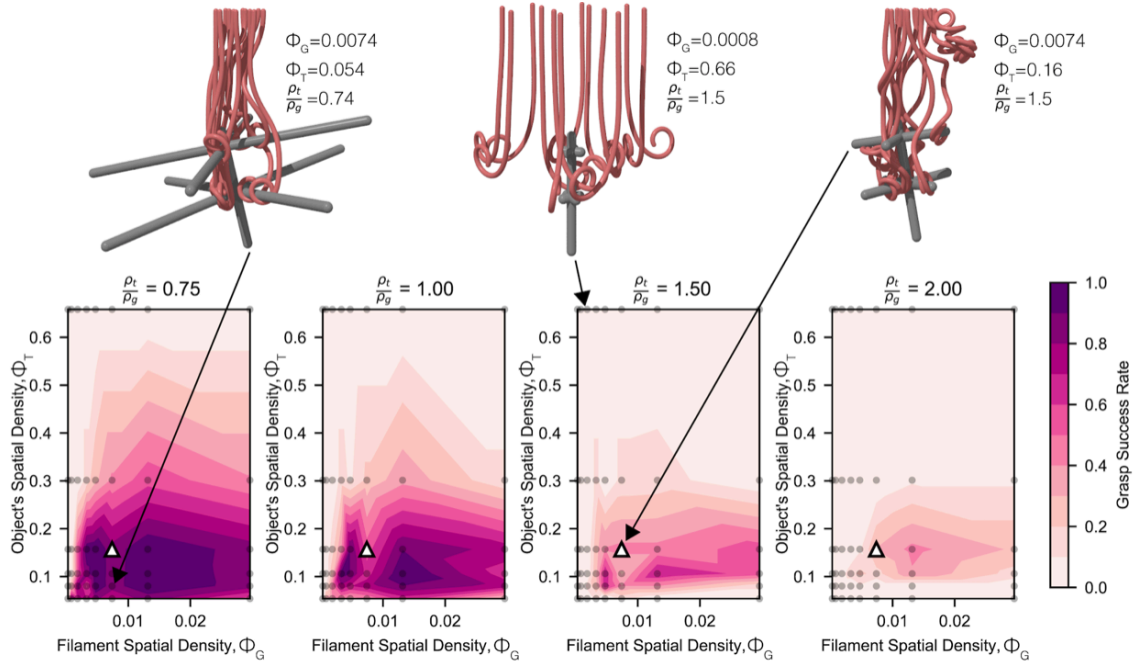


Figure 5.14: Example simulated trials of varying target size, filament spacing, and object density. The location of these samples on the phase space below is indicated. The phase space shows the success rates of simulated grasp tests assuming perfect centering over the eight-branch test object with varying gripper filament spacing, branch length, and four densities of the test object. The prototype and object parameters used in physical testing are indicated by the white triangle.

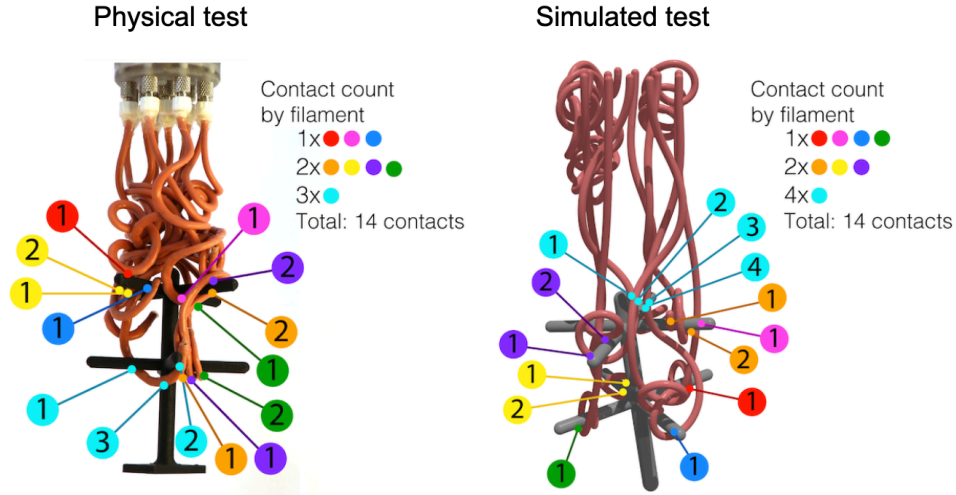


Figure 5.15: Examples of contact distributions when the entanglement gripper holds an 52g eight-branch tree in a physical test and simulated test. Contacts are indicated and sorted by the number of contacts made by unique filaments. In both of the examples shown, 14 contacts are made with eight unique filaments from an array of 12 filaments.

5.4.2 Preliminary contact study

From each of the grasp test simulations represented in Figure 5.14, it was possible to extract information on the contact points between the gripper and tree. The number of contact points observed from successful grasp simulations ranged from 11 to 32 discrete points of contact. The contacts from the pictured eight branch object grasp in Figure 5.12 is shown in Figure 5.15, next to an example of a simulated grasp of an eight-branch structure. In the examples shown, fourteen contact points are made by eight of the twelve gripper filaments. Not all contacts counted were necessarily load bearing, as can be inferred by the examples in Figures 5.12 and 5.15, but this suggests that, for a given filament strength, there is a critical threshold of engagement or contacts that leads to a successful grasp and that the number of contact points increases with target object weight. We have observed successful grasps with lower numbers of contacts from physical testing but this is dependent on the object weight and static friction, (which is not represented in the simulation). In future work, we can look at the spatial distribution of contacts in addition to the number of contacts to further characterize the engagement of entanglement grippers with their target objects. The entanglement gripper performance and contact also changes with object topology, which we intend to explore further in future work.

5.5 Prototype entanglement gripper

5.5.1 Hardware

The gripper used for all of the physical tests in this chapter is comprised of twelve silicone filaments attached to a 3D printed palm (manifold). The filaments were approximately 260 mm in length and 4.5 mm in diameter prior to actuation. The filaments were mounted to polypropylene and nylon luer lock plug to barb fittings (McMaster PN51525K141, PN51525K121) on one end and sealed at the other end. The luer lock fittings mounted in the ends of the filaments attached to a 3D-printed manifold via nickel coated brass threaded luer lock sockets (McMaster PN51465K161). This allowed for modular repairs and replacement of individual filaments in the case of a leak. The individual ports on the manifold could also be closed with luer lock end plugs (McMaster PN51525K311) for fewer numbers of filaments and easily rearranged for different array formations, although the testing in this study utilized all twelve ports for all of the experiments. The Manifold was printed in a semi transparent resin (Stratasys Vero Clear OBJ-03271) on a Stratasys polyjet 3D printer. Three different mounting attachments were used for (1) mounting to the robot arm for grasp testing, (2) mounting in the materials characterization system (Instron 5544A) for grip strength tests, and (3) mounting on a ROV for deep-sea tests. For all of the tests, however, the configuration of the ports on the distal portion of the gripper remained the same. The ports were evenly spaced in two concentric circles. The outer circle had diameter of 50 mm and contained eight of the twelve ports, while the inner circle had a diameter of 25 mm and contained the remaining four of twelve filaments.

5.5.2 Filament actuator fabrication

Following the procedures outlined in Chapter 4, the filament actuators were made from silicone rubber, Elastosil m4601 (Wacker Chemie). The rubber filaments were formed by dip molding silicone onto 305 mm (12 in) long stainless steel pins (McMaster-Carr 88915K11). The pins (or rods) were coated with liquid silicone rubber and then fixed at a 10 degree angle from vertical while the rubber cured. For the fabrication of the filaments, it was easier to suspend the rods from above, and the rods remained suspended between successive coatings. The filaments used for the tests in this study were formed with four coatings on pins that were 10 deg from vertical. To ease the release of actuators off of longer

pins, the pin was pulled off of the dipping fixture and the ends trimmed while still on the pin. Removal of the silicone from the pin was aided by 15-30psi of air pressure applied via a 1/16in hose barb into one side of the silicone. This does not create a perfect seal but supplies enough internal pressure to cause the actuators to expand and slip off of the pin more easily. This demolding pressure may be modulated depending on the operating pressure of the actuators. Care was taken to apply tension to the actuator during removal from the pin so that, if the barb slipped and the internal pressure dropped, the actuator did not snap back and stretch over the tip of the pin, potentially creating a weak spot or pin hole.

After removing the actuators from their forming pins, one end was sealed using Sil-Poxy (Smooth-On Ic.) or newly mixed Elastosil. For filaments used in a deep-sea field test, 1/16" diameter, 1/4" long steel pins were inserted into the end before sealing it. This served the purpose of weighting the ends to make them settle down faster after being moved through the water. The filaments otherwise drift in the water and are harder to direct. The pins also allowed the ends of the filaments to stick to a magnet on the ROV holster to keep them from drifting around until deployment. The remaining end of the filament was fixed onto a plastic 1/16" Luer-lok barb (part listed above) and secured with Sil-Poxy and a wrapping of cotton twine (McMaster-Carr PN1929T12). After all Sil-Poxy and rubber was fully set, the Luer-lok fitting could then be attached to the gripper manifold as described above.

5.5.3 Pneumatic actuation and control

For repeatable and tunable actuation of the filaments in the robot arm grasp testing, the input pressure of the filament gripper was controlled by a custom pneumatic pressure control system based on the system used in the studies of Teeple et al. and Abondance et al. [40, 41]. The controller enables execution of arbitrary pressure trajectories in real time with an accuracy of 1.4 kPa. The working control range is between -35 kPa and 350 kPa, and preliminary testing shows this system has a response time of approximately 0.2 s, enabling high-bandwidth operation. Finally, the system utilizes custom ROS drivers allowing high-level coordination between the gripper (pressure controller) and our robot arm. As this system is being actively developed at the time of writing, documentation about the hardware and software is available on GitHub [143].

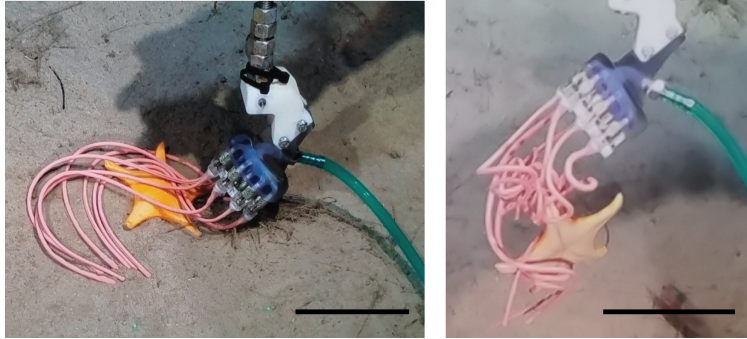


Figure 5.16: Photos from a field test at 800m under water, demonstrating that the filaments can also be operated hydraulically and can operate under high hydrostatic pressure. The scale bars in the images represent 10cm.

5.5.4 Field tests and challenging objects

In addition to the set of objects used for laboratory and simulation grasp tests, the gripper was tested on a remotely operated arm and ROV in a deep-sea field test evaluation. This adds the complications of a different surrounding fluid, currents, unpredictable target objects, and limited testing vision and feedback. A twelve-filament array like the set used for the laboratory and simulated grasp success testing was successfully used to pick up a benthic sea star at a depth of 800 m (Fig. 5.16), which was then released after grasping. The field tests were performed with the help of the Schmidt Ocean Institute, the crew of the Falkor, the ROV pilots operating the vehicle SuBastien, and our collaborators from the URIL (Undersea Robotics & Imaging Laboratory) lab at the University of Rhode Island. Development of the entanglement gripper was originally motivated by challenging grasping tasks in the deep-sea, where the gentle grasps of deep sea life and precious artifacts cannot be done by human hands due to the hydrostatic pressure.

While the filament gripper was originally inspired by challenging deep-sea grasping tasks, entanglement grasping can also augment the abilities of robotic grasping with everyday objects on land. As discussed above, we have begun initial performance characterization with a small subset of test objects. Rigorous testing with more complex objects, as well as discussion of how to classify the complexity of objects will be a subject of future study. The set of objects in Figure 5.17 is intended to demonstrate the feasibility of using entanglement grasping for familiar household objects that might prove more challenging for the vast majority of robotic grippers. The collection includes an array of houseplants, irreg-

ularly shaped toys, and a flexible phone tripod. The grasping demonstrations in Figure 5.17 were not performed with a robot arm. To emulate a top drape approach while allowing the gripper to remain in a static position, the object was manually raised up into the array of unactuated filaments and the filaments were then pneumatically actuated around the object with an operating pressure of 25 psi (172 kPa).



Figure 5.17: Topologically complex household objects held by a 12-filament entanglement gripper.

5.6 Conclusion

Secure and gentle grasping of an object often requires a characterization of the size, shape, mass distribution, and stiffness of the target. This characterization requires perception, planning, and action with feedback. Distributed contact realized in entanglement grasping offers an embodied solution to this problem. The flexible topology and geometry of the grasper leads to adaptable grasping without perception, planning, or feedback. In laboratory experiments, the filament gripper excelled when grasping topologically complex targets (torus, branched structures), which would normally challenge traditional grasping platforms. Features such as curved surfaces and narrow cuts or protrusions traditionally

make a target object more challenging to grasp [125, 4] but provide more features on which curling filaments can catch and hold onto an object. Conversely, our entanglement gripper had trouble with simpler objects like spheres and vertical tubes, which are easier for traditional grippers due to convexity and rotational symmetry. While many household objects are simple in shape (for example, most objects in the YCB Object set are cylindrical, spherical, or rectangular [138]), many objects such as plants, produce, cables, and other high aspect ratio or porous objects are much more topologically complex. The entanglement gripper can blindly distribute contact on complex objects without the need for planning, but may not distribute contact sufficiently on simpler objects.

In this first instantiation of robotic grasping via entanglement, the goal was to demonstrate the use of a uniform array of filament grippers to adapt to complex topologies without perception, planning, or controls. In this passive mode of operation, an entanglement gripper is able to excel in grasping objects that would be challenging for traditional grippers in both their passive and active operational modes. In future work, however, we can explore the potential of a hybrid approach, where some level of perception and control is combined with the benefits of the stochastic nature of entanglement. We can explore sensorization of the filaments and composite gripper to trigger actuation without central control, like the ambush hunting behavior of medusae, siphonophorae, and ctenophorae [136]. By incorporating strain or capacitance sensing, the filaments may also be able to provide information about the material and topology of objects with which it is interacting, expanding on the differing entanglement pull-out force profiles discussed above. With further characterization of target object topologies and interactions with the filaments, we can also introduce a hybrid of planned dynamic approaches and random distribution of contacts for more strategic grasping. Or, remaining in a passive operational mode, the use of non-uniform arrays might allow adaptation to more target object variability. Conversely, the coiling behavior of the filaments could be tuned to down-select for certain characteristic topologies. This is a new platform for robotic grasping as well as a new grasping strategy with a wide space for potential exploration.

Chapter 6

Conclusions and Future Work

The three modalities of contact tuning that were explored in this thesis include passive contact tuning via materials and structure, active contact tuning via control over surface structure, and distributed contact via large arrays of highly compliant actuators. These modalities were leveraged to create soft robotic grippers that are gentle, conformal, secure, and adaptive. Gentleness could be quantified as contact pressure passively limited to 2 kPa or less. The quality of being conformal was quantified on a pressure map to show an increase in contact area and reduction of stress concentration, as well as visually demonstrating a grasp that could adapt to object diameters ranging from approximately 1 to 10 cm without significant change on the contact stress. Security of grasps was confirmed by quantifying the forces required to break a gripper's hold on an object, and ranged from 10 to 60 N. Finally, adaptability was demonstrated as both a friction tuning mechanism to increase the pose dexterity as well as via the introduction of a stochastic grasping strategy that uses highly compliant filaments to blindly adapt to complex geometries. From the desktop to the deep sea, the resulting grippers excel in grasping and manipulating target objects that are challenging for traditional grippers, including objects that are compliant, fragile, or topologically complex. In doing so, these grasping strategies are not poised to replace traditional rigid grippers but can be used to augment what is currently possible with robotic grasping as a whole.

6.1 Integration

Moving forward, the three contact tuning modalities were explored relatively independently of one another but can be more directly integrated, creating a system that is both functionally and physically hierarchical. With the feasibility of these modalities demonstrated individually, the next challenge is developing fabrication methods for full integration of these concepts into multi-functional soft systems. I presented fabrication methods that are independently robust and demonstrated their compatibility with other soft manufacturing processes, such as microfluidic fabrication. More work remains, however, to ensure that system integration is scalable and easily translated to other practitioners in the field without extensive experience. While the creation of the friction tuning mechanism soft actuator and arrays has been made simple, their integration into larger systems is not yet a straightforward process. As an example, for the friction-tuning mechanism to be useful to a robotic manipulation specialist, or soft arrays useful as a model for a biologist to study ciliary beating patterns, the platforms should have a relatively straightforward standard operating procedure for modifying designs and incorporating them into soft and rigid robotic systems.

Within any system, soft or rigid, hierarchical structures translate to an increasing span of functional scales. As the range of scales represented in a single construction increases, so does the complexity of fabrication. Adding to this complexity is that fact that modular integration of soft components is not possible in the way that it is for rigid components. Soft components, for example, cannot be bolted, braised, or bonded together in the same way that rigid components might. The integration of soft components and functional structures, therefore, must typically be integrated in both the design and fabrication processes from a very early stage. A future goal is to introduce a library of methods for low profile modular and seamless integration for similar soft systems.

6.2 Passive tuning: surface and structure

Chapters 2 and 3 explored passive contact tuning via materials and structure, as well as active contact tuning via control over surface structure, respectively. Ultimately, the notions of active versus passive, and underlying structures versus surface structures can also be interchanged. Active tuning of the underlying structure can be used to affect the

contact interface, and passive surface structures can be used to adjust friction and adhesion. Active stiffening of the underlying structure is an area of interest in the field of soft robotics, largely explored via phase transition materials and jamming [144, 145, 146]. These could be further explored for the express intention of tuning the contact interface of a gripper via the controllable stiffening of the underlying structure. Passive surface structures to tune contact, particularly bio-inspired adhesion and suction, have also been explored in soft materials [147, 65, 81, 148, 149].

Active or passive, the interplay between internal and surface structure is very apparent. One can isolate the surface structure on a rigid substrate for characterization, but the underlying mechanics should also be taken into consideration when evaluating the role of surface structures implemented in soft systems. Furthermore, I believe merging the two for consideration will be a challenging but interesting area for further study. Mentioned in Chapter 3, as an interesting example of this, Geckos have been hypothesized to modulate pressure in their underlying vasculature to aid in attachment to and release from substrates [150].

6.3 Application of friction tuning: dexterous manipulation

The concept of a gripper with friction-tunable fingers tips was presented in Chapter 3 with a demonstration of the capacity to modulate surface friction. Most prior work on tuning the adhesion forces in soft robots has targeted increased adhesion for climbing or increased grasp force. In contrast, the intent of the mechanism presented was to increase dexterity of a soft gripper. Since the publication of the original manuscript, there has also been expressed interest in incorporating related mechanisms for the purpose of adaptive manipulation in rigid robotic grippers [61]. The next logical step for this work in soft contact is to incorporate the mechanism into a study that further evaluates the use of tunable friction in a soft gripper for dexterous manipulation. For example, one might incorporate an element of friction tuning to augment the in-hand soft manipulation demonstrated by Abondance et al. [41].

In future work, the friction pads should also be made into a lower profile setup that can flex with the surface of the larger actuators to which they are coupled. The underlying support structure on the back side of the friction pads, while made of soft material, was not very compliant. This contributed to the decision to only apply friction pad to the tip

of the soft digits and not the entire inner surface. A lower profile version of this structure could be modularly coupled to soft gripper with the use of the lacing and bridging material techniques discussed in Chapter 2, or they could be integrated more directly in to the finger structure.

As I demonstrated in a simple gripper and crawler, coupling of the pneumatic control between the surface structure and supporting actuator can also be handled in two ways. One can opt for separate control of the friction and underlying actuator as demonstrated in the gripper digits (2DOF). The other option is coupling the friction directly to the pressurized volume of the underlying actuator, as was done with the crawler leg (1DOF). Either means of coupling could be applied to grasping and locomotion but there is an opportunity for more development of the direct coupling approach to further tune the actuation profile. By tuning the relative pressures at which individual components of the integrated system operate, the surface structures and underlying structures can be engage sequentially at different pressures supplied by the same pressure line. This was demonstrated in the crawler but could be optimized to better emphasize the hysteretic path and forward motion.

6.4 Application of arrays: study of biological systems

Soft robots benefit from incorporating bio-inspired soft structures. Our understanding of soft biological structures can also benefit from the use of soft robots [103, 151, 152]. In Chapter 2, I described how we developed tools to carefully handle precious specimens from the deep sea, but soft structures can also be used to directly emulate and thereby study the morphology and behavior of soft biological systems. In particular, the large arrays of high aspect ratio soft actuators introduced in Chapter 4 are a new platform that could be leveraged in the study of behavior like cilia beating and fluid flow manipulation [153, 154, 155], or the locomotion of echinoderms and coordination of their tube feet [156]. Milana et al. propose a pneumatic cilium morphology with two input chambers for the purpose of creating a hysteretic stroke for greater fluid propulsion but were limited to experiments with a single cilium [86] and the single-chamber predecessor of this setup was limited to a six-part array [110]. By modifying my dip molding process, a large, a dip-molded, 2D array of similar two-chamber soft actuators could be used to explore more complex cilia beating patterns and interactions. As demonstrated in Chapter 2, it would also be possible to create an array composed of tri-chambered dip-molded actuators for two

degrees of freedom in each cilium.

With the ability to control large soft arrays, address segments or individual actuators within the arrays, and program arbitrary vector field of actuation, this platform can augment biological study by complementing the findings of biological observation and numerical simulation. A physical array of actuators could, for example, be programmed to test open loop patterns for fluid flow manipulation or robot locomotion. In a closed loop format, the arrays could also be incorporated into experiments to explore the implementation of coordination and distributed control in soft bodies.

6.5 Further exploration and application of entanglement

Entanglement grasping was presented in Chapter 5 as a novel strategy enabled by the combined geometric and material compliance of the filament-like actuators introduced in Chapter 4. We examined the gripper's sensitivity to object topology and centering error. The effects of gripper and target spatial density were also characterized in a non-dimensionalized phase space. This begins to construct an understanding of the functional design space for entanglement grasping but does not yet incorporate secondary design possibilities, including intentional variance of the characteristic curvature of the filaments, filament length, and staggered operating pressure and actuation times for the filaments. Furthermore, passive or active surface tuning structures may also be incorporated into the filaments.

The arrays of filament actuators used to demonstrate entanglement grasping were uniform. However, intentional randomness or controlled variation in the filament curvature, diameter, and length might allow the gripper to accommodate a greater diversity of objects. Conversely, the filaments could be tuned to passively filter and select for targets with specific characteristic dimensions, weight, surface roughness, or topological complexity. Similarly, as discussed in Chapter 5, the engagement forces between an entanglement gripper could be used to assess characteristics of the object structure without the help of vision or other sensing.

Applications of interest that would motivate coupling entanglement grippers with sensing might include using entanglement grippers for picking produce or automation of moving or pollinating plants for breeding programs. The grippers might just need sufficient vision to position above a plant or sensing could be enhanced to sniff for and respond to

ripe produce. A medusae jellyfish inspired entanglement gripper could also be developed to mimic the ambush predators that snatch materials of interest that drift into their tentacles [136]. In this case, the materials of interest might be floating refuse, which the gripper could collect from the ocean. An entanglement gripper might sift through refuse for potentially recyclable or reusable materials, responding when the tentacles come in contact with metals or other recyclable materials.

6.6 Hybrid control with embodied intelligence

Each of the gripper systems presented was either controlled by a human operator or functioned in a pre-programmed open loop format. This is the typical mode of operation for deep-sea biological sampling and it allows us to demonstrate the extent to which embodied intelligence or passive control can be programmed into the skin and body of the compliant structures. However, a next clear step is to sensorize the actuators to create autonomous systems for applications like produce and plant manipulation, or to create the medusae inspired recycling bot mentioned above. Adding sensors would also be a logical next step to study distributed system behavior like the beating of cilia, or sea star tube foot locomotion and feeding behavior. If the arrays are outfitted to sense chemical, pressure differentials, or contact, they could be used to test distributed response to stimuli. Experiments of interest would look at the balance of central and localized control as compared to the biological analogs of cilia [156], tube feet, and tentacles.

6.7 Tools for soft system design and innovation

As discussed in Chapter 2, a design tool that helps to rapidly simulate and experiment with actuatable soft structures could strategically complement experimental and robust numerical analysis. Though computing power continues to become cheaper and readily available, I believe there is still currently potential value in the idea of a rapid digital prototyping tool that comprises some level of detail and accuracy for the purpose of easy early ideation and feasibility exploration. A prototype tool to illustrate this concept was presented in Chapter 2 but was limited to relatively simple panel-based construction and could be made much more flexible to incorporate arbitrary geometries. Additionally, the tool could incorporate some ability for simple multi-variable optimization. Variables of

interest might include the degree of motion achieved in actuation, deflection under applied load, compliance in a non-actuated state, or differential of directional compliance.

The tool demonstrated in Chapter 2 also does not reflect thickness, which detracts from the accuracy but aids in reducing the computational cost. In place of incorporating thickness in the design, the tool could implement a simplistic surrogate of variable stiffness within a body. This would capture some of the effect of thickness and focus on the conceptual design of an actuator rather than the exact form. After conceptual development, a designer would later transition to more rigorous FEA. In developing tools explicitly for the purpose of exploratory design of soft structures, it would also be an interesting study to observe how the tools used for concept development (and for more detailed design work) effect the resulting soft robotic system. This is directly related to and inspired by the the work of Tsai et al. [5].

By studying how our designs vary based on the tools used to create them, we may be able to isolate some of the the biases (likely from foundations in rigid systems) that we bring into the development of soft systems. Another proposal to drive innovation in the design of soft systems is to apply artificial intelligence or frameworks inspired by artificial intelligence to the design of soft robots [51, 157]. I think these proposals will lead to valuable design of soft structures but, in the near term (<10 years), I think the more immediate utility may be the potential for artificial intelligence to help us reflect on the design process, distilling problems down to the core functional requirements, and systematically evaluating new design spaces. Selfishly, as a designer, I hope that the development of artificial intelligence based design tools will expose some of the rigid-system-derived biases and blind spots, of which we are not yet aware.

6.8 Conclusion

Soft robotics is at a stage that holds a lot of potential for the intersection of design and fabrication. I think the success and broader application of soft systems will depend on the development of soft-material-specific design and fabrication methodologies. This will have to include both exploratory innovation as well as more detailed optimization of scalable and robust manufacturing methods. It is also an opportunity to re-examine the tools and methods that we have at our disposal and to create new tools and methods.

Bibliography

- [1] P. Paoletti, G. W. Jones, and L. Mahadevan, “Grasping with a soft glove: intrinsic impedance control in pneumatic actuators,” *Journal of the Royal Society Interface*, 2017.
- [2] H. Lipson, “Challenges and Opportunities for Design, Simulation, and Fabrication of Soft Robots,” *Soft Robotics*, vol. 1, no. 1, pp. 21–27, 2014.
- [3] K. J. Cho, J. S. Koh, S. Kim, W. S. Chu, Y. Hong, and S. H. Ahn, “Review of manufacturing processes for soft biomimetic robots,” *International Journal of Precision Engineering and Manufacturing*, vol. 10, no. 3, pp. 171–181, 2009.
- [4] D. Morrison, P. Corke, J. Leitner, and J. Leitner, “EGAD! An Evolved Grasping Analysis Dataset for Diversity and Reproducibility in Robotic Manipulation,” *IEEE Robotics and Automation Letters*, vol. 5, no. 3, pp. 4368–4375, 2020.
- [5] G. Tsai and M. C. Yang, “How It Is Made Matters: Distinguishing Traits of Designs Created by Sketches, Prototypes, and CAD,” in *Volume 7: 29th International Conference on Design Theory and Methodology*, (Cleveland), pp. 1–12, American Society of Mechanical Engineers, 8 2017.
- [6] R. Danovaro, C. Corinaldesi, A. Dell’Anno, and P. V. Snelgrove, “The deep-sea under global change,” *Current Biology*, vol. 27, no. 11, pp. R461–R465, 2017.
- [7] P. A. Tyler, M. Baker, and E. R. Llodra, “Deep - Sea Benthic Habitats,” in *Biological Sampling in the Deep Sea* (M. R. Clark, M. Consalvey, and A. A. Rowden, eds.), ch. Deep-Sea B, pp. 1–15, John Wiley & Sons, first edit ed., 2016.
- [8] C. Darwin, *The Structure and Distribution of Coral Reefs*. New York: Appleton and Co., 3rd. editi ed., 1889.

- [9] C. Wilkinson, “Status of Coral Reefs of the World: 2008,” tech. rep., Global Coral Reef Monitoring Network and Reef and Rainforest Research Centre, Townsville, Australia, 2008.
- [10] P. Bongaerts, T. Ridgway, E. M. Sampayo, and O. Hoegh-Guldberg, “Assessing the ‘deep reef refugia’ hypothesis: Focus on Caribbean reefs,” *Coral Reefs*, vol. 29, no. 2, pp. 1–19, 2010.
- [11] D. M. Holstein, T. B. Smith, J. Gyory, and C. B. Paris, “Fertile fathoms: Deep reproductive refugia for threatened shallow corals,” *Scientific Reports*, vol. 5, pp. 1–12, 2015.
- [12] C. Menza, M. Kendall, and S. Hile, “The deeper we go the less we know,” *Revista de Biologia Tropical*, vol. 56, no. May, pp. 11–24, 2008.
- [13] S. E. Kahng, J. M. Copus, and D. Wagner, “Recent advances in the ecology of mesophotic coral ecosystems (MCEs),” *Current Opinion in Environmental Sustainability*, vol. 7, pp. 72–81, 2014.
- [14] H. W. Fricke, E. Vareschi, and D. Schlichter, “Photoecology of the coral *Leptoseris fragilis* in the Red Sea twilight zone (an experimental study by submersible),” *Oecologia*, vol. 73, no. 3, pp. 371–381, 1987.
- [15] J. S. Sparks and D. F. Gruber, “A new mesophotic clingfish (Teleostei: Gobiesocidae) from the Bahamas,” *Copeia*, no. 2, pp. 251–256, 2012.
- [16] O. Nir, D. F. Gruber, S. Einbinder, S. Kark, and D. Tchernov, “Changes in scleractinian coral *Seriatopora hystrix* morphology and its endocellular Symbiodinium characteristics along a bathymetric gradient from shallow to mesophotic reef,” *Coral Reefs*, vol. 30, no. 4, pp. 1089–1100, 2011.
- [17] M. S. Roth, J. L. Padilla-Gamiño, X. Pochon, R. R. Bidigare, R. D. Gates, C. M. Smith, and H. L. Spalding, “Fluorescent proteins in dominant mesophotic reef-building corals,” *Marine Ecology Progress Series*, vol. 521, pp. 63–79, 2015.
- [18] B. R. Kennedy, K. Cantwell, M. Malik, C. Kelley, J. Potter, K. Elliott, E. Lobecker, L. M. K. Gray, D. Sowers, M. White, S. France, S. Auscavitch, C. Mah, V. Moriwake,

- S. Bingo, M. Putts, and R. D. Rotjan, “The unknown and the unexplored: Insights into the Pacific deep-sea following NOAA CAPSTONE expeditions,” *Frontiers in Marine Science*, vol. 6, no. JUL, pp. 1–21, 2019.
- [19] K. C. Galloway, K. P. Becker, B. Phillips, J. Kirby, S. Licht, D. Tchernov, R. J. Wood, and D. F. Gruber, “Soft Robotic Grippers for Biological Sampling on Deep Reefs,” *Soft Robotics*, vol. 3, no. 1, pp. 23–33, 2016.
- [20] O. Nir, D. F. Gruber, E. Shemesh, E. Glasser, and D. Tchernov, “Seasonal mesophotic coral bleaching of Stylophora pistillata in the northern Red Sea,” *PLoS ONE*, vol. 9, no. 1, 2014.
- [21] S. Mehr, A. Verdes, R. DeSalle, J. Sparks, V. Pieribone, and D. F. Gruber, “Transcriptome sequencing and annotation of the polychaete *Hermodice carunculata* (Annelida, Amphinomididae),” *BMC Genomics*, vol. 16, no. 1, pp. 1–13, 2015.
- [22] S. F. Pooyaei Mehr, R. DeSalle, H. T. Kao, A. Narechania, Z. Han, D. Tchernov, V. Pieribone, and D. F. Gruber, “Transcriptome deep-sequencing and clustering of expressed isoforms from *Favia* corals,” *BMC Genomics*, vol. 14, no. 1, p. 1, 2013.
- [23] M. Tessler, M. R. Brugler, J. A. Burns, N. R. Sinatra, D. M. Vogt, A. Varma, M. Xiao, R. J. Wood, and D. F. Gruber, “Ultra-gentle soft robotic fingers induce minimal transcriptomic response in a fragile marine animal,” *Current Biology*, vol. 30, no. 4, pp. R157–R158, 2020.
- [24] E. Brown, N. Rodenberg, J. Amend, a. Mozeika, E. Steltz, M. R. Zakin, H. Lipson, and H. M. Jaeger, “From the Cover: Universal robotic gripper based on the jamming of granular material,” *Proceedings of the National Academy of Sciences*, vol. 107, no. 44, pp. 18809–18814, 2010.
- [25] M. Cianchetti, a. Arienti, M. Follador, B. Mazzolai, P. Dario, and C. Laschi, “Design concept and validation of a robotic arm inspired by the octopus,” *Materials Science and Engineering C*, vol. 31, no. 6, pp. 1230–1239, 2011.
- [26] F. Ilievski, A. D. Mazzeo, R. F. Shepherd, X. Chen, and G. M. Whitesides, “Soft robotics for chemists,” *Angewandte Chemie - International Edition*, vol. 50, no. 8, pp. 1890–1895, 2011.

- [27] P. Polygerinos, Z. Wang, K. C. Galloway, R. J. Wood, and C. J. Walsh, “Soft robotic glove for combined assistance and at-home rehabilitation,” *Robotics and Autonomous Systems*, vol. 73, pp. 135–143, 2015.
- [28] M. Cianchetti, T. Ranzani, G. Gerboni, T. Nanayakkara, K. Althoefer, P. Dasgupta, and A. Menciassi, “Soft Robotics Technologies to Address Shortcomings in Today’s Minimally Invasive Surgery: The STIFF-FLOP Approach,” *Soft Robotics*, vol. 1, no. 2, pp. 122–131, 2014.
- [29] A. Stilli, H. A. Wurdemann, and K. Althoefer, “Shrinkable , stiffness-controllable soft manipulator based on a bio-inspired antagonistic actuation principle,” *IEEE/RSJ International Conference on Intelligent Robots and Systems*, no. Iros, pp. 2476–2481, 2014.
- [30] T. Noritsugu, M. Takaiwa, and D. Sasaki, “Power assist wear driven with pneumatic rubber artificial muscles,” *15th International Conference on Mechatronics and Machine Vision in Practice, M2VIP’08*, pp. 539–544, 2008.
- [31] H. S. Stuart, S. Wang, B. Gardineer, D. L. Christensen, D. M. Aukes, and M. Cutkosky, “A Compliant Underactuated Hand with Suction Flow for Underwater Mobile Manipulation,” pp. 6691–6697, 2014.
- [32] A. Dollar and R. Howe, “A robust compliant grasper via shape deposition manufacturing,” *IEEE/ASME Transactions on Mechatronics*, vol. 11, no. 2, p. 154–161, 2006.
- [33] P. Polygerinos, Z. Wang, K. Galloway, B. Overvelde, and R. Wood, “Soft Elastomeric Actuators with Fiber Reinforcement,” *Materials Research Society*, p. 2, 2013.
- [34] K. Suzumori, S. Iikura, and H. Tanaka, “Development of flexible microactuator and its applications to robotic mechanisms,” *Proceedings. 1991 IEEE International Conference on Robotics and Automation*, no. April, pp. 1622–1627, 1991.
- [35] D. Lane, J. Davies, G. Robinson, D. O’Brien, J. Sneddon, E. Seaton, and a. Elfstrom, “The AMADEUS dextrous subsea hand: design, modeling, and sensor\nprocessing,” *IEEE Journal of Oceanic Engineering*, vol. 24, no. 1, pp. 96–111, 1999.

- [36] I. D. Walker, D. M. Dawson, T. Flash, F. W. Grasso, R. T. Hanlon, B. Hochner, W. M. Kier, C. C. Pagano, C. D. Rahn, and Q. M. Zhang, “Continuum robot arms inspired by cephalopods,” *SPIE Conference on Unmanned Ground Vehicle Technology*, vol. 5804, pp. 303–314, 2005.
- [37] N. M. W. Editors, *Bioinspired Sensing, Actuation, and Control in Underwater Soft Robotic Systems*. Cham: Springer International Publishing, 2021.
- [38] S. Aracri, F. Giorgio-Serchi, G. Suaria, M. E. Sayed, M. P. Nemitz, S. Mahon, and A. A. Stokes, “Soft Robots for Ocean Exploration and Offshore Operations: A Perspective,” *Soft Robotics*, vol. 00, no. 00, pp. 1–15, 2021.
- [39] A. Rodriguez, M. T. Mason, and S. S. Srinivasa, “Manipulation Capabilities with Simple Hands,” in *Experimental Robotics* (O. Khatib, V. Kumar, and G. Sukhatme, eds.), ch. Grasping a, pp. 285–299, Springer, 2014.
- [40] C. B. Teeple, T. N. Koutros, M. A. Graule, and R. J. Wood, “Multi-segment soft robotic fingers enable robust precision grasping,” *International Journal of Robotics Research*, vol. 39, no. 14, pp. 1647–1667, 2020.
- [41] S. Abondance, C. B. Teeple, and R. J. Wood, “A Dexterous Soft Robotic Hand for Delicate In-Hand Manipulation,” *IEEE Robotics and Automation Letters*, vol. 5, no. 4, pp. 5502–5509, 2020.
- [42] R. Deimel and O. Brock, “A novel type of compliant and underactuated robotic hand for dexterous grasping,” *International Journal of Robotics Research*, vol. 35, no. 1-3, pp. 161–185, 2016.
- [43] J. Zhou, J. Yi, X. Chen, Z. Liu, and Z. Wang, “BCL-13: A 13-DOF soft robotic hand for dexterous grasping and in-hand manipulation,” *IEEE Robotics and Automation Letters*, vol. 3, no. 4, pp. 3379–3386, 2018.
- [44] F. Sørdeide and M. E. Jasinski, “Ormen Lange, Norway - The deepest dig,” *International Journal of Nautical Archaeology*, vol. 37, no. 2, pp. 380–384, 2008.
- [45] S. Licht, E. Collins, M. L. Mendes, and C. Baxter, “Stronger at Depth: Jamming Grippers as Deep Sea Sampling Tools,” *Soft Robotics*, vol. 4, no. 4, pp. 305–316, 2017.

- [46] Y. Hao, S. Biswas, E. Hawkes, T. Wang, M. Zhu, L. Wen, and Y. Visell, “A multimodal, enveloping soft gripper: Shape conformation, bioinspired adhesion, and expansion-driven suction,” *arXiv*, pp. 1–11, 2019.
- [47] J. Shintake, V. Cacucciolo, D. Floreano, and H. Shea, “Soft Robotic Grippers,” *Advanced Materials*, vol. 30, no. 29, 2018.
- [48] B. Mosadegh, P. Polygerinos, C. Keplinger, S. Wennstedt, R. F. Shepherd, U. Gupta, J. Shim, K. Bertoldi, C. J. Walsh, and G. M. Whitesides, “Pneumatic networks for soft robotics that actuate rapidly,” *Advanced Functional Materials*, vol. 24, no. 15, pp. 2163–2170, 2014.
- [49] F. Connolly, P. Polygerinos, C. J. Walsh, and K. Bertoldi, “Mechanical Programming of Soft Actuators by Varying Fiber Angle,” *Soft Robotics*, vol. 2, no. 1, pp. 26–32, 2015.
- [50] N. Bartlett, M. T. Tolley, J. T. B. Overvelde, J. C. Weaver, B. Mosadegh, K. Bertoldi, G. M. Whitesides, and R. J. Wood, “A 3D-printed, functionally graded soft robot powered by combustion,” *Science*, vol. 349, no. 6244, pp. 161–166, 2015.
- [51] H. Lipson, “Challenges and Opportunities for Design, Simulation, and Fabrication of Soft Robots,” *Soft Robotics*, vol. 1, no. 1, pp. 21–27, 2014.
- [52] K. Ghazi-Zahedi, R. Deimel, G. Montufar, V. Wall, and O. Brock, “Morphological computation: The good, the bad, and the ugly,” *IEEE International Conference on Intelligent Robots and Systems*, vol. 2017-Septe, pp. 464–469, 2017.
- [53] A. D. Marchese, R. K. Katzschmann, and D. Rus, “A Recipe for Soft Fluidic Elastomer Robots,” *Soft Robotics*, vol. 2, no. 1, pp. 7–25, 2015.
- [54] K. L. Bell, J. Flanders, A. Bowman, and N. A. Raineault, “New frontiers in ocean exploration: The E/V nautilus, NOAA ship okeanos explorer, and R/V falkor 2016 field season,” *Oceanography*, vol. 30, no. 1, 2017.
- [55] S. Kurumaya, B. T. Phillips, K. P. Becker, M. H. Rosen, D. F. Gruber, K. C. Galloway, K. Suzumori, and R. J. Wood, “A Modular Soft Robotic Wrist for Underwater Manipulation,” *Soft Robotics*, vol. 5, pp. 399–409, 8 2018.

- [56] B. T. Phillips, K. P. Becker, S. Kurumaya, K. C. Galloway, G. Whittredge, D. M. Vogt, C. B. Teeple, M. H. Rosen, V. A. Pieribone, D. F. Gruber, and R. J. Wood, “A Dexterous, Glove-Based Teleoperable Low-Power Soft Robotic Arm for Delicate Deep-Sea Biological Exploration,” *Scientific Reports*, vol. 8, no. 1, p. 14779, 2018.
- [57] C. B. Teeple, K. P. Becker, and R. J. Wood, “Soft Curvature and Contact Force Sensors for Deep-Sea Grasping via Soft Optical Waveguides,” *IEEE International Conference on Intelligent Robots and Systems*, pp. 1621–1627, 2018.
- [58] D. M. Vogt, K. P. Becker, B. T. Phillips, M. A. Graule, R. D. Rotjan, T. M. Shank, E. E. Cordes, R. J. Wood, and D. F. Gruber, “Shipboard design and fabrication of custom 3D-printed soft robotic manipulators for the investigation of delicate deep-sea organisms,” *PLoS ONE*, vol. 13, no. 8, pp. 1–16, 2018.
- [59] S. Nojiri, K. Mizushima, Y. Suzuki, T. Tsuji, and T. Watanabe, “Development of contact area variable surface for manipulation requiring sliding,” *RoboSoft 2019 - 2019 IEEE International Conference on Soft Robotics*, pp. 131–136, 2019.
- [60] H. S. Stuart, S. Wang, and M. R. Cutkosky, “Tunable Contact Conditions and Grasp Hydrodynamics Using Gentle Fingertip Suction,” *IEEE Transactions on Robotics*, vol. 35, no. 2, pp. 295–306, 2019.
- [61] A. J. Spiers, B. Calli, A. M. Dollar, and S. Member, “Variable-Friction Finger Surfaces to Enable Within-Hand Manipulation via Gripping and Sliding,” vol. 3, no. 4, pp. 4116–4123, 2018.
- [62] E. Buselli, V. Pensabene, P. Castrataro, P. Valdastri, A. Menciassi, and P. Dario, “Evaluation of friction enhancement through soft polymer micro-patterns in active capsule endoscopy,” *Measurement Science and Technology*, vol. 21, no. 10, 2010.
- [63] P. Glass, E. Cheung, and M. Sitti, “A legged anchoring mechanism for capsule endoscopes using micropatterned adhesives,” *IEEE Transactions on Biomedical Engineering*, vol. 55, no. 12, pp. 2759–2767, 2008.
- [64] D. Santos, B. Heyneman, S. Kim, N. Esparza, and M. R. Cutkosky, “Gecko-inspired climbing behaviors on vertical and overhanging surfaces,” *Proceedings - IEEE International Conference on Robotics and Automation*, pp. 1125–1131, 2008.

- [65] B. Aksak, M. P. Murphy, and M. Sitti, “Gecko inspired micro-fibrillar adhesives for wall climbing robots on micro/nanoscale rough surfaces,” *Proceedings - IEEE International Conference on Robotics and Automation*, pp. 3058–3063, 2008.
- [66] P. Day, E. V. Eason, N. Esparza, D. Christensen, and M. Cutkosky, “Microwedge Machining for the Manufacture of Directional Dry Adhesives,” *Journal of Micro and Nano-Manufacturing*, vol. 1, no. 1, p. 011001, 2013.
- [67] S. Kim, M. Sitti, T. Xie, and X. Xiao, “Reversible dry micro-fibrillar adhesives with thermally controllable adhesion,” *Soft Matter*, vol. 5, no. 19, p. 3689, 2009.
- [68] P.-C. Lin, S. Vajpayee, A. Jagota, C.-Y. Hui, and S. Yang, “Mechanically tunable dry adhesive from wrinkled elastomers,” *Soft Matter*, vol. 4, p. 1830, 2008.
- [69] D. Liu and D. J. Broer, “Self-assembled Dynamic 3D Fingerprints in Liquid-Crystal Coatings Towards Controllable Friction and Adhesion,” *Angewandte Chemie*, vol. 126, no. 18, pp. 4630–4634, 2014.
- [70] V. Vikas, E. Cohen, R. Grassi, C. Sozer, and B. Trimmer, “Design and locomotion control of soft robot using friction manipulation and motor-tendon actuation,” vol. 02155, no. 4, pp. 1–11, 2015.
- [71] T. Umedachi, V. Vikas, and B. A. Trimmer, “Highly deformable 3-D printed soft robot generating inching and crawling locomotions with variable friction legs,” *IEEE International Conference on Intelligent Robots and Systems*, pp. 4590–4595, 2013.
- [72] C. Majidi, R. F. Shepherd, R. K. Kramer, G. M. Whitesides, and R. J. Wood, “Influence of surface traction on soft robot undulation,” *The International Journal of Robotics Research*, vol. 32, no. 13, pp. 1577–1584, 2013.
- [73] T. Nishimura, Y. Suzuki, T. Tsuji, and T. Watanabe, “Fluid pressure monitoring-based strategy for delicate grasping of fragile objects by a robotic hand with fluid fingertips,” *Sensors (Switzerland)*, vol. 19, no. 4, 2019.
- [74] T. Hou, X. Yang, Y. Aiyama, K. Liu, Z. Wang, T. Wang, J. Liang, and Y. Fan, “Design and experiment of a universal two-fingered hand with soft fingertips based on jamming effect,” *Mechanism and Machine Theory*, vol. 133, pp. 706–719, 2019.

- [75] S. Donaire, J. Borràs, G. Alenyà, and C. Torras, “A Versatile Gripper for Cloth Manipulation,” vol. 5, no. 4, pp. 6520–6527, 2020.
- [76] K. Mizushima, Y. Suzuki, T. Tsuji, and T. Watanabe, “Deformable fingertip with a friction reduction system based on lubricating effect for smooth operation under both dry and wet conditions,” *Advanced Robotics*, vol. 33, no. 10, pp. 508–519, 2019.
- [77] A. P. Russell, *Descriptive and functional anatomy of the digital vascular system of the tokay, Gekko gecko*, vol. 169. 1981.
- [78] L. Tang and N. Y. Lee, “A facile route for irreversible bonding of plastic-PDMS hybrid microdevices at room temperature,” *Lab on a Chip*, vol. 10, no. 10, pp. 1274–1280, 2010.
- [79] V. Sunkara, D. K. Park, and Y. K. Cho, “Versatile method for bonding hard and soft materials,” *RSC Advances*, vol. 2, no. 24, pp. 9066–9070, 2012.
- [80] M. Spenko, M. Cutkosky, C. Majidi, R. Fearing, R. Groff, and K. Autumn, “Foot design and integration for bioinspired climbing robots,” *Unmanned Systems Technology VIII*, vol. 6230, pp. 623019–623019, 2006.
- [81] P. Day, E. V. Eason, N. Esparza, D. Christensen, and M. Cutkosky, “Microwedge Machining for the Manufacture of Directional Dry Adhesives,” *Journal of Micro and Nano-Manufacturing*, vol. 1, no. 1, p. 011001, 2013.
- [82] K. Suzumori, M. Mihara, and S. Wakimoto, “Beautiful flexible microactuator changing its structural color with variable pitch grating,” *Proceedings - IEEE International Conference on Robotics and Automation*, pp. 2771–2776, 2011.
- [83] C. Y. Chen, L. Y. Cheng, C. C. Hsu, and K. Mani, “Microscale flow propulsion through bioinspired and magnetically actuated artificial cilia,” *Biomicrofluidics*, vol. 9, no. 3, 2015.
- [84] A. Keißner and C. Brücker, “Directional fluid transport along artificial ciliary surfaces with base-layer actuation of counter-rotating orbital beating patterns,” *Soft Matter*, vol. 8, no. 19, pp. 5342–5349, 2012.

- [85] B. Gorissen, M. de Volder, and D. Reynaerts, “Pneumatically-actuated artificial cilia array for biomimetic fluid propulsion.,” *Lab on a chip*, vol. 15, no. 22, pp. 4348–4355, 2015.
- [86] E. Milana, B. Gorissen, S. Peerlinck, M. De Volder, and D. Reynaerts, “Artificial Soft Cilia with Asymmetric Beating Patterns for Biomimetic Low-Reynolds-Number Fluid Propulsion,” *Advanced Functional Materials*, vol. 1900462, pp. 1–8, 2019.
- [87] F. Saito and K. Suzumori, “Micro rubber structure realizing multi-legged passive walking - Integration and miniaturization by micro rubber molding process,” *2009 IEEE/RSJ International Conference on Intelligent Robots and Systems, IROS 2009*, pp. 3025–3030, 2009.
- [88] A. R. Shields, B. L. Fiser, B. A. Evans, M. R. Falvo, S. Washburn, and R. Superfine, “Biomimetic cilia arrays generate simultaneous pumping and mixing regimes,” *Proceedings of the National Academy of Sciences*, vol. 107, no. 36, pp. 15670–15675, 2010.
- [89] M. Vilfan, A. Potocnik, B. Kavcic, N. Osterman, I. Poberaj, A. Vilfan, and D. Babic, “Self-assembled artificial cilia,” *Proceedings of the National Academy of Sciences*, vol. 107, no. 5, pp. 1844–1847, 2009.
- [90] H. Lu, M. Zhang, Y. Yang, Q. Huang, T. Fukuda, Z. Wang, and Y. Shen, “A bioinspired multilegged soft millirobot that functions in both dry and wet conditions,” *Nature Communications*, vol. 9, no. 1, 2018.
- [91] Y. Wang, J. Den Toonder, R. Cardinaels, and P. Anderson, “A continuous roll-pulling approach for the fabrication of magnetic artificial cilia with microfluidic pumping capability,” *Lab on a Chip*, vol. 16, no. 12, pp. 2277–2286, 2016.
- [92] K. Ogura, S. Wakimoto, K. Suzumori, and Y. Nishioka, “Micro pneumatic curling actuator - Nematode actuator -,” *2008 IEEE International Conference on Robotics and Biomimetics*, pp. 462–467, 2009.
- [93] S. Wakimoto, K. Ogura, K. Suzumori, and Y. Nishioka, “Miniature soft hand with curling rubber pneumatic actuators,” *Proceedings - IEEE International Conference on Robotics and Automation*, pp. 556–561, 2009.

- [94] Y. Lu and C.-j. C. Y. Kim, “Micro-finger articulation by pneumatic parylene balloons,” *Engineering*, pp. 276–279, 2003.
- [95] S. Konishi, F. Kawai, and P. Cusin, “Thin flexible end-effector using pneumatic balloon actuator,” *Sensors and Actuators, A: Physical*, vol. 89, no. 1-2, pp. 28–35, 2001.
- [96] O. C. Jeong and S. Konishi, “All PDMS pneumatic microfinger with bidirectional motion and its application,” *Journal of Microelectromechanical Systems*, vol. 15, no. 4, pp. 896–903, 2006.
- [97] Y. Watanabe, M. Maeda, N. Yaji, R. Nakamura, and H. Iseki, “Small, soft, and safe microactuator for retinal pigment epithelium transplantation,” no. January, pp. 659–662, 2007.
- [98] S. Konishi, M. Nokata, O. C. Jeong, S. Kusuda, T. Sakakibara, M. Kuwayama, and H. Tsutsumi, “Pneumatic micro hand and miniaturized parallel link robot for micro manipulation robot system,” *Proceedings - IEEE International Conference on Robotics and Automation*, vol. 2006, no. May, pp. 1036–1041, 2006.
- [99] N. R. Sinatra, T. Ranzani, J. J. Vlassak, K. K. Parker, and R. J. Wood, “Nanofiber-reinforced soft fluidic micro-actuators,” *Journal of Micromechanics and Microengineering*, vol. 28, no. 8, p. aab373, 2018.
- [100] K. Suzumori, “Elastic materials producing compliant robots,” *Robotics and Autonomous Systems*, vol. 18, pp. 135–140, 1996.
- [101] R. V. Martinez, C. R. Fish, X. Chen, and G. M. Whitesides, “Elastomeric origami: Programmable paper-elastomer composites as pneumatic actuators,” *Advanced Functional Materials*, vol. 22, no. 7, pp. 1376–1384, 2012.
- [102] J. Paek, I. Cho, and J. Kim, “Microrobotic tentacles with spiral bending capability based on shape-engineered elastomeric microtubes,” *Scientific Reports*, vol. 5, no. March, p. 10768, 2015.
- [103] D. Rus and M. T. Tolley, “Design, fabrication and control of soft robots,” *Nature*, vol. 521, no. 7553, pp. 467–475, 2015.

- [104] R. V. Martinez, J. L. Branch, C. R. Fish, L. Jin, R. F. Shepherd, R. M. D. Nunes, Z. Suo, and G. M. Whitesides, “Robotic tentacles with three-dimensional mobility based on flexible elastomers,” *Advanced Materials*, vol. 25, no. 2, pp. 205–212, 2013.
- [105] M. Cianchetti, M. Calisti, L. Margheri, M. Kuba, and C. Laschi, “Bioinspired locomotion and grasping in water: the soft eight-arm OCTOPUS robot,” *Bioinspiration & Biomimetics*, vol. 10, no. 3, p. 035003, 2015.
- [106] I. Must, E. Sinibaldi, and B. Mazzolai, “on reversible osmotic actuation,” *Nature Communications*, no. 2019, pp. 1–8, 2019.
- [107] S. Kurumaya, H. Nabae, G. Endo, and K. Suzumori, “Design of thin McKibben muscle and multifilament structure,” *Sensors and Actuators, A: Physical*, vol. 261, pp. 66–74, 2017.
- [108] J. Zhou, S. Chen, and Z. Wang, “A Soft-Robotic Gripper with Enhanced Object Adaptation and Grasping Reliability,” *IEEE Robotics and Automation Letters*, vol. 2, no. 4, pp. 2287–2293, 2017.
- [109] C. Lefteri, *Making It: Manufacturing Techniques for Product Design*. Laurence King Publishing, 2nd ed., 2012.
- [110] B. Gorissen, W. Vincentie, F. Al-Bender, D. Reynaerts, and M. De Volder, “Modeling and bonding-free fabrication of flexible fluidic microactuators with a bending motion,” *Journal of Micromechanics and Microengineering*, vol. 23, no. 4, 2013.
- [111] K. C. Galloway, P. Polygerinos, C. J. Walsh, and R. J. Wood, “Mechanically programmable bend radius for fiber-reinforced soft actuators,” *2013 16th International Conference on Advanced Robotics, ICAR 2013*, 2013.
- [112] A. Yamaguchi, K. Takemura, S. Yokota, and K. Edamura, “A robot hand using electro-conjugate fluid,” *Proceedings - IEEE International Conference on Robotics and Automation*, pp. 5923–5928, 2011.
- [113] K. Suzumori, S. Iikura, and H. Tanaka, “Development of flexible microactuator and its applications to robotic mechanisms,” in *Proceedings. 1991 IEEE International Conference on Robotics and Automation*, pp. 1622–1627, IEEE Comput. Soc. Press.

- [114] N. W. Bartlett, K. P. Becker, and R. J. Wood, “A fluidic demultiplexer for controlling large arrays of soft actuators,” *Soft Matter*, vol. 16, no. 25, pp. 5871–5877, 2020.
- [115] K. Murasugi, *Knot Theory & Its Applications*. 2008.
- [116] M. T. Mason, “Toward Robotic Manipulation,” *Annual Review of Control, Robotics, and Autonomous Systems*, vol. 1, no. 1, pp. 1–28, 2018.
- [117] A. Bicchi, “Hands for dexterous manipulation and robust grasping: A difficult road toward simplicity,” *IEEE Transactions on Robotics and Automation*, vol. 16, no. 6, pp. 652–662, 2000.
- [118] M. R. Cutkosky and P. K. Wright, “Friction, Stability and the Design of Robotic Fingers,” *The International Journal of Robotics Research*, vol. 5, no. 4, pp. 20–37, 1986.
- [119] A. Bicchi, “On the Closure Properties of Robotic Grasping,” *The International Journal of Robotics Research*, vol. 14, no. 4, pp. 319–334, 1995.
- [120] S. C. Jacobsen, E. K. Iversen, D. F. Knutti, R. T. Johnson, and K. B. Biggers, “THE UTAHh4.I.T. DEXTROUS HAND S.C. Jacobsen, E.K. Iversen, D.F. Knutti, R.T. Johnson, K.B. Biggers Center for Engineering Design, University of Utah,” *Science*, 1986.
- [121] W. Townsend, “The BarrettHand grasper – programmably flexible part handling and assembly,” *Industrial Robot: An International Journal*, vol. 27, no. 3, pp. 181–188, 2000.
- [122] A. Kochan, “Shadow delivers first hand,” *Industrial Robot: An International Journal*, vol. 32, pp. 15–16, 2 2005.
- [123] L. B. Bridgwater, C. A. Ihrke, M. A. Diftler, M. E. Abdallah, N. A. Radford, J. M. Rogers, S. Yayathi, R. S. Askew, and D. M. Linn, “The robonaut 2 hand - Designed to do work with tools,” *Proceedings - IEEE International Conference on Robotics and Automation*, pp. 3425–3430, 2012.
- [124] Robotiq, “2F-85 and 2F-140 Grippers,” *Online datasheet*, 2019.

- [125] J. Mahler, J. Liang, S. Niyaz, M. Laskey, R. Doan, X. Liu, J. A. Ojea, and K. Goldberg, “Dex-net 2.0: Deep learning to plan robust grasps with synthetic point clouds and analytic grasp metrics,” *arXiv*, 2017.
- [126] L. U. Odhner, L. P. Jentoft, M. R. Claffee, N. Corson, Y. Tenzer, R. R. Ma, M. Buehler, R. Kohout, R. D. Howe, and a. M. Dollar, “A compliant, underactuated hand for robust manipulation,” *The International Journal of Robotics Research*, vol. 33, no. 5, pp. 736–752, 2014.
- [127] a. M. Dollar and R. D. Howe, “The Highly Adaptive SDM Hand: Design and Performance Evaluation,” *The International Journal of Robotics Research*, vol. 29, no. 5, pp. 585–597, 2010.
- [128] D. M. Aukes, B. Heyneman, J. Ulmen, H. Stuart, M. R. Cutkosky, S. Kim, P. Garcia, and A. Edsinger, “Design and testing of a selectively compliant underactuated hand,” *International Journal of Robotics Research*, vol. 33, no. 5, pp. 721–735, 2014.
- [129] W. Friedl, H. Hoppner, F. Schmidt, M. A. Roa, and M. Grebenstein, “CLASH: Compliant Low Cost Antagonistic Servo Hands,” *IEEE International Conference on Intelligent Robots and Systems*, pp. 6469–6476, 2018.
- [130] M. G. Catalano, G. Grioli, E. Farnioli, A. Serio, C. Piazza, and A. Bicchi, “Adaptive synergies for the design and control of the Pisa/IIT SoftHand,” *International Journal of Robotics Research*, vol. 33, no. 5, pp. 768–782, 2014.
- [131] J. Zhou, X. Chen, U. Chang, J. T. Lu, C. C. Y. Leung, Y. Chen, Y. Hu, and Z. Wang, “A Soft-Robotic Approach to Anthropomorphic Robotic Hand Dexterity,” *IEEE Access*, vol. 7, pp. 101483–101495, 2019.
- [132] N. R. Sinatra, C. B. Teeple, D. M. Vogt, K. K. Parker, D. F. Gruber, and R. J. Wood, “Ultrgentle manipulation of delicate structures using a soft robotic gripper,” *Science Robotics*, vol. 4, no. 33, pp. 1–12, 2019.
- [133] D. Rus and M. T. Tolley, “Design, fabrication and control of soft robots,” *Nature*, vol. 521, no. 7553, pp. 467–475, 2015.

- [134] K. Becker, Y. Chen, and R. Wood, “Mechanically Programmable Dip Molding of High Aspect Ratio Soft Actuator Arrays,” *Advanced Functional Materials*, vol. 30, no. 12, 2020.
- [135] S. J. Gerbode, J. R. Puzey, A. G. McCormick, and L. Mahadevan, “How the Cucumber Tendril Coils and Overwinds,” *Science*, vol. 337, pp. 1087–1091, 8 2012.
- [136] L. P. Madin, “Feeding behavior of tentaculate predators: in situ observations and a conceptual model,” *Bulletin of Marine Science*, vol. 43, no. 3, pp. 413–429, 1988.
- [137] D. J. Montana, “Contact Stability for Two-Fingered Grasps,” *IEEE Transactions on Robotics and Automation*, vol. 8, no. 4, pp. 421–430, 1992.
- [138] B. Calli, A. Walsman, A. Singh, S. Srinivasa, P. Abbeel, and A. M. Dollar, “Benchmarking in Manipulation Research: Using the Yale-CMU-Berkeley Object and Model Set,” *IEEE Robotics and Automation Magazine*, vol. 22, no. 3, pp. 36–52, 2015.
- [139] D. M. Aukes and M. R. Cutkosky, “Simulation-based tools for evaluating underactuated hand designs,” *Proceedings - IEEE International Conference on Robotics and Automation*, pp. 2067–2073, 2013.
- [140] E. Cosserat and F. Cosserat, *Theorie des corps d’formables*. A. Hermann et fils, 1909.
- [141] M. Gazzola, L. H. Dudte, A. G. McCormick, and L. Mahadevan, “Forward and inverse problems in the mechanics of soft filaments,” *Royal Society Open Science*, vol. 5, no. 6, 2018.
- [142] K. P. Becker, C. B. Teeple, N. Charles, L. Mahadevan, and R. J. Wood, “Grasping Via Entanglement,” *Under Review*, 2021.
- [143] C. B. Teeple, “Ctrl-P: Smooth Pressure Control for Soft Robots.”
- [144] M. Cianchetti, T. Ranzani, G. Gerboni, I. D. Falco, C. Laschi, S. Member, and A. Menciassi, “STIFF-FLOP Surgical Manipulator mechanical design and,” *2013 IEEE/RSJ International Conference on Intelligent Robots and Systems (IROS)*, pp. 3576–3581, 2013.

- [145] Y. S. Narang, J. J. Vlassak, and R. D. Howe, “Mechanically Versatile Soft Machines through Laminar Jamming,” *Advanced Functional Materials*, vol. 28, no. 17, pp. 1–9, 2018.
- [146] R. Baines, S. Freeman, F. Fish, and R. Kramer-Bottiglio, “Variable stiffness morphing limb for amphibious legged robots inspired by chelonian environmental adaptations,” *Bioinspiration and Biomimetics*, vol. 15, no. 2, 2020.
- [147] P. Glass, E. Cheung, and M. Sitti, “A legged anchoring mechanism for capsule endoscopes using micropatterned adhesives,” *IEEE Transactions on Biomedical Engineering*, vol. 55, no. 12, pp. 2759–2767, 2008.
- [148] H. Lee, B. P. Lee, and P. B. Messersmith, “A reversible wet/dry adhesive inspired by mussels and geckos,” *Nature*, vol. 448, no. 7151, pp. 338–341, 2007.
- [149] G. Greco, F. Bosia, F. Tramacere, B. Mazzolai, and N. M. Pugno, “The role of hairs in the adhesion of octopus suckers: A hierarchical peeling approach,” *Bioinspiration and Biomimetics*, vol. 15, no. 3, 2020.
- [150] A. P. Russell, *Descriptive and functional anatomy of the digital vascular system of the tokay, Gekko gecko*, vol. 169. 1981.
- [151] B. Trimmer, R. H. Ewoldt, M. Kovac, H. Lipson, N. Lu, M. Shahinpoor, and C. Majidi, “At the Crossroads: Interdisciplinary Paths to Soft Robots,” *Soft Robotics*, vol. 1, no. 1, pp. 63–69, 2014.
- [152] N. Gravish and G. V. Lauder, “Robotics-inspired biology,” *Journal of Experimental Biology*, vol. 221, no. 7, pp. 1–8, 2018.
- [153] H. Guo, J. Nawroth, Y. Ding, and E. Kanso, “Cilia beating patterns are not hydrodynamically optimal,” *Physics of Fluids*, vol. 26, no. 9, p. 091901, 2014.
- [154] Y. Ding, J. C. Nawroth, M. J. McFall-Ngai, and E. Kanso, “Mixing and transport by ciliary carpets: A numerical study,” *Journal of Fluid Mechanics*, vol. 743, pp. 124–140, 2014.
- [155] B. Gorissen, T. Chishiro, S. Shimomura, D. Reynaerts, M. De Volder, and S. Konishi, “Flexible pneumatic twisting actuators and their application to tilting micromirrors,” *Sensors and Actuators A: Physical*, vol. 216, pp. 426–431, 2014.

- [156] S. Heydari, A. Johnson, O. Ellers, M. J. McHenry, and E. Kansa, “Sea star inspired crawling and bouncing,” *arXiv*, 2019.
- [157] D. Howard, A. E. Eiben, D. F. Kennedy, J. B. Mouret, P. Valencia, and D. Winkler, “Evolving embodied intelligence from materials to machines,” *Nature Machine Intelligence*, vol. 1, no. 1, pp. 12–19, 2019.